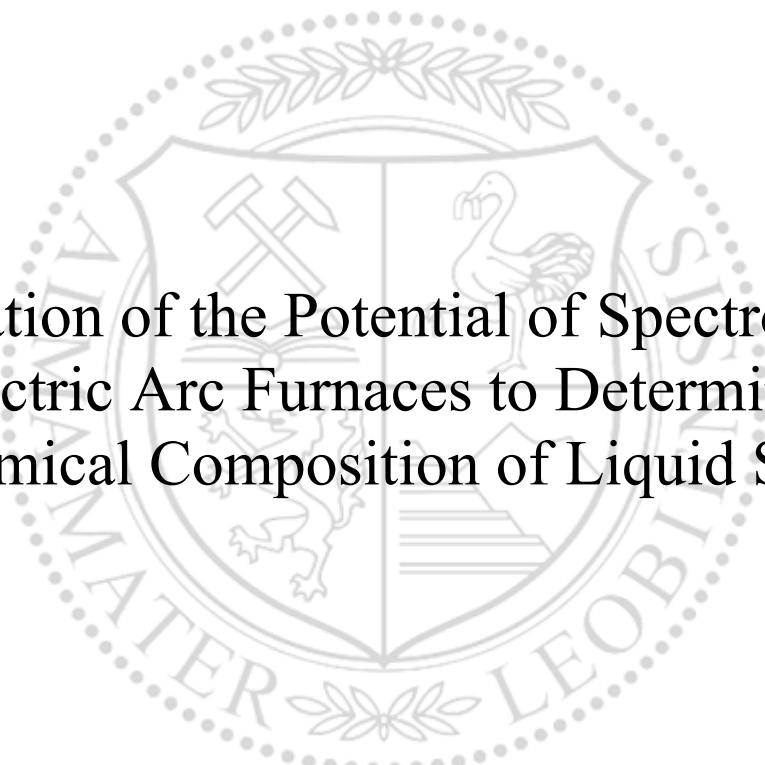




Chair of Automation

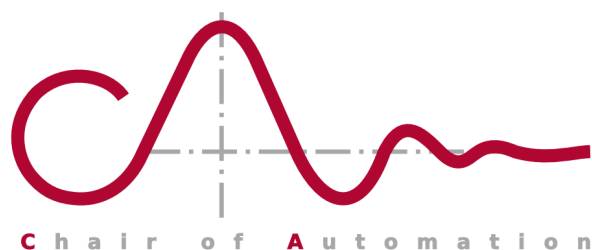
Master's Thesis



Evaluation of the Potential of Spectroscopy  
in Electric Arc Furnaces to Determine the  
Chemical Composition of Liquid Steel

Florian Floh, BSc

September 2019



Copyright ©2019

Florian Floh

Chair of Automation  
Department Product Engineering  
Montanuniversitaet Leoben  
Peter-Tunner Straße 25  
8700 LEOBEN, Austria

W: automation.unileoben.ac.at

E: automation@unileoben.ac.at

T: +43(0)3842/402-5301

F: +43(0)3842/402-5302

When using  $\text{BIB}\text{T}_{\text{E}}\text{X}$ , copy and paste the following lines, to cite this work:

```
@mastersthesis{FFlohMasterT2019,  
  author      = {Florian Floh},  
  title       = {Evaluation of the Potential of Spectroscopy in  
                Electric Arc Furnaces to Determine the Chemical  
                Composition of Liquid Steel},  
  school      = {Montanuniversitaet Leoben},  
  year        = 2019,  
}
```

Last compiled on Wednesday 2<sup>nd</sup> October, 2019.

This thesis was typeset using  $\text{L}^{\text{A}}\text{T}_{\text{E}}\text{X}$ .

$\text{T}_{\text{E}}\text{X}$  is a trademark of the American Mathematical Society.



## EIDESSTATTLICHE ERKLÄRUNG

Ich erkläre an Eides statt, dass ich diese Arbeit selbständig verfasst, andere als die angegebenen Quellen und Hilfsmittel nicht benutzt, und mich auch sonst keiner unerlaubten Hilfsmittel bedient habe.

Ich erkläre, dass ich die Richtlinien des Senats der Montanuniversität Leoben zu "Gute wissenschaftliche Praxis" gelesen, verstanden und befolgt habe.

Weiters erkläre ich, dass die elektronische und gedruckte Version der eingereichten wissenschaftlichen Abschlussarbeit formal und inhaltlich identisch sind.

Datum 18.09.2019

---

Unterschrift Verfasser/in  
Florian, Floh  
Matrikelnummer: 01335151

# Abstract

This thesis investigates the feasibility and stability of using atomic emission spectroscopy as a means of determining the composition of liquid steel in an electric arc furnace (EAF). In the first step of the data processing, the observed spectra from the spectroscope are smoothed (Savitzky-Golay polynomial smoothing) and the baseline is removed, with methods based on “minimizing non-quadratic cost functions” or “penalized least-squares”. Next, the corresponding chemical elements are assigned to the peaks in the spectra with the help of the online database “NIST Atomic Spectra Database”. In the final step, calibration curves are established for each element, in order to determine, whether there is correlation between the observations and the actual content of the corresponding element in the steel sample.

The experimental setup, conceived and implemented in the course of this work, covers a small-scale laboratory EAF and a spectroscope. In order to conduct the required experiments, low alloy steel samples of known chemical composition are utilized and the arc that is established between the molten steel and the graphite electrode is observed by the spectroscope.

The results of this thesis lead to the assumption, that the setup, that was available for the experimental work may not be sufficiently suitable to be conclusive with respect to an industrial oven and equipment.

Another major finding of this work is, that the uncontrolled nature of the arc in an EAF is not suitable as an excitation source for atomic spectroscopy, due to the instability and the sensitivity to impurities in the sample.

## Index Terms

Atomic Emission Spectroscopy; Spectroscopy; Electric Arc Furnace; EAF; Steel Analysis; In-Situ Analysis; Steelmaking

# Kurzfassung

Diese Arbeit untersucht die Machbarkeit und das Potential der Methode, die chemische Zusammensetzung der Stahlschmelze in einem Lichtbogenofen (EAF) mittels Atomemissionsspektroskopie zu bestimmen.

Im ersten Schritt der Datenverarbeitung werden die vom Spektroskop erhaltenen Spektren geglättet (Savitzky-Golay polynomial smoothing) und die Basislinie mittels Methoden, die auf der "Minimierung nicht-quadratischer Cost-Functions" und "Penalized Least-Squares" basieren, entfernt. Im nächsten Schritt werden die entsprechenden chemischen Elemente den Peaks in den Spektren, unter Zuhilfenahme der Online-Datenbank "NIST Atomic Spectra Database", zugewiesen. Das Erstellen sogenannter "Kalibrierkurven" ermöglicht es sodann, zu ermitteln, ob eine Korrelation zwischen den beobachteten Daten und den tatsächlichen chemischen Zusammensetzungen der Stahlproben zu verzeichnen ist.

Die Versuchsanordnung, welche während dieser Arbeit ersonnen und implementiert wird, umfasst einen EAF im Labormaßstab und ein Spektroskop. Für die experimentelle Durchführung werden Proben aus niedriglegiertem Stahl bekannter chemischer Zusammensetzung verwendet und der Lichtbogen, welcher sich zwischen Elektrode und ebendieser Stahlproben ausbildet, vom Spektroskop erfasst. Die Ergebnisse dieser Arbeit führen zu der Annahme, dass die zur Verfügung stehende Versuchsanordnung keine eindeutigen Rückschlüsse auf eine mögliche Anwendung in einem Industrie-EAF zulässt.

Des Weiteren eignet sich der Lichtbogen in einem EAF, aufgrund seiner instabilen Ausbildung, nur bedingt für Atomemissionsspektroskopie.

## Schlagwörter

Atomemissionsspektroskopie; Spektroskopie; Lichtbogenofen; EAF; Stahlanalyse; In-Situ Analyse; Stahlerzeugung

# Acknowledgements

I would like to dedicate this page to express my special thanks of gratitude to those, who made this work possible and to those who supported me in all my technical challenges.

First off, I want to thank INTECO atec automation GmbH, especially Dipl.-Ing. Dr. mont. Ronald Ofner, MBA, who gave me the opportunity to work on this thesis. Next, I am thankful to my colleagues at the Chair of Automation who provided me with great support in all my difficulties and technical questions.

Finally, I would also like to thank the PhD.-students from the institute of Ferrous Metallurgy, who helped me with conducting the required measurements for this thesis.

# Contents

<b>Abstract</b>	<b>iii</b>
<b>Kurzfassung</b>	<b>iv</b>
<b>Acknowledgements</b>	<b>v</b>
<b>1 Introduction</b>	<b>1</b>
1.1 Outlook of this Thesis . . . . .	2
1.2 Motivation . . . . .	3
<b>2 Electric Arc Furnace</b>	<b>6</b>
2.1 The Role of the Electric Arc Furnace in the Steel- making Industry . . . . .	6
2.1.1 The Process Stages During the Operation of an EAF . . . . .	7
2.2 Brief Historical Overview of Electric Arc Furnace Steelmaking . . . . .	11
2.3 Construction of an Electric Arc Furnace . . . . .	11
2.3.1 Containment of an EAF . . . . .	12
2.3.2 Electric Circuit of an EAF . . . . .	14
2.4 Fundamentals of a Plasma . . . . .	19
2.4.1 Classifications of Plasmas . . . . .	20
2.4.2 Important Physical Properties of Plasmas . . . . .	20
2.4.3 Some Examples of Plasmas . . . . .	22
2.4.4 The Process of Ionization . . . . .	23
2.4.5 Arcs in Industrial Furnaces . . . . .	23
2.4.6 Atmosphere in a Steelmaking Electric Arc Furnace . . . . .	24
<b>3 Atomic Spectroscopy</b>	<b>25</b>
3.1 The Effect of Temperature on Spectroscopy . . . . .	27
3.2 The Process of Atomization in Spectroscopy . . . . .	28
3.2.1 Atomization with the Help of an Inductively Coupled Plasma . . . . .	29
3.2.2 Atomization with the Help of a Flame . . . . .	30
3.2.3 Atomization with the Help of Furnaces . . . . .	32

<b>4</b>	<b>Experimental Setup</b>	<b>34</b>
4.1	Small Scale EAF as the Experimental Setup . . . . .	34
4.1.1	Bottom Part of the Furnace . . . . .	34
4.1.2	Roof Part of the Furnace . . . . .	36
4.1.3	The Electrode and the Electrode Lifting Mechanism . . . . .	36
4.1.4	Spectrometer and Optical Fibre . . . . .	36
4.1.5	Adjusting Mechanism for the Optical Fibre . . . . .	37
<b>5</b>	<b>Data Processing</b>	<b>40</b>
5.1	Savitzky-Golay Polynomial Smoothing . . . . .	40
5.1.1	Some Properties of SG-Smoothing Filters . . . . .	49
5.2	Background Correction and Baseline Estimation . . . . .	51
5.2.1	Background Removal by Minimizing a Non-Quadratic Cost Function . . . . .	51
5.2.2	Adaptive Iteratively Reweighted Penalized Least-Squares Background Correction . . . . .	57
5.3	Generating Synthetic Spectrometer Data . . . . .	62
5.4	Peak Detection . . . . .	63
<b>6</b>	<b>Results and Conclusion</b>	<b>69</b>
6.1	Results . . . . .	69
6.2	Conclusion . . . . .	80
<b>A</b>	<b>Code</b>	<b>81</b>
A.1	Savitzky-Golay Polynomial Smoothing . . . . .	81
A.2	Background Removal by Minimizing a Non-Quadratic Cost Function . . . . .	83
A.3	Adaptive Iteratively Reweighted Penalized Least-Squares Background Correction . . . . .	86
A.4	Synthetic Spectrometer Data . . . . .	88
A.5	Peak Detection . . . . .	91



# List of Figures

1.1	Worldwide Crude Steel Production in Million Tonnes in 2017 . . . . .	1
1.2	Overview of Innovations and Overall Improvements in EAF Steelmaking [1] . . . . .	3
1.3	Energy Sources and Sinks in an EAF [2] . . . . .	5
1.4	Main Sources of Carbon Dioxide in an EAF, adapted from [2] . . . . .	5
2.1	Overview of the Processes and their Links to Each Other in the Steelmak- ing Industry, adapted from [3] . . . . .	7
2.2	The Different Phases of the Meltdown Process, adapted from [4] . . . . .	9
2.3	Parts of an Electric Arc Furnace, adapted from [3] . . . . .	12
2.4	Schematic Overview of a Steelworks' Power Grid [5] . . . . .	14
2.5	High Current System of an EAF, adapted from [4] . . . . .	15
2.6	Overview of the Different Electrode Supporting Arm Designs [6] . . . . .	16
2.7	Side and Top View of Electrode Supporting Arms [6] . . . . .	17
2.8	Cross Section of an Electrode Clamp [7] . . . . .	17
2.9	Front View of Electrode Holder [6] . . . . .	17
2.10	Diameter of the Electrode Depending on the Current [7] . . . . .	18
2.11	Overview of the Manufacturing Steps of a Graphite Electrode [6] . . . . .	19
2.12	Electrical Conductivity of $Ar$ , $He$ , $H_2$ and $N_2$ , adapted from [8] . . . . .	21
2.13	Enthalpy of $H_2$ , $Ar$ , $N_2$ , $O_2$ , $Ne$ , $He$ as a Function of the Temperature, adapted from [8] . . . . .	22
3.1	Principle of a Crude Prism Spectroscope [9] . . . . .	25
3.2	Schematic Illustration of the Three Forms of Atomic Spectroscopy [10] . . . . .	26
3.3	Cross Section of an Inductively Coupled Plasma Burner [10] . . . . .	29
3.4	Working Principle of a Cyclonic Nebulizer [10] . . . . .	30
3.5	Cross Section of an Ultrasonic Nebulizer, adapted from [10] . . . . .	30
3.6	Parts of a Premix Burner, adapted from [10] . . . . .	31
3.7	Cross Section of the Flame, adapted from [10] . . . . .	31
3.8	Graphite Tubes for Furnaces [10] . . . . .	32

3.9	Sectional View of a Transversely Heated Graphite Furnace, adapted from [10] . . . . .	33
4.1	Cross Section of the Laboratory-EAF . . . . .	35
4.2	Isometric View of the Fibre Holder. <i>Screw 1</i> adjusts the horizontal position and <i>screw 2</i> the angle . . . . .	38
4.3	Fibre Holder Mounted on a Flange on Top of the Furnace Roof . . . . .	38
4.4	Overview of the Fibre Holder's Parts. The white ones are printed from PLA	39
5.1	Data Points and the Corresponding Fitting Polynomials . . . . .	42
5.2	Difference Between Smoothing Polynomial ( $l_s = 41$ , $d = 2$ ) With and Without Endpoint-Correction . . . . .	48
5.3	Comparison of Symmetric and Asymmetric Non-Quadratic Cost-Functions to the Quadratic Cost-Function. ( $s = 3$ ) . . . . .	53
5.4	Baseline Removal, Demonstrated on Synthetic Spectrometer Data. Baseline modelled as a polynomial of order $d = 4$ . . . . .	55
5.5	Baseline Removal, Demonstrated on Real Spectrometer Data . . . . .	55
5.6	Baseline Removal, Demonstrated on Synthetic Spectrometer Data. Baseline modelled as a polynomial of order $d = 3$ . . . . .	60
5.7	Baseline Removal, Demonstrated on Real Spectrometer Data . . . . .	60
5.8	Synthetic Spectrometer Data, Baseline: Polynomial of Order $d = 3$ and Noise $\mu = 0$ , $\sigma = 300$ . . . . .	63
5.9	Signum Function . . . . .	65
5.10	Convolution table in the case of $l = 3$ and $f = 4$ , [11] . . . . .	66
5.11	Detecting the Peaks in a Set of Data from a Spectrometer. <i>Window size</i> = 10, <i>Threshold</i> = 500, hence peaks with <i>Counts</i> lower than 500 are ignored . . . . .	67
6.1	Example of a Calibration Curve. Each horizontal plot of red circles represents one steel sample with a specific content of a certain chemical element	71
6.2	Overview of the Typical Parts of a Boxplot, adapted from [12] . . . . .	72
6.3	Example of a Calibration Curve. Data represented with the help of boxplots	72
6.4	Flowchart, Illustrating Each Step from Raw Spectrometer Data to the Calibration Curves . . . . .	73
6.5	Schematic Overview of the Overall Process from Raw Spectrometer Data to a Calibration Curve . . . . .	74
6.6	Calibration Curve (Chromium) . . . . .	75
6.7	Calibration Curve (Chromium) . . . . .	75
6.8	Calibration Curve (Nickel) . . . . .	76
6.9	Calibration Curve (Copper) . . . . .	76

6.10 Calibration Curve (Manganese) . . . . .	77
6.11 Calibration Curve (Carbon) . . . . .	77
6.12 Calibration Curve (Silicon) . . . . .	78
6.13 Calibration Curve (Aluminum) . . . . .	78
6.14 Calibration Curve (Phosphorous) . . . . .	79
6.15 Calibration Curve (Sulfur) . . . . .	79

# List of Tables

2.1	Constituents of the Slag in an EAF [6] . . . . .	10
2.2	Ionisation Energy of Some Elements [8] . . . . .	23
4.1	Constituents of the Crucible, [13] . . . . .	36
4.2	Technical Data of the Used Spectrometer, taken from [14] . . . . .	37
6.1	The Samples and Their Chemical Composition. The contents are given in wt-%. . . . .	69

# Chapter 1

## Introduction

Over the past ten years, the annual worldwide crude steel production has increased by 25 percent, reaching 1690,5 million tons in 2017. Figure 1.1 depicts the data [15] separated by region. Due to this significant rise and the increasingly stringent environmental requirements, the overall percentage of steel produced from scrap has also seen some significant growth [16].

In steelplants, so-called electric arc furnaces (EAFs) are utilized to convert this recycled scrap back to crude steel. Since electrical energy is used as the main energy source, and the average consumption in modern versions is  $375kWh$  for each ton of steel, it is endeavored to increase the performance with respect to economical and environmental reasons [1], [16].

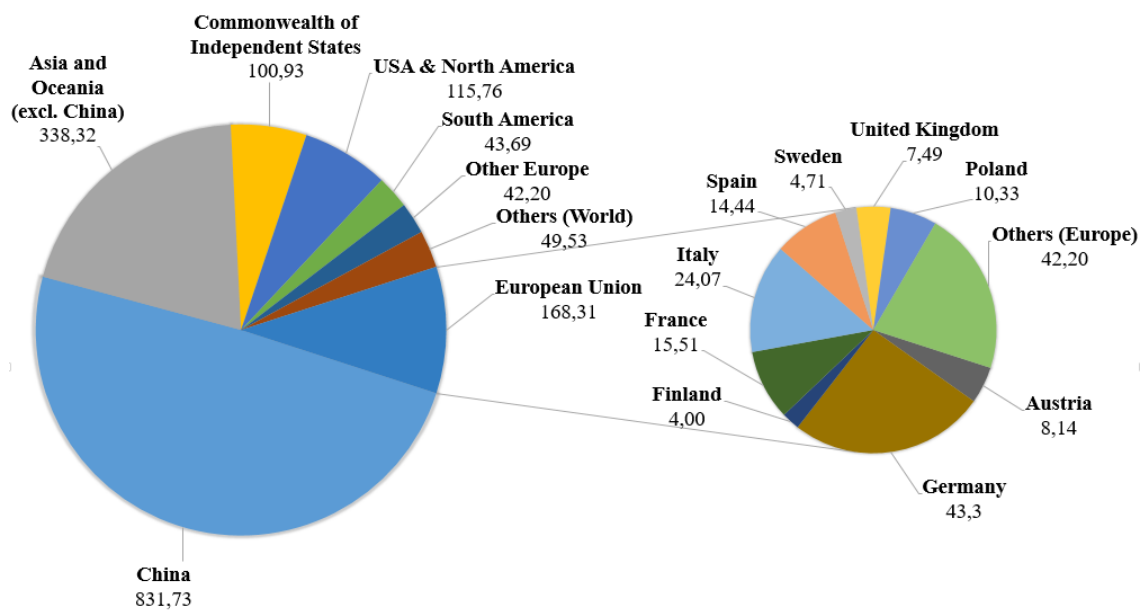


**Figure 1.1:** Worldwide Crude Steel Production in Million Tonnes in 2017

One possible approach of increasing the effectiveness might be to avoid a free burning

arc. In other words, such arcs are not enveloped in slag or scrap, which leads to unwanted energy losses due to radiation. However, detecting such a lack of slag covering is not trivial and is usually estimated with the help of the water temperature in the cooling panels of the furnace. One major disadvantage of this method is, that there is a certain delay (of up to several minutes), since the water in the cooling panels does not change its temperature immediately [17].

To bypass this issue though, the temperature of the arc might be acquired with the aid of spectroscopy. It is known, that these temperatures are in a range of approximately 8000 to 11000K [5]. Whenever values are measured, that are slightly underneath this range, it can be assumed, that the arc is covered with slag and the energy losses are therefore minimized.

What is more, not only the temperature in the region of the arc can be measured with this mentioned approach, but also that of the steel bath. This could replace the usual method, where a sleeve with an attached thermocouple gets either immersed normally or with a lance manipulator through a slag door of the furnace. By opening the slag door, cold air from the surrounding atmosphere gets inside the furnace, which leads to an increase of nitrogen in the vessel of the furnace and also an energy loss, which is both unwanted.

Finally, another aspect of improving the overall efficiency of an EAF with the help of spectroscopy is to conduct an in-situ analysis of the chemical composition of the steel. This implicates to the same advantages as the previously described method to measure the temperature, since an opening of the slag door to obtain a sample of molten steel, which is then analysed via XRF, is not required [17].

## 1.1 Outlook of this Thesis

Even though spectroscopy is capable of the previously mentioned measurements, this thesis solely puts its focus on developing and evaluating a method to analyse the chemical composition during the meltdown process in an industrial electric arc furnace.

In the first part of this thesis, a profound literature research on EAFs is provided, since it is inevitable to investigate the surroundings and the possible influences on the measurement equipment.

The second part addresses the subject of *spectroscopy* with respect to the basic physical principles and how the measurements are conducted under laboratory conditions.

The section, that covers the experimental setup, describes a laboratory version of an electric arc furnace and the overall experimental setup, that was conceptualized and implemented during this thesis.

What is more, the chapter *Data Processing* demonstrates a procedure on how to handle the acquired data, for example, how to reduce the noise in the signal, remove the baseline in each spectrum and detect the local maxima (i.e. peaks).

Subsequently, all the findings and problems, with respect to the construction and data processing are being presented, and discussed.

## 1.2 Motivation

Throughout the past decades, the main focus on research conducted in the area of steel-making in an EAF has been on the improvement of their overall efficiency. This includes, among others, the consumption of electrical energy, the tap-to-tap time and the wear of the graphite electrodes.

Considering an example of a furnace of the approximate size of 120t, the energy consumption was decreased from about 650kWh/t to roughly 350kWh/t within only 40 years, which might be explained due to the reduction of the tap-to-tap times to 30-40mins. Figure 1.2 illustrates these mentioned trends together with significant inventions [1].

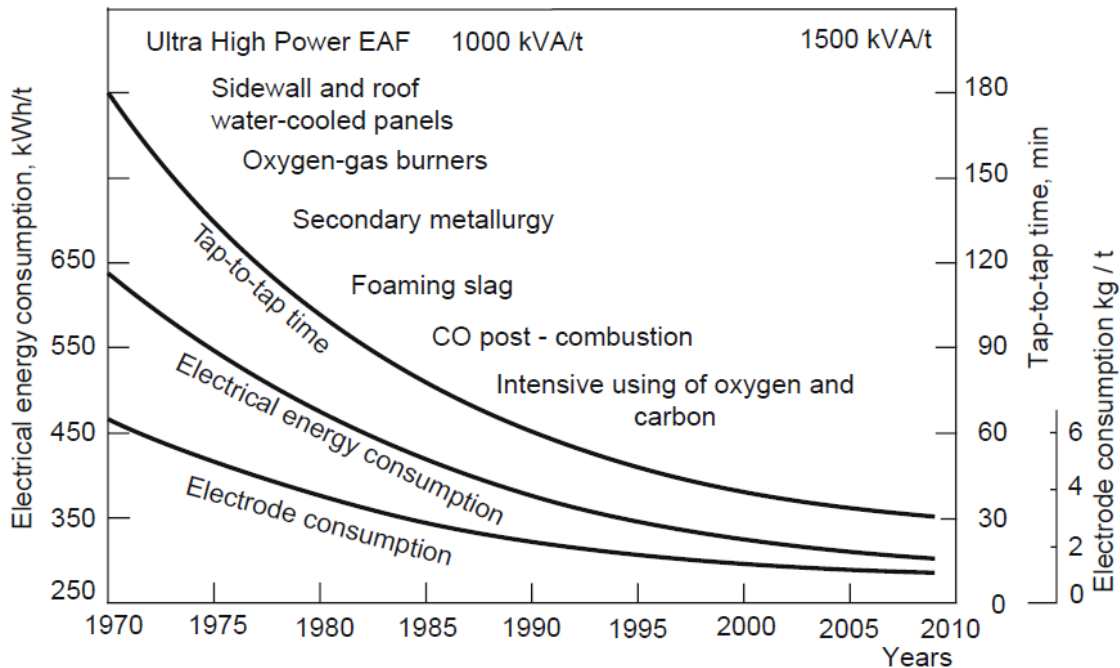


**Figure 1.2:** Overview of Innovations and Overall Improvements in EAF Steelmaking [1]

With the aim of continuing this trend of increasing the EAF's overall efficiency, the objective of this thesis is to evaluate, whether it is possible to determine the composition of molten steel in-situ. As mentioned previously, this would replace the method of obtaining a sample with the help of a sleeve through the slag door, which causes an unwanted loss of energy and an increase of the tap-to-tap time.

Taking a closer look at the overall energy balance of a typical electric arc furnace, it is possible to make an assumption about the energy saving potential. The energy input of an EAF consists of the following [2]:

1. Electrical energy, that is transferred to the (liquid) scrap via graphite electrodes
2. Energy supplied by natural gas burners, that decrease the time to melt the scrap and to avoid cold spots
3. Energy, that is released by exothermic reactions (i.e. oxidations) during the refining phase

Computing the input energy leads to the following representation [2]:

$$E_{Input} = \int_{t_{Charging}}^{t_{Tapping}} P_{Electric} dt + \Delta H_{NG-Burner} + \Delta H_{Oxygen-Injection} \quad (1.1)$$

$P_{Electric}$  ... Electrical power input

$\Delta H_{NG-Burner}$  ... Reaction enthalpy of natural gas

$\Delta H_{Oxygen-Injection}$  ... Reaction enthalpy caused by exothermic reactions

The output energy, that has to be equal to the input is obtained as [2]:

$$E_{Output} = \Delta H_{Slag} + \Delta H_{Steel} + \int_{t_{Charging}}^{t_{Tapping}} \Delta \dot{H}_{Offgas} dt + \int_{t_{Charging}}^{t_{Tapping}} \Delta \dot{Q}_{Cooling} dt + \int_{t_{Charging}}^{t_{Tapping}} \Delta \dot{Q}_{Radiation,OtherLosses} dt \quad (1.2)$$

$\Delta H_{Slag}$  ... Increase of the slag's enthalpy

$\Delta H_{Steel}$  ... Increase of the steel's enthalpy

$\Delta \dot{H}_{Offgas}$  ... Enthalpy flow rate (off-gas)

$\Delta \dot{Q}_{Cooling}$  ... Heat flow rate (cooling system)

$\Delta \dot{Q}_{Radiation,OtherLosses}$  ... Heat flow rate (radiation and other losses)

Finally, the conservation of energy leads to [2]:

$$E_{Total} = E_{Output} = E_{Input} \quad (1.3)$$

Figure 1.3 illustrates the energy balance (energy sources and sinks) of an EAF, together with typical values. What is more, this figure demonstrates, that up to three quarters of the input is due to electrical or chemical energy from natural gas/oil burners and, therefore,



mainly from fossile fuels [2].

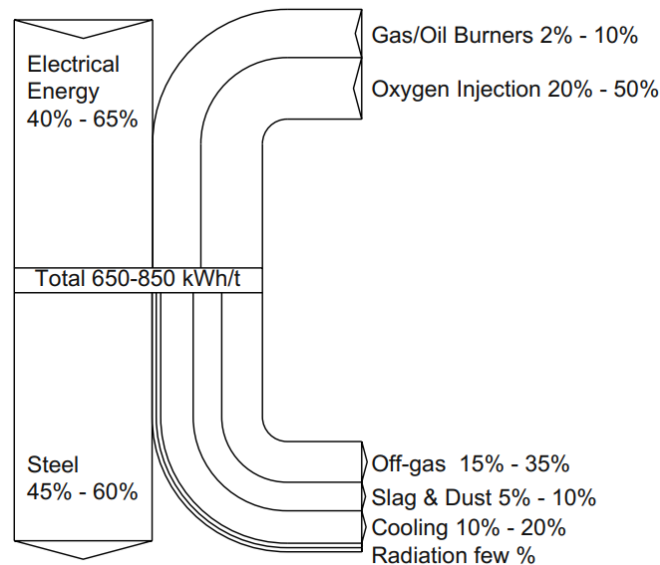


**Figure 1.3:** Energy Sources and Sinks in an EAF [2]

However, the  $CO_2$ -emissions are not solely due to the previously described sources, but are also caused by oxidation reactions during oxygen injection and the combustion of off-gas, see Figure 1.4.

The overall  $CO_2$ -emissions ( $m_{CO_2}/E_{Total}$ ) of electric arc furnaces in the steelmaking industry amount to approximately 0,11 to 0.21kg  $CO_2/kWh$  [2].

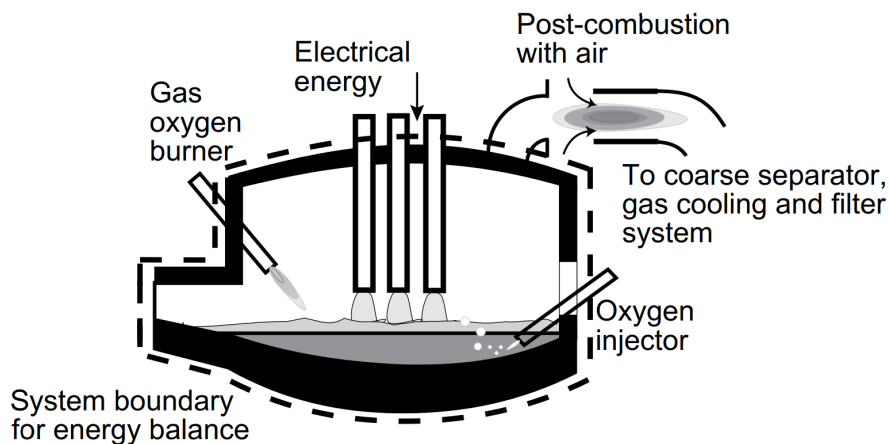


**Figure 1.4:** Main Sources of Carbon Dioxide in an EAF, adapted from [2]

In conclusion, equation 1.1 and 1.2 proof, that a reduction of the tap-to-tap time (i.e. by bypassing the issue of taking a sample of liquid steel with the aid of a sleeve) reduces the overall energy consumption of an EAF and therefore lowers the amount of  $CO_2$  for each produced ton of steel.

# Chapter 2

## Electric Arc Furnace

### 2.1 The Role of the Electric Arc Furnace in the Steel-making Industry

Generally, there are two different methods, separated by the iron source, to obtain steel as a raw material. One possible way is to use iron ore as the feedstock to transform it into its liquid state with the help of a blast furnace, that is fuelled by coke, or to receive DRI (direct reduced iron) or HBI (hot briquetted iron) through the process of direct reduction [6] [16]. The other possibility is to convert recycled scrap metal into liquid metal. Both, the final product of the direct reduction (briquettes or pellets), as well as the scrap, then get liquified with the help of electrical energy in the EAF.

Usually, the pig iron received from the blast furnace is transformed into molten steel with the help of a BOF (Basic Oxygen Converter). In this steelmaking process, the carbon content is reduced by injecting oxygen from approximately four percent to a value of 0.1-1% (mainly depending on the demands of the required steel quality). Furthermore, the overall sulfur and phosphorus content are also decreased in this step. A detailed overview of the mentioned processes (and their links to each other) in the steelmaking industry is illustrated in Figure 2.1. One of the major advantages of an EAF in comparison to a blast furnace is the reduced emission of toxic gasses. This pollution occurs due to the operation with coke that leads to emissions of  $CO$ ,  $CO_2$  or  $SO_2$ . However, converting scrap metal into steel grades of higher quality with specified demands on the chemical composition is often complicated, due to the fact, that scrap contains impurities such as nickel, chromium or copper, which are not removable in this process. This issue can be bypassed by separating the scrap before charging the furnace.

Further refining of the molten steel to the desired chemical composition is subject to secondary metallurgy. Here, any unwanted (non-)metallic inclusions or dissolved gaseous elements get removed with the assistance of a vacuum degasser or ladle furnace and the steel bath is brought to a temperature required for the following casting process [16].

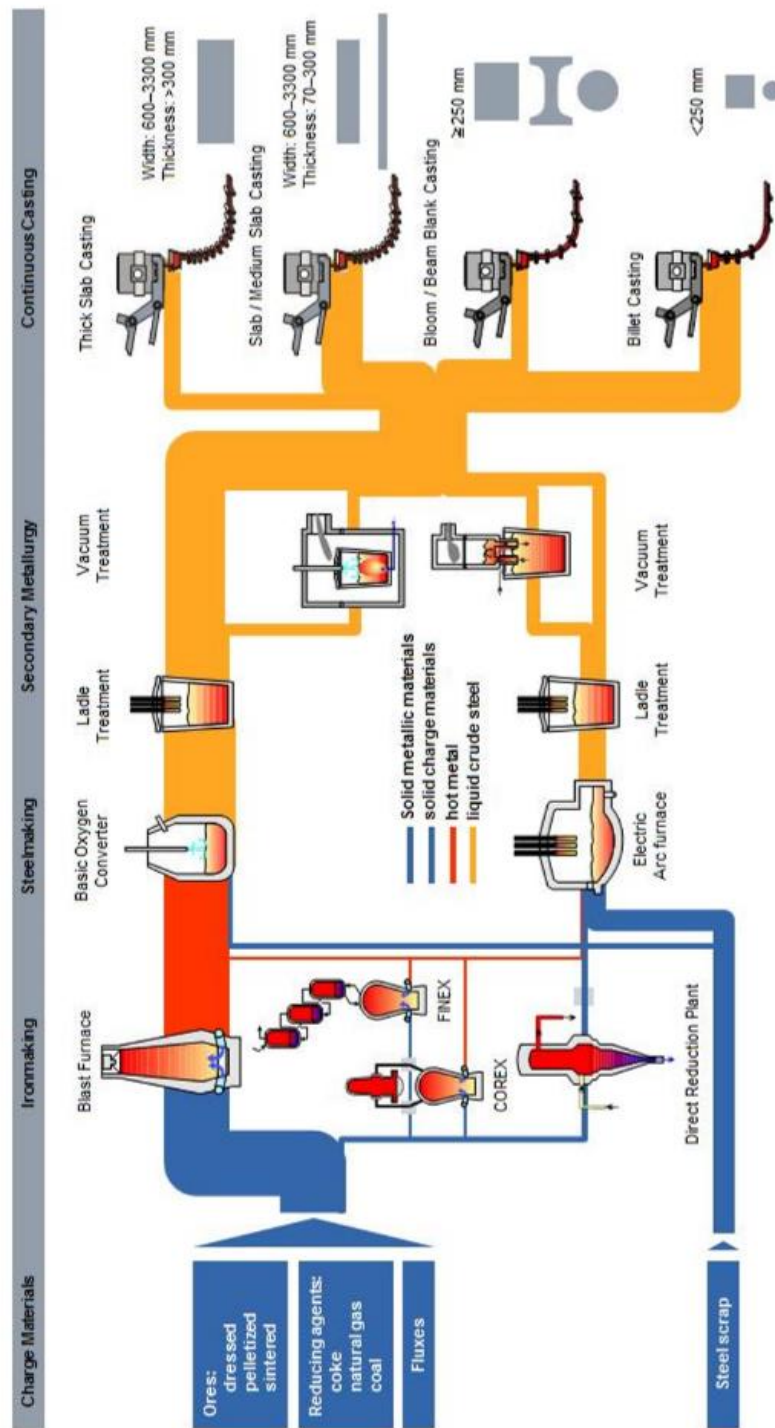


**Figure 2.1:** Overview of the Processes and their Links to Each Other in the Steelmaking Industry, adapted from [3]

### 2.1.1 The Process Stages During the Operation of an EAF

A tap-to-tap cycle of an electric arc furnace usually consists of these operations in the following order [6]:

- Charging of the Furnace
- Meltdown

- Refining
- De-Slagging
- Tapping

Conducting these operations, tap-to-tap times of around 60min are achieved. Modern EAFs, however, often skip the refining-process, which is later done in a ladle furnace. This lowers the tap-to-tap time to about 35-40min [3][6].

### **Charging**

In this step, both the roof part as well as the electrodes of the furnace are lifted to their top position and swiveled to the side, to allow the crane to deposit the scrap into the furnace's containment. An important aspect is to pre-select the scrap, since it later mainly determines the quality of the produced steel. Any additives, such as carbon or lime, may be included in the charge or added later via injection.

After the charging is done, the roof and the electrodes are moved back to their designated position. As the electrodes are lowered, an arc is established between the scrap and the electrodes, where the next stage, called *meltdown*, begins.

During a single tap-to-tap cycle, the process of charging can be done several times, depending on the volume of the containment and the density of the steel scrap. However, it is desirable to keep the number of backcharges as low as possible, since they decrease the productivity and cause energy losses of up to 10-20kWh/t of molten steel [6].

### **Meltdown**

During this operation, the scrap in the vessel is transformed into liquid steel, which is accomplished by the help of electrical and chemical energy. Usually, the chemical energy is supplied via oxy-fuel burners, that are fueled by natural gas, whereas the electrical energy is transferred to the scrap via graphite electrodes.

In the first part of the melting process, the so-called *boredown*-phase, the scrap pile gets penetrated by the descending graphite electrodes (see Figure 2.2), whereas their pace is mainly determined by the density of scrap and input power [5] [6].

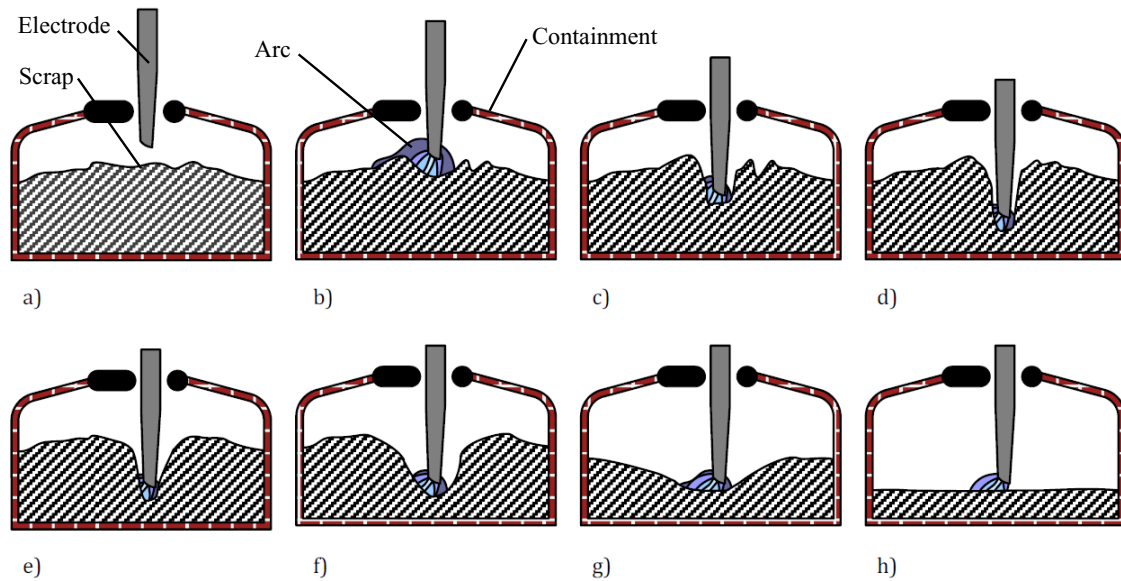


**Figure 2.2:** The Different Phases of the Meltdown Process, adapted from [4]

The parameter, that mainly determines the diameter of these pits, is the arc length, which is furthermore depending on the voltage. Thus, a higher voltage contributes to an increased diameter of the pits. Any material, that gets liquified, flows downwards and re-solidifies as it makes contact with "cold" scrap (see Figure 2.2 *a-e*), which rises the bulk density of material underneath the electrode.

According to [5], the boredown phase is finished, as the material beneath the arc reaches a density of approximately  $7t/m^3$ .

The next stage is known as *scrap collapse*. As the name implies, a slow descending and often a collapsing of the scrap pile into molten steel occurs (Figure 2.2 *f-g*). If there is a sufficient amount of liquified material in the vessel, often, oxygen is supplied, which therefore causes exothermic reactions with elements such as iron, phosphorus, carbon, silicon, manganese and aluminum. The metal oxides then may enter the slag phase. Carbon monoxide, that is created in this process, is either burnt inside the furnace, if there is a sufficient amount of oxygen present or escapes through the furnace exhaust. If the entire scrap has been transformed into the liquid state, the last stage of the meltdown, the *flat bath period* (Figure 2.2 *h*), is reached [5] [6].

During this phase, the furnace shell has to endure excessive heat loads due to radiant heat energy from the arc. In order to reduce these loads, the arc voltage has to be either lowered or the arc may be coated with foaming slag. The latter also rises the efficiency of the furnace, since the quantity of energy transferred to the steel bath gets increased.

Finally, before the refining process is initiated, the temperature of the steel bath is measured with the help of a sleeve and an attached thermocouple and a sample for the chemical analysis is taken [5] [17].

## Refining

During this operation, the contents of carbon, manganese, silicon, aluminum, sulfur and phosphorus are lowered. These impurities are partly removed as the transition into the slag phase. This is an important task, since the content of these impurities has a strong influence on the quality as well as the properties of the final steel product.

However, one major difference between an EAF and oxygen steelmaking is, that the basicity of the slag in an EAF is lower. What is more, the mass ratio of slag to steel is also lower, which leads to a limited capability of removing the mentioned impurities in an EAF. Table 2.1 depicts the typical constituents of slag in an electric arc furnace [6].

Constituents	Source	Rate of Composition
$CaO$	Charged	40 – 60%
$FeO$	Oxidation Product	10 – 30%
$SiO_2$	Oxidation Product	5 – 15%
$MgO$	Charged as Dolomite	3 – 8%
$MnO$	Oxidation Product	2 – 5%
$CaF_2$	Charged as Slag Fluidizer	
$S$	Absorbed from Steel	
$P$	Oxidation Product	

**Table 2.1:** Constituents of the Slag in an EAF [6]

Removing the phosphorus from the molten steel is usually accomplished by increasing the basicity of the slag, which can be done by charging the furnace with lime. On the other hand, this method raises the slag's viscosity, which in return hinders the removal of phosphorus. In order to bypass this issue, fluorospar is applied to the bath, which is beneficial for fluidizing the slag. This way, the content of phosphorus is lowered by 20-50% in an EAF.

The removal of the element sulfur is primarily achieved by sulfides, that are soluble in the slag, whereas the same conditions as described during the removal of phosphorus are leading to the desired result.

The final step of this operation includes the measurement of the bath temperature and taking a sample in the same way as mentioned in the meltdown phase [6].

## De-Slagging

In this operation, the impurities, that are dissolved in the slag during the meltdown and refining phase, get removed from the furnace over the slag door [6].

### **Tapping**

The tapping of the furnace is done as soon as the molten steel reaches the desired chemical composition as well as the proper temperature. This step involves the opening of the taphole and the tilting of the containment to transfer the molten steel into a vessel (i.e. a ladle). Usually, the steel is then processed in a ladle furnace, an equipment of the secondary metallurgy [3] [6].

## **2.2 Brief Historical Overview of Electric Arc Furnace Steel-making**

It was Sir William Siemens, who came up with the first construction of a working electric arc furnace, in 1878. However, due to the insufficient quality of carbon electrodes, that were barely capable of carrying the high currents, the poorly developed power grid and the expensive electrical power, it took more than 20 years until the first commercial electric arc furnace was established by Heroult in 1899. In this patent, Heroult described a furnace with one or more phases, creating arcs through the molten steel bath.

In 1906, the first one of these Heroult-furnaces went into operation in the steelplant Halocomb Steel Company in Syracuse, New York. This rectangular-shaped furnace had a capacity of 3,6t, utilized a single phase power and was equipped with two electrodes.

Three years later, in 1909, the first round-shaped three phase electric arc furnace with a capacity of 13,5t was established by the Illinois Steel Company. Since then, the vast majority of the EAFs in steel plants around the world are operated by AC current. The use of DC-powered furnaces in steel plants occurred much later, in the 1980s, due to their necessity of powerful rectifiers.

Today, the DC-EAFs make up 10% of all furnaces in steel plants [5], [6].

## **2.3 Construction of an Electric Arc Furnace**

Throughout the history of the electric arc furnace, the main focus of the research has been on the improvement of its productivity. This demand has been achieved by, among other things, increasing the size of the furnace, an improvement of the power input and reducing the power-off time with the help of faster moving furnace parts.

Basically, a modern electric arc furnace consists of the following components [6]:

- A containment, where the scrap is charged and gets transformed into molten steel
- Components, responsible for supplying the furnace with electrical power

- Parts and modules, that enable certain movements of the EAF (i.e.tilting of the vessel)

A detailed overview of a modern EAF is depicted in Figure 2.3

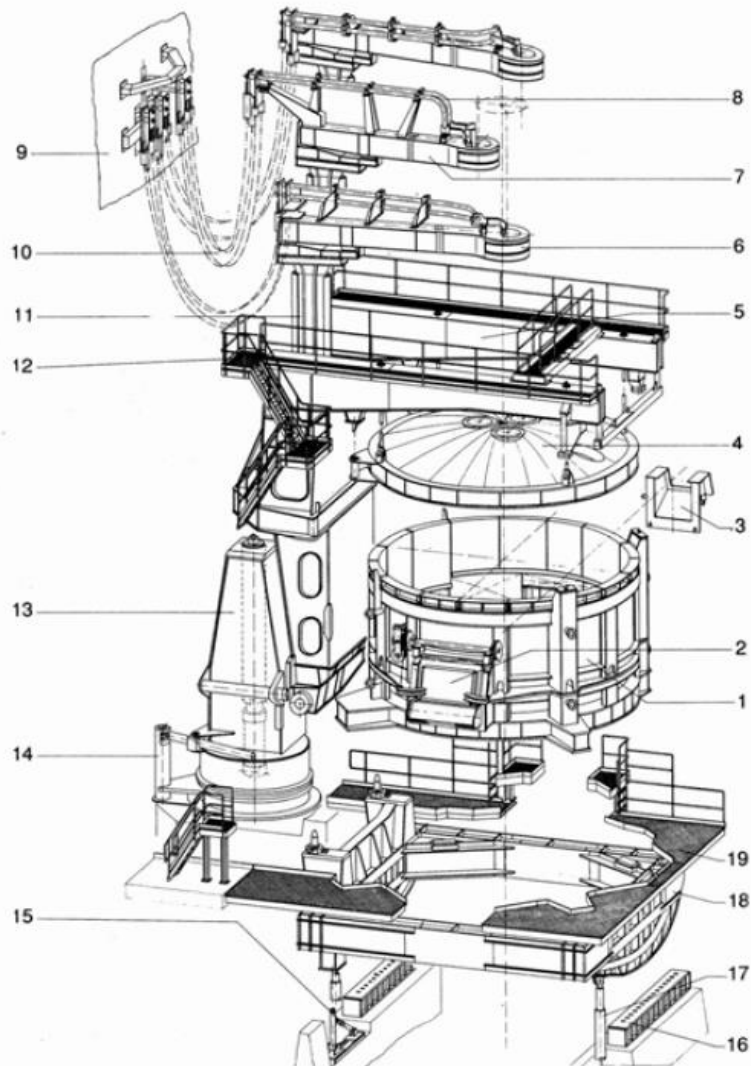


**Figure 2.3:** Parts of an Electric Arc Furnace, adapted from [3]

- |                              |                                  |                      |
|------------------------------|----------------------------------|----------------------|
| 1...Shell                    | 2...Door                         | 3...Pouring Spout    |
| 4...Roof                     | 5...Roof Suspension              | 6...Electrode Holder |
| 7...Electrode Supporting Arm | 8...Conducting Copper Pipe       | 9...Transformer Room |
| 10...Water Cooled Cables     | 11...Electrode Lifting Mechanism | 12...Passage         |
| 13...Roof Lifting Mechanism  | 14...Roof Swiveling Mechanism    | 15...Furnace Mount   |
| 16...Rocker Rail             | 17...Tilt Cylinder               | 18...Rocker          |
| 19... Working Platform       |                                  |                      |

### 2.3.1 Containment of an EAF

The containment of a furnace has a cylindrical shape, whereas the bottom is spherical and the roof part resembles a flattened sphere. The spherically shaped furnace bottom



is usually made of a steel shell, which is covered by refractory, that acts as an insulator. Both, the roof and the panels of the containment, that are placed above the slag-line (the top level of the liquid bath), are water cooled. This helps to enable higher heat input rates and should avoid any critical thermal expansion of the cage, that may lead to warping or unwanted gaps between the panels. What is more, these structural parts of the furnace also have to be designed to endure high mechanical stress, that occurs when the EAF is charged with scrap. Thus, the panels should have a sufficient wall thickness in order to have the ability to withstand these forces. In contrast to that, if the wall thickness is too high, the heat transfer to the cooling water gets minimized, which is also not desirable. In general, mainly depending on the heat input and the workload of the furnace, the wall thickness lies between 8-10mm. Generally, these panels contain pipes, where the water is flowing, in order to provide sufficient cooling. The preferred material for such pipes is boiler tube steel with a diameter of 70-90mm, since it features an adequate thermal conductivity of  $50W/mK$  at a reasonable price.

However, in areas of the furnace, where excessive heat loads might occur (e.g. around the level of the molten steel bath) the boiler tube steel gets replaced by copper, since it has an even higher thermal conductivity of  $383W/mK$  and thus enables a better heat transfer rate to the cooling water. Due to the fact, that the furnace is not operated at a constant temperature, the panels are exposed to a certain quantity of thermal cycling, which mainly determines their period of application. In order to increase their lifespan, both a high cooling rate as well as a low heat flux to the panel should be achieved, which seems to be a contradictory requirement. A good compromise, that satisfies these two demands, is to support the build-up of a layer of slag on the panels, since it acts as an insulator with its low thermal conductivity of  $0,12-0,13W/mK$ . In order to enhance the adhesion of the slag coating, bolts and cups are placed onto the surface of the panels. However, it is important to consider, that the temperature difference in the cross section of the panel should not exceed a critical value, where the mechanical stress (compression and tension) due to thermal expansion is greater than the yield strength of the panels' material. Otherwise, an irreversible deformation will occur, that causes cracks and might lead to a complete failure of the panels.

In order to avoid any formation of steam bubbles in the pipes, which transfer the heat ten times worse than water, the flow velocity should be in a range of 1,2-2,5m/s. Only in areas that are exposed to extremely high temperatures (i.e. the slag line), a higher velocity of the flowing water (5m/s) is unbearable to suppress any accumulation of steam bubbles [6].

### 2.3.2 Electric Circuit of an EAF

#### AC-Circuit

Due to the fact, that modern industrial EAFs consume approximately  $375kWh$  of electrical energy to melt one ton of scrap, it is essential to obtain this energy from the high voltage grid. In order to make the voltage easier to handle at the steel plant, a transformer is used to step it down from  $100-500kV$  to  $30-35kV$  (see Figure 2.4). On the primary side of the furnace transformer, there is usually an isolator, a vacuum switch, that acts as a circuit breaker and a reactor, which is used to regulate the line reactance. The secondary side of the furnace transformer delivers a voltage in a range of several hundreds of volts, that is capable of providing a stable arc and a current of several kilo amperes. This transformer is in most cases located next to the furnace, with the purpose of minimizing the ohmic losses in the supply cables [5].

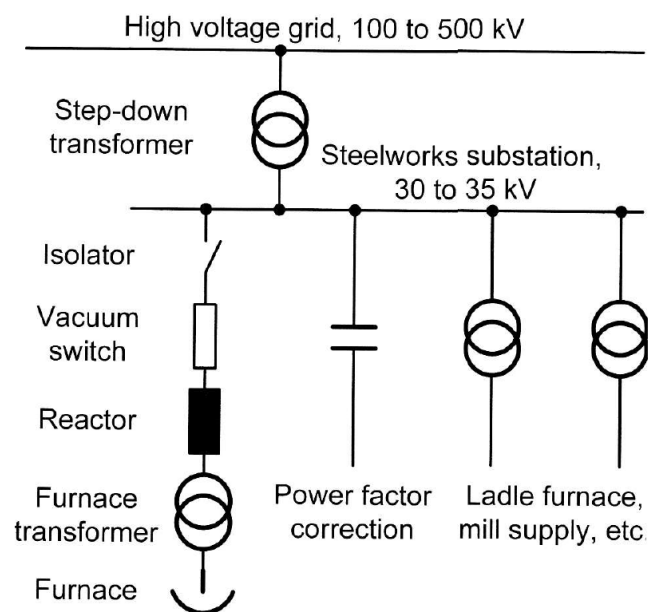


**Figure 2.4:** Schematic Overview of a Steelworks' Power Grid [5]

An important aspect when designing a power supply of the steel plant is to consider the installation of a so-called *power factor correction*. This system is necessary, due to the poor power factor of the furnace, which is around 0,7 and therefore helps to lower the losses in the grid [5].

A schematic overview of the high current system is provided with the help of Figure 2.5. This high current system consists of the following parts:

- High current busbar system

- Cables
- Electrode supporting arms
- Electrode clamp
- Graphite electrode

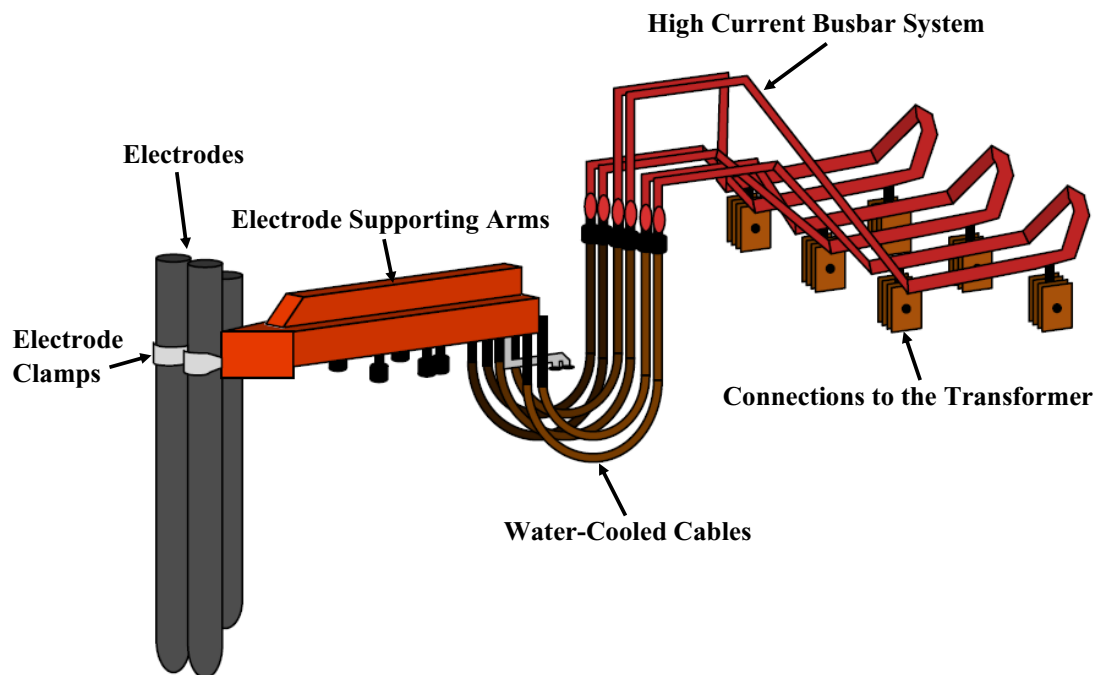


**Figure 2.5:** High Current System of an EAF, adapted from [4]

From the secondary side of the transformer, a high current busbar system is responsible for the connection of the furnace transformer and the high current cables. Mainly depending on the required power input, the busbar system is either made of copper plates, that are cooled by convecting air (allows a current density of up to  $1,5A/mm^2$ ) or the most common way are water-cooled pipes (allow a current density of up to  $9A/mm^2$ ). Since these plates or pipes are directly mounted to the wall of the transformer's house, it is inevitable, that the area of this wall does not contain any iron to avoid any arcing or inductive heating. Due to the fact, that the electrode supporting arms are moveable and the furnace itself often gets tilted (i.e. during the process of tapping), the connection from the busbar system to the electrode supporting arms is established with the help of flexible high current cables. The cables, that are made of stranded wire ropes, are also usually water-cooled to enable maximum current densities of  $6-7A/mm^2$ . Another important design aspect is to keep the reactance of the cables (approx.  $0,1m\Omega/m$ ) as low as possible, with the goal of minimizing the ohmic losses [7].

When it comes to the electrode supporting arms, their main functions are holding the

electrodes in position and providing them with current from the cables. Usually, the supporting arms are attached to a stool of the electrode lifting column, which is responsible for adjusting the height of the electrodes [7].

Basically, there are three different design-concepts [7]:

- **Conventional design:** The main purpose of the supporting arms made of steel is to keep the current conducting copper pipes and the electrodes in place. Since the arms remain currentless, both the copper pipes and the electrode clamps are isolated. Figure 2.6 (*centre and left*) shows, how this design may look like in a real application.
- **Design manufactured from aluminum:** In this version (Figure 2.6, *left* and 2.7), the arm is manufactured from aluminum and also responsible for conducting the current. The reactance is kept low with this design, since almost the whole cross section of the arm body is available for the current conduction (penetration depth is mainly determined by the frequency: *skin effect*). In comparison to the copper-plated version, the current densities are limited to values of  $2\text{-}3\text{A}/\text{mm}^2$ , which requires bigger dimensions of the arms.
- **Design manufactured from copper-plated steel:** In modern steelmaking plants, this is the preferred version (Figure 2.6, *left* and 2.7), since it features a high stiffness and allows a greater current density of  $6\text{-}9\text{A}/\text{mm}^2$  (depending on the thickness of the copper plates), in comparison to the previously described arms made of aluminum.

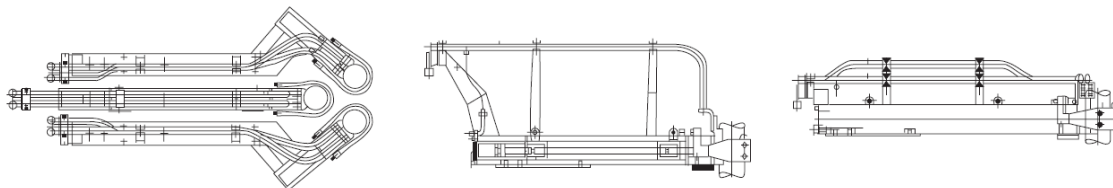


**Figure 2.6:** Overview of the Different Electrode Supporting Arm Designs [6]

The connection between the graphite electrodes and the supporting arms is accomplished by electrode clamps (see Figure 2.8 and 2.9). What is more, these clamps are responsible for conducting the current to the electrodes, which is usually done by conductive pads manufactured from copper [6].

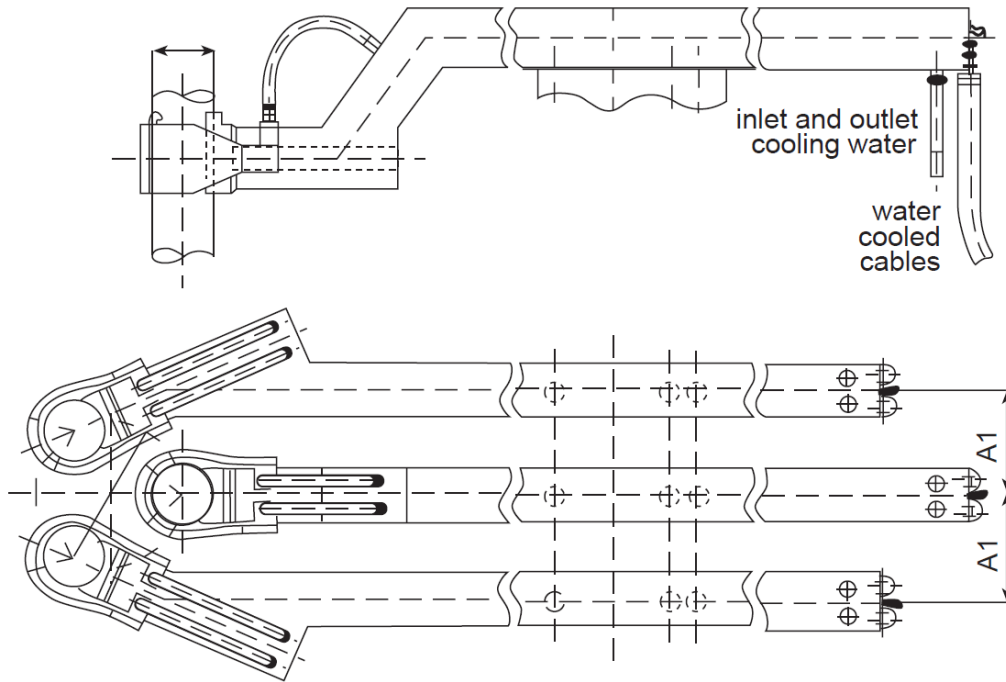


**Figure 2.7:** Side and Top View of Electrode Supporting Arms [6]

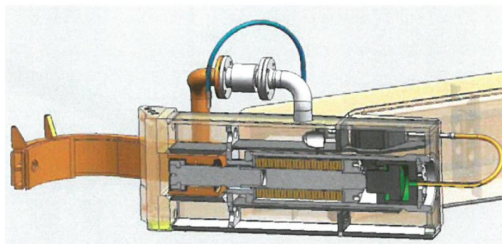


**Figure 2.8:** Cross Section of an Electrode Clamp [7]



**Figure 2.9:** Front View of Electrode Holder [6]

The graphite electrodes are responsible for transferring electrical energy to the scrap with the aim to melt it down and later for heating up the molten steel to the desired temperature. These electrodes are exposed to temperatures of up to 11000K [5] and a high amount of thermal cycling. Hence, graphite is the preferred material, due to its excellent heat resistance, a sufficient electrical conductivity, a low chemical reactivity (oxidation appears at temperatures higher than 500°C) and a good resistance against thermal shock, due to its low thermal expansion rates. The raw materials required to manufacture such cylindrically shaped graphite electrodes for an electric arc furnace are petroleum needle coke (a product of crude oil), coal tar pitch (a product of coal) and additives [6] [7].

The diameter mainly depends on the electrode current, which is depicted in Figure 2.10.

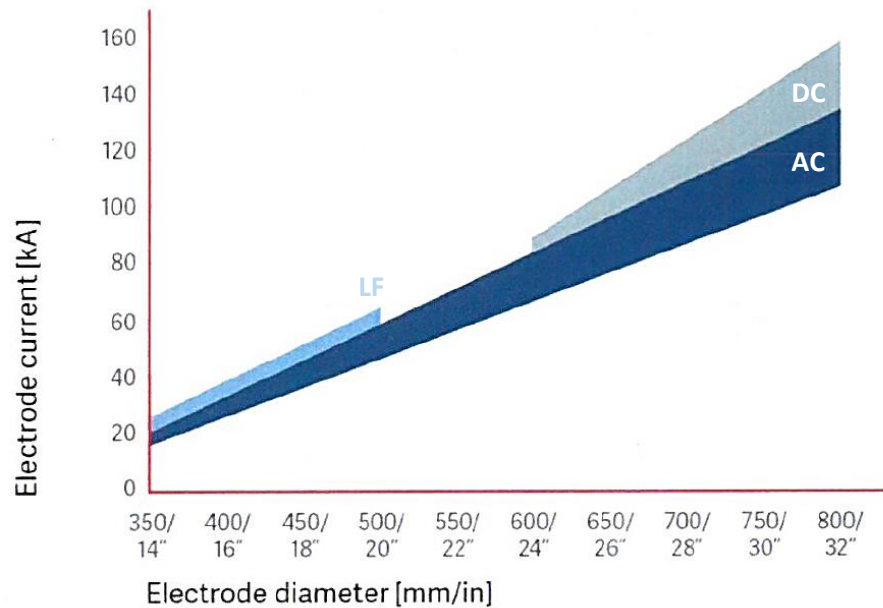


**Figure 2.10:** Diameter of the Electrode Depending on the Current [7]

A schematic overview of the manufacturing process is shown in Figure 2.11 and includes the following steps [6] [7]:

1. *Grinding and mixing the raw materials (petroleum needle coke, coal tar pitch and additives)*
2. *Extrusion of the mixture to get it into a cylindrical shape*  
Green electrode sections are created
3. *Baking the green electrodes at around 800°C*  
In this process, the electrodes turn into brittle carbon. Any gas build-up caused by high thermal gradients inside the material should be avoided, since they might cause cracks. Thus, this production step requires three to four weeks of time.
4. *Impregnation of the porous electrodes*  
During the *impregnation*, the pores, that were formed during the evaporation of gases in the baking process, are filled with pitch to support solidification. Hence, the density and the strength of the electrode material are increased.
5. *Re-baking of the impregnated carbon to transfer the pitch into carbon*
6. *Graphitization*  
In the step of *graphitization*, the electrodes are heated up to a temperature of around

3000°C by passing a direct current of 100kA through them. The amorphous structure transforms into a layer structure, that is typical for graphite. This transformation is desirable, since it improves mechanical, thermal and electrical properties of the electrodes.

### 7. Machining

The dimensions of the electrode, such as the diameter, are machined with the help of a lathe.

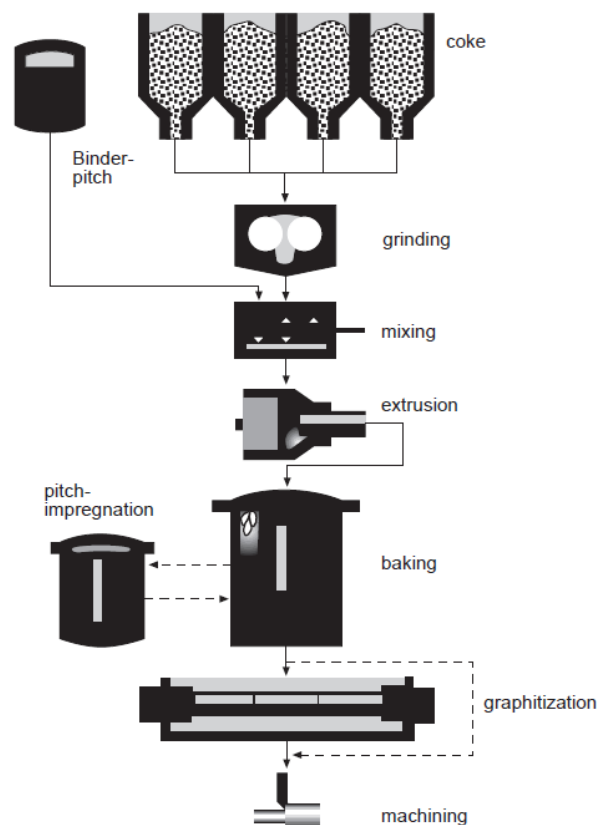


**Figure 2.11:** Overview of the Manufacturing Steps of a Graphite Electrode [6]

## 2.4 Fundamentals of a Plasma

The term *plasma* characterizes a partially or completely ionized gas (it consists of ions and electrons) and was first described by Irving Langmuir in 1923. Since a plasma consists of ions and electrons, its constituents are attracted to each other due to the electrostatic Coulomb-force. Some important physical properties include the shielding of electrical fields, electrical conductivity and the interference with magnetic fields [18].

### 2.4.1 Classifications of Plasmas

Basically, there are two classes of plasma, that distinguish from each other by the temperature of its electrons  $T_e$  [18]:

- **High temperature plasma** (Temperature of the electrons  $T_e \geq 10^5 K$ ):  
The gas solely consists of ionized atoms. Examples: Fusion plasmas, stars
- **Low temperature plasma** (Temperature of the electrons  $T_e \leq 2 * 10^4 K$ ):  
Partial ionization of the gas means, that beside the electrons and ions, also neutral atoms are present.
  - **Non-thermal plasma:**  
The electrons get heated up, while the ions remain cold. ( $T_i \approx 300K$ )
  - **Thermal plasma:**  
An exchange of energy between electrons and ions occurs. Furthermore, the temperature of the ions  $T_i$  is approximately the same as that of the electrons  $T_e$ , i.e. ( $T_i \approx T_e$ )

### 2.4.2 Important Physical Properties of Plasmas

#### Electrical Conductivity

Both, the energy consumption, as well as the stability of an arc are mainly determined by the electrical conductivity of a plasma. In further consequence, the conductivity is primarily depending on the ionization energy. Figure 2.12 depicts the electrical conductivity of the gaseous elements  $Ar$ ,  $He$ ,  $H_2$  and  $N_2$  in dependence on the temperature. It is important to point out, that  $He$  has the lowest conductivity, which can be explained by its high ionization energy [8].



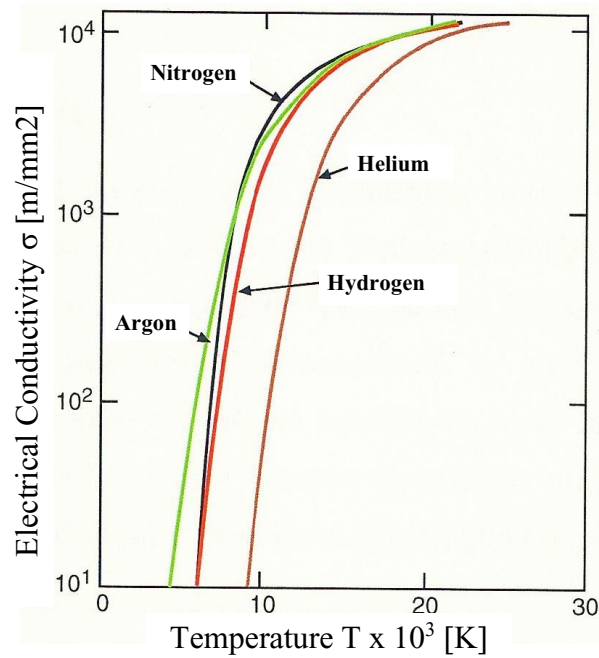


**Figure 2.12:** Electrical Conductivity of *Ar*, *He*, *H<sub>2</sub>* and *N<sub>2</sub>*, adapted from [8]

### Enthalpy

One important aspect in terms of enthalpy of plasmas is the fact, that monoatomic gases (i.e. *He*, *Ar* or *Ne*) have a lower enthalpy than gases with two or more atoms (i.e. *O<sub>2</sub>*, *N<sub>2</sub>* or *H<sub>2</sub>*) at same temperatures, see Figure 2.13. This phenomenon is explained by the fact, that gases with two or more atoms dissociate at higher temperatures. Monoatomic gases show such a significant rise of enthalpy at temperatures of approximately 10000°C.

Such an increase of the plasma's enthalpy (i.e. by purging the area around the plasma with hydrogen) is often desired, for instance if a higher melting rate is requested. However, gases as Argon may be used, since its low ionisation temperature enables a better ignition and stabilization of the arc. What is more, argon also acts as an inert gas [8].

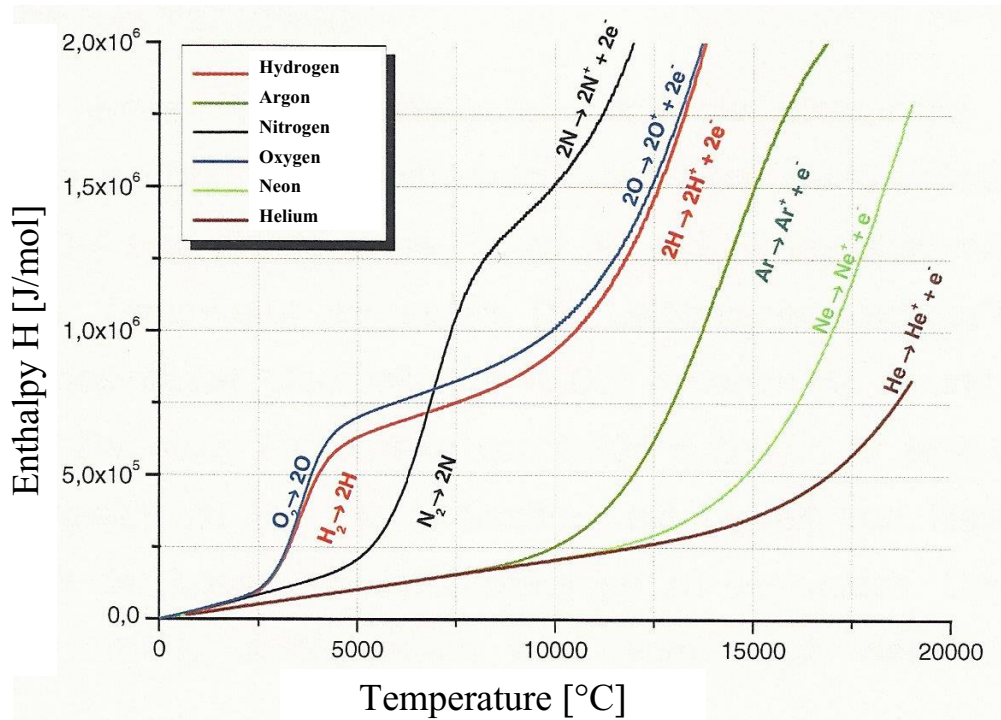


**Figure 2.13:** Enthalpy of  $H_2$ ,  $Ar$ ,  $N_2$ ,  $O_2$ ,  $Ne$ ,  $He$  as a Function of the Temperature, adapted from [8]

### 2.4.3 Some Examples of Plasmas

In this context, the most important examples of plasmas shall be depicted [18],[8]:

- **Gas discharge:**

The electrons are accelerated in the presence of an electrical field and their ionization happens due to their collisions with each other. Usually, this acceleration is achieved with two opposing electrodes, a cathode (negative electrode and source of electrons) and an anode (positive electrode). Common examples of gas discharge are arcs, sparks, glow discharges or dark electrical discharges.

- **Flames:**

The process of heating and ionization is achieved with the help of a chemical reaction (i.e. oxidation). Temperatures are limited by the dissociation of the molecules ( $T \approx 10^4 K$ ).

- **Light-induced plasma:**

Inducing a plasma through photo-ionization, which can be achieved with a powerful laser, for instance.

### 2.4.4 The Process of Ionization

The ionization of atoms is inevitable, when it comes to the creation of a plasma. During this process, which occurs numerous times in a real plasma, an atom acquires a positive charge (it becomes an ion with almost the same mass), while losing an electron, which possesses a relatively small mass in comparison to the ion. In order to achieve such an ionization, a certain amount of energy, usually in the form of electrons or photons in the case of a plasma, has to be transferred to the atom, known as the so-called *ionization energy*. Since this energy is required to remove an electron from the atom's outer shell, the *ionization potential* is a specific constant for each element. Some examples are shown in Table 2.2 [8].

Element	Ionisation Energy $E_i$ [eV]
<i>Ar</i>	15.76
<i>H</i>	13.6
<i>He</i>	24.58
<i>N</i>	14.55
<i>O</i>	13.62
<i>Cu</i>	7.72
<i>W</i>	7.97
<i>Na</i>	5.14

**Table 2.2:** Ionisation Energy of Some Elements [8]

Considering the ionization due to impacts of electrons, approximately only one third of all impacts have a sufficiently high energy required to knock an electron out of an atom's shell. The remaining two thirds of these impacts only change the speed of the atoms after the collision, or promote them to an excited state.

The reversal process to the ionization is called *recombination*, where the positively charged ion receives an electron and becomes a neutral atom again [8].

### 2.4.5 Arcs in Industrial Furnaces

Mainly depending on the size of the furnace, the arc voltage is typically within the range of 100 to 800V, whereby the currents reach from about 10 to 150kA. Therefore, large scale electric arc furnaces are capable of consuming an electrical power of 100MW and beyond.

Generally, there are two types of industrial electric arc furnaces, that are distinguished from each other through the characteristics of their power supply: AC- and DC- furnaces. However, mainly explained by the need of elaborated technology to rectify the current, the DC-furnace only constitutes to ten percent of the EAFs in modern steel plants [5].

### **Arcs in AC-Furnaces**

Depending on the electrical grid, the electrodes in an AC-powered furnace switch their polarity 50 to 60 times each second, meaning, that both the graphite electrodes and the steel (bath) act as cathodes and anodes. During the process of switching the polarity, the current decreases and eventually reaches zero. Mainly depending on the thermal capacity of the remaining plasma between anode and cathode, the arc either extinguishes or continues. Both, an instant and sufficiently high enough input from the power supply are beneficial for a continuing arc [5]. However, the measurements conducted during the research process for this master's thesis require a stable and continuing arc.

What is more, high speed photographs in industrial electric arc furnaces have shown, that the arc diameter is much smaller than that of the graphite electrode. Due to this fact, the arc is able to move across the tip of the graphite electrode, which leads to a changing length of the arc [5].

#### **2.4.6 Atmosphere in a Steelmaking Electric Arc Furnace**

In general, explained by the fact, that metals in their vaporous phase, have significantly lower ionization potentials, in comparison to gasses, such as oxygen, nitrogen or carbon monoxide, they are mainly responsible for providing their electrons. This means, that the characteristics, such as radiation density or electrical conductivity of the plasma, that carries the arc, is mainly determined by the properties of the metallic vapor.

Since scrap, that is charged into industrial EAFs, may also contain galvanized metal, the zinc from this coating evaporates during the melting at temperatures below 800°C. Due to its low ionization potential, zinc therefore increases the electrical conductivity of the plasma.

Non-metallic elements, such as hydrogen might also be supplied to the furnace's atmosphere, due to the dissociation of water from wet scrap or from natural gas burners. In addition to this, carbon monoxide, as well as carbon dioxide are mainly formed during the oxygen injection [5].

# Chapter 3

## Atomic Spectroscopy

The term *spectrum*, when used in physics or chemistry, describes a spread (or range) of wavelengths.

It was Sir Isaac Newton in 1667, who first observed the spectrum of visible light by dispersion, with the help of a simple prism. Roughly two centuries later, in 1859, Kirchhoff and Bunsen came up with the first spectroscope with the purpose of using it for chemical analysis. This crude version of a spectroscope consists of a light source (e.g. a flame), an entrance and exit slit, two lenses and a prism (see Figure 3.1) [9].

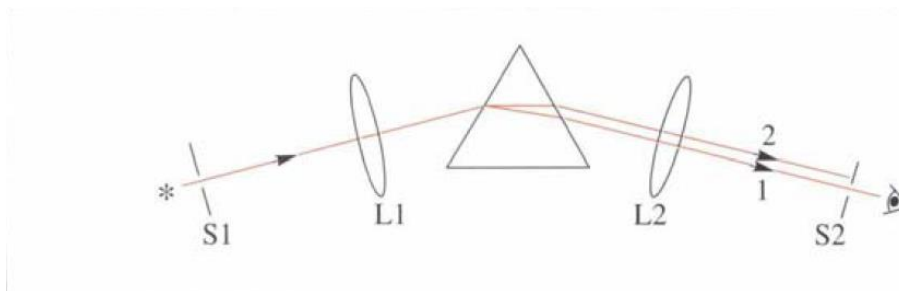


**Figure 3.1:** Principle of a Crude Prism Spectroscope [9]

The light from the source travels through the entrance slit and gets then dispersed by the prism. To ensure, that the separated rays are distinguishable from each other, the prism is rotatable, so that only one ray is capable of passing through the exit slit and therefore observable by the spectator. Considering *ray 1* has the wavelength  $\lambda$  and *ray 2*  $\lambda + d\lambda$ , where  $d\lambda$  represents a short step width. Therefore, the resolution of a spectroscope corresponds to the smallest value of  $d\lambda$ , where the two rays are just separately observable [9]. Nowadays, atomic spectroscopy plays a major role in chemical analysis, when it comes to determining the chemical composition of a given sample. However, there are three different forms of atomic spectroscopy (emission, absorption and fluorescence spectroscopy), mainly separated by the physical principle behind it. Figure 3.2 depicts the main characteristic differences between the three forms of atomic spectroscopy. In atomic emission spectroscopy, a flame or more commonly, a plasma is used as a source to get some atoms of the sample from the ground to their corresponding excited electronic states. When re-

turning back to their ground states, the electrons emit a photon with their characteristic wavelengths. The intensity of the emitted photons is proportional to the elements' concentration in the inspected sample [10].

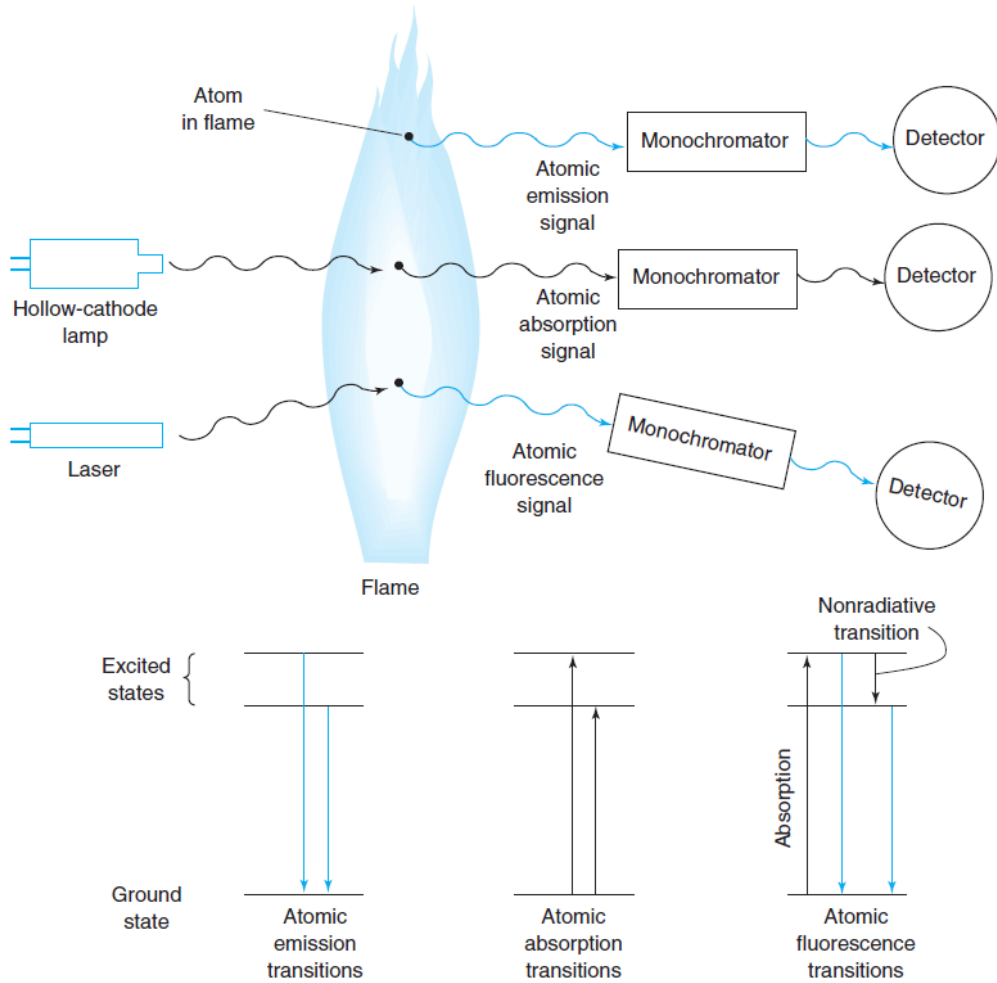


**Figure 3.2:** Schematic Illustration of the Three Forms of Atomic Spectroscopy [10]

Atomic absorption spectroscopy uses a light source (e.g. a hollow-cathode lamp) to emit photons, which then get partially absorbed by the atoms of the analysed sample. Photons, that are not absorbed, will then be measured by a detector to determine the concentration of this element. A flame with a temperature of approximately 2000-3000K and a path-length of about 10cm is utilized to evaporate and break the sample into its single atoms (atomization). Another important part of this type of spectroscopy is the light source, where a hollow-cathode lamp is usually used for. The hollow-cathode of this lamp is made out of the same element as the one to be analysed. The glass body is filled with argon or neon at a slightly low pressure of 130-700Pa. When a voltage of around 500V is applied to the electrodes, the cations of the ionized gas are accelerated towards the negatively charged cathode. The amount of energy obtained during this acceleration is sufficiently high to remove metal atoms from the cathode. These energetic  $Ar^+$ - or  $Ne^+$ -

ions (depending on the gaseous filling of the lamp) excite the  $Fe$ -atoms of the cathode, so that these  $Fe$ -atoms emit a photon with the same frequency of the one, that gets absorbed by the sample in the flame. The detector then counts the photons, that have not been absorbed. Due to the fact, that these  $Fe$ -atoms have a significantly lower temperature than those in the flame, the width of the emitted line by the hollow-cathode lamp is smaller than the width of the line absorbed by the atoms in the flame. Therefore, the light emitted by the hollow-cathode lamp can be considered as almost *monochromatic*. Since the analysed element has to correspond to the material of the lamp's cathode, a different lamp is required when examining a different analyte [10].

### 3.1 The Effect of Temperature on Spectroscopy

The temperature plays a major role in spectroscopy, since it mainly determines to which extent the analyte is atomized. Furthermore, a higher temperature is beneficial for increasing the ratio of atoms in their excited states to those in their ground states, which has a significant influence on the intensity of the observed signal.

Assuming a thermal equilibrium, the *Boltzmann-Distribution* helps to describe the ratio of the populations in the ground and excited state. At any given energy level of an atom or molecule in the sample, there might be one or more possible states. The term *degeneracy* describes, how many states at a certain energy level are possible.

The Boltzmann Distribution is given as [10]:

$$\frac{N^*}{N_0} = \frac{g^*}{g_0} e^{-\frac{\Delta E}{k_B T}} \quad (3.1)$$

With,

$N^*$ ...Population of atoms in the excited state

$N_0$ ...Population of atoms in the ground state

$k_B$ ...Boltzmann's constant ( $k_B = 1.381 \cdot 10^{-23} JK^{-1}$  [19])

$g^*$ ...Degeneracy of the excited state

$g_0$ ...Degeneracy of the ground state

Considering the following example of sodium: The energy gap  $\Delta E$  between the ground and the lowest excited state of sodium amounts to  $3,371 \cdot 10^{-19} J/atom$ , whereas the corresponding degeneracies are 1 and 2. Calculating the relative populations of these two states at a temperature of  $2600K$  (e.g. in a flame, where a mixture of acetylene and air gets burnt) leads to [10]:

$$\frac{N^*}{N_0} = \frac{2}{1} e^{-\frac{3,371 \cdot 10^{-19}}{1,381 \cdot 10^{-23} \cdot 2600}} = 1,6738 \cdot 10^{-4} \quad (3.2)$$

According to this computation, approximately 0,017% of all sodium atoms are in their excited state. Increasing the temperature by 10K also rises the number of atoms in their excited state [10]:

$$\frac{N^*}{N_0} = \frac{2}{1} e^{-\frac{3,371 \cdot 10^{-19}}{1,381 \cdot 10^{-23} \cdot 2610}} = 1,7351 \cdot 10^{-4} \quad (3.3)$$

This example depicts, that an increase of the temperature by 10K also increases the fraction of atoms in their excited state by [10]:

$$A = G \frac{P}{100} \quad (3.4)$$

$$p = \frac{100 \cdot A}{G} = \frac{100 \cdot (1,7351 - 1,6738) \cdot 10^{-4}}{1,6738 \cdot 10^{-4}} = 3,6623\% \quad (3.5)$$

With,

$p$ ...Percentage

$G$ ...Original value

$A$ ...New value

Due to the fact, that the intensity of the emission is proportional to the atoms in the excited state, a temperature rise of 10K therefore increases the emission intensity by almost 4% (in the case of sodium). This is why a stable flame is inevitable to obtain a stable signal, that does not vary too much in its intensity. Hence, an inductively coupled plasma is the preferred excitation source in emission spectroscopy, since it is capable of delivering a stable temperature.

In contrast, in atomic absorption spectroscopy, an unstable flame with a varying temperature does not have the same significant effect on the observed signal [10].

## 3.2 The Process of Atomization in Spectroscopy

The most important part in spectroscopy is the process called *atomization*, where the given substance (also named *analyte*) gets broken into single atoms. Subsequently, some of these atoms are promoted to an excited state, which can be achieved with the help of a flame, a heated furnace or a plasma [10].



### 3.2.1 Atomization with the Help of an Inductively Coupled Plasma

The inductively coupled plasma is capable of delivering a stable temperature of 6000 to 15000K. Due to this reason, it is mainly used to simultaneously detect single elements in a sample.

An inductively coupled plasma-burner is depicted in Figure 3.3. On the top of the shown cross section is a quartz bonnet, that holds two turns of an induction coil (operating frequency is 27 or 41MHz) in place. Argon is used as a plasma gas, that gets fed in the corresponding inlet. With the aid of a tesla coil, the argon gets ionized and the free electrons are then accelerated by the field of the radio-frequency coil. Through collisions of these electrons with atoms of the argon, the entire gas is heated up [10].

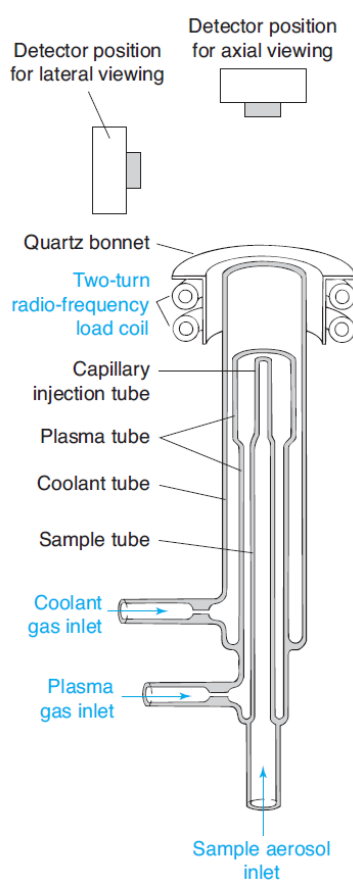


**Figure 3.3:** Cross Section of an Inductively Coupled Plasma Burner [10]

Instead of evaporating the solvent with the plasma, specific nebulizers are utilized, with the purpose of using all the plasma's energy for the atomization. A cyclone nebulizer (Figure 3.4) helps to transfer the liquid sample into a fine mist, which is then introduced into the plasma torch. In order to lower the detection limit for e.g. a specific element in the analyte, an ultrasonic nebulizer, see Figure 3.5, is used. The sample solution is applied onto a piezoelectric crystal oscillating at a frequency of around 1MHz. The vibration of the crystal causes the liquid sample to transition into a fine aerosol, which is

then led through a heated tube to evaporate the solvent. As soon as the stream enters the cooled zone, condensing solvent gets removed. In the last section, any remaining vaporous solvent is removed with the help of a PTFE-membrane and flowing argon, so that only desolvated dry aerosol gets redirected to the plasma [10].

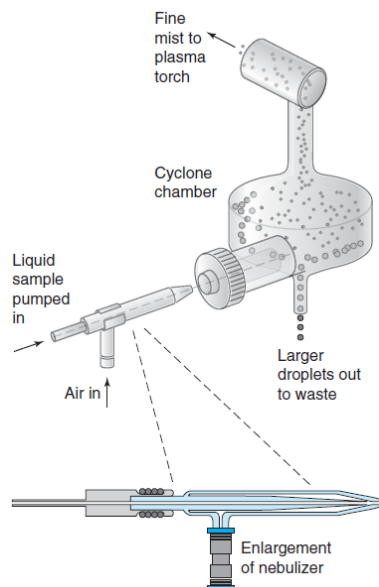


**Figure 3.4:** Working Principle of a Cyclonic Nebulizer [10]

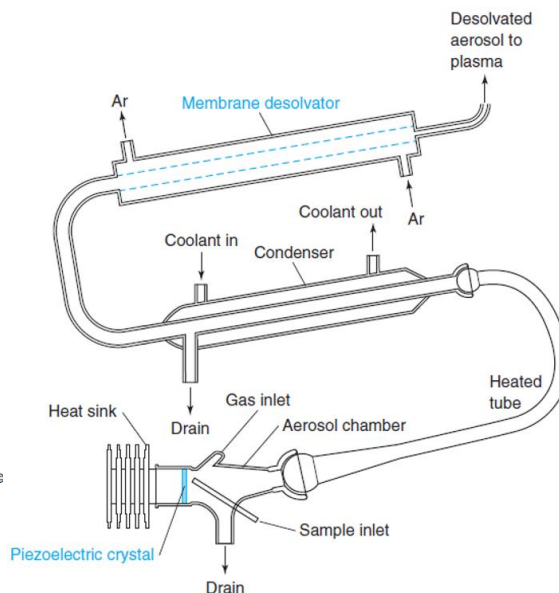


**Figure 3.5:** Cross Section of an Ultrasonic Nebulizer, adapted from [10]

### 3.2.2 Atomization with the Help of a Flame

Commonly, the main component of a flame spectrometer is a so-called *premix burner*, as shown in Figure 3.6, that is responsible for mixing fuel, the analyte and oxidizer. The flowing oxidant (in most cases air) causes the liquid sample to transition into a fine mist in the section of the pneumatic nebulizer. Subsequently, the nebulized analyte passes a glass bead, which is beneficial to form particles of a smaller size. The baffles, which are located under the burner head prevent any large droplets of analyte from entering the flame. Any remaining liquid sample is gathered at the bottom, to exit the spray chamber over the drain [10].

Usually, in flame spectroscopy, a mixture of acetylene (fuel) and air (oxidant) is utilized to maintain a flame temperature of 2400-2700K. In the case of so-called *refractory elements*, that require a higher temperature for the atomization process, due to their higher boiling points, nitrous oxide is used instead of air as oxidizer.

When observing the signal from a flame spectroscope, the fact, that the flame itself also emits photons, has to be taken into account. Hence, this emitted light has to be subtracted from the observed signal, in order to acquire the signal of the analysed sample.

The cross section of the flame is depicted in Figure 3.7. As soon as the mixture of fuel,

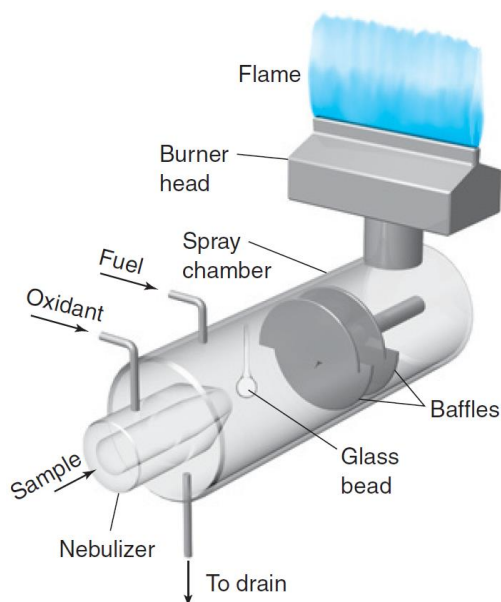


**Figure 3.6:** Parts of a Premix Burner, adapted from [10]

oxidizer and nebulized analyte enters the *preheated region*, its temperature is increased by radiation and conduction from the *blue cone* (primary reduction zone). The combustion process reaches up to the outer cone. In this region of the flame, the majority of elements from the entering analyte tends to form hydroxides or oxides. Molecules, which are not decomposed into atoms, when exposed to high temperatures during the combustion, emit significantly broader spectra in comparison to single atoms. This fact has to be taken into consideration, when analysing the measured signal. This means, that the broader emission lines of the molecules have to be subtracted from the sharper ones of the atoms. In order to bypass this problem, the flame is operated with an excess of fuel, which leads to an incomplete combustion and a surplus of carbon. This carbon helps to reduce some metal hydroxides and oxides. In contrast, if the flame is operated with an excess of oxidizer, higher temperatures can be achieved. In conclusion, the ratio between fuel and oxidant mainly depends on the elements in the given sample [10].

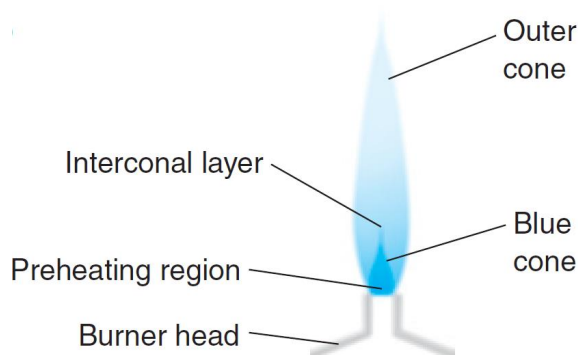


**Figure 3.7:** Cross Section of the Flame, adapted from [10]

### 3.2.3 Atomization with the Help of Furnaces

The distinguishing feature of a furnace, in comparison to the previously explained flame, is an increased sensitivity and therefore a smaller amount of analyte is required. The main part of such an electrically heated furnace is for instance a graphite tube, where a small amount of sample ( $1\text{-}100\mu\text{L}$ ) gets injected through a hole in the middle as shown in Figure 3.8 [10].



**Figure 3.8:** Graphite Tubes for Furnaces [10]

The tubes are open at both ends, so that photons from the hollow cathode lamp can pass through. In order to avoid any oxidation of the graphite, the atmosphere inside the furnace usually consists of an inert gas such as argon and the temperatures should not exceed  $2550^{\circ}\text{C}$  for a time period of less than  $7\text{s}$ . In addition, the graphite tubes often get a thin coating of pyrolytic carbon to diminish the surface porosity.

Compared to a flame or inductively coupled plasma spectrometer, the furnace increases its temperature step-wise during the whole process, which is necessary to achieve an adequate atomization of the analyte. This might be the case, when elements from i.e. organic matter like proteins are examined. Hence, the furnace gets heated in three steps.

In the first stage, the sample gets dried for around  $20\text{s}$  at a temperature of  $125^{\circ}\text{C}$ . In the following step, the furnace is heated up to  $1400^{\circ}\text{C}$  in a period of roughly one minute, in order to break up the organic matter, which is called *pyrolysis*. Finally, the process of *atomization* is achieved at a temperature of  $2100^{\circ}\text{C}$  within  $10\text{s}$ . After completing these three steps, the furnace gets heated up to  $2500^{\circ}\text{C}$  with the purpose of removing any remaining sample.

In the first two steps, the furnace is cleansed with the help of inert gas, such as argon or nitrogen, to get rid of any remnant gaseous elements from the analyte. This gas flow is solely halted during the atomization phase, in order to bypass the danger of blowing out any sample.

It is important to emphasize, that the observed signal changes after each step. In other words, this means, that the signal from the atomization process is different from the one of the pyrolysis- or drying process. Hence, the operator itself has to determine, which

signal is from the sample.

An improved version of the previously described graphite tube is the transversely heated furnace, shown in Figure 3.9. The analyte is inserted onto a platform through a sample port. The furnace wall, that surrounds the platform, gets heated up electrically with heating rates of up to  $2000\text{K/s}$  and therefore transfers the heat to the sample via radiation. Consequently, the temperature of the analyte is lagging behind that of the furnace wall, until they reach a constant temperature. Thus, any possible evaporation of the analyte is avoided during the heating process.

In comparison to the previously described graphite tube furnace, with the heat source at both ends (end-to-end-heating), the transversely heated furnace is capable of providing an almost consistent temperature distribution over the whole length of the platform. Since the centre of the furnace has a slightly higher temperature than the ends of the platform, evaporated analyte condenses at the ends. This leads to the so-called *memory – effect*, where atoms of the sample from the previous run may cause an interference with the new analyte. To bypass this issue, the relatively porous graphite tube or platform are coated with a sealing layer of pyrolytic carbon, in order to reduce the chance of any unwanted absorption of atoms from the sample [10].

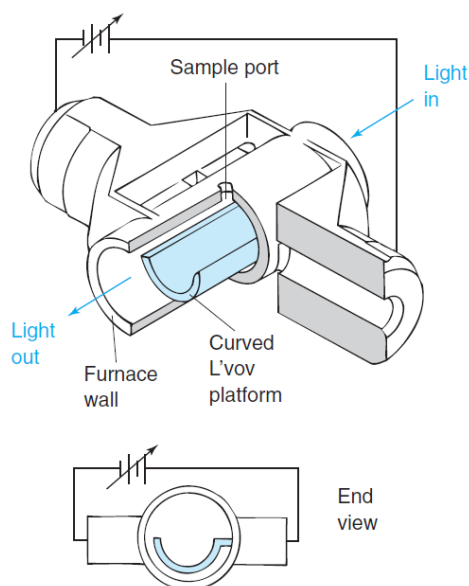


**Figure 3.9:** Sectional View of a Transversely Heated Graphite Furnace, adapted from [10]

# Chapter 4

## Experimental Setup

### 4.1 Small Scale EAF as the Experimental Setup

The experiments required for this thesis were conducted on a simplified small scale DC-powered electric arc furnace, that was designed and manufactured by [20] and later improved by [8]. A schematic overview of the recent version with the dimensions (in *mm*) is illustrated in Figure 4.1.

This laboratory version of an EAF utilizes a DC-power supplying unit, which was usually intended for plasma cutting operations. The transformer of this unit is capable of delivering a maximum power of approximately  $8kW$  (voltages of up to  $110V$  and currents of up to  $70A$ ) [13].

#### 4.1.1 Bottom Part of the Furnace

The bottom part, which is similar to the containment of a full-sized EAF, is basically fabricated from welded steel and has a cylindrical shape. On the inside of this steel containment, refractory is used, with the aim of providing a sufficient insulation from the high temperatures and to hold the copper pipes for the cooling water in place. This ring shaped refractory surrounds the anode, as well as the crucible and a part of the electrode. Since the crucible may get consumed partly during the melting process, a steel plate is placed between this crucible and the anode, to avoid any damage of the anode. This replaceable crucible, which is usually charged with scrap or ore is manufactured from non-alloyed steel. The chemical composition is shown in Table 4.1, and has to be taken into account, if parts of the crucible get molten during the experiment.

An important aspect of this furnace's design is an appropriate gas-proof sealing between the top and bottom part, which is done with two o-ring sealings. This aspect is inevitable, since it helps to prevent any gasses from escaping the oven. In addition to this, besides these sealings, there is also some electrical insulation required between the roof part (i.e.

the cathode) and the vessel (i.e. the anode), see Figure 4.1, 8.

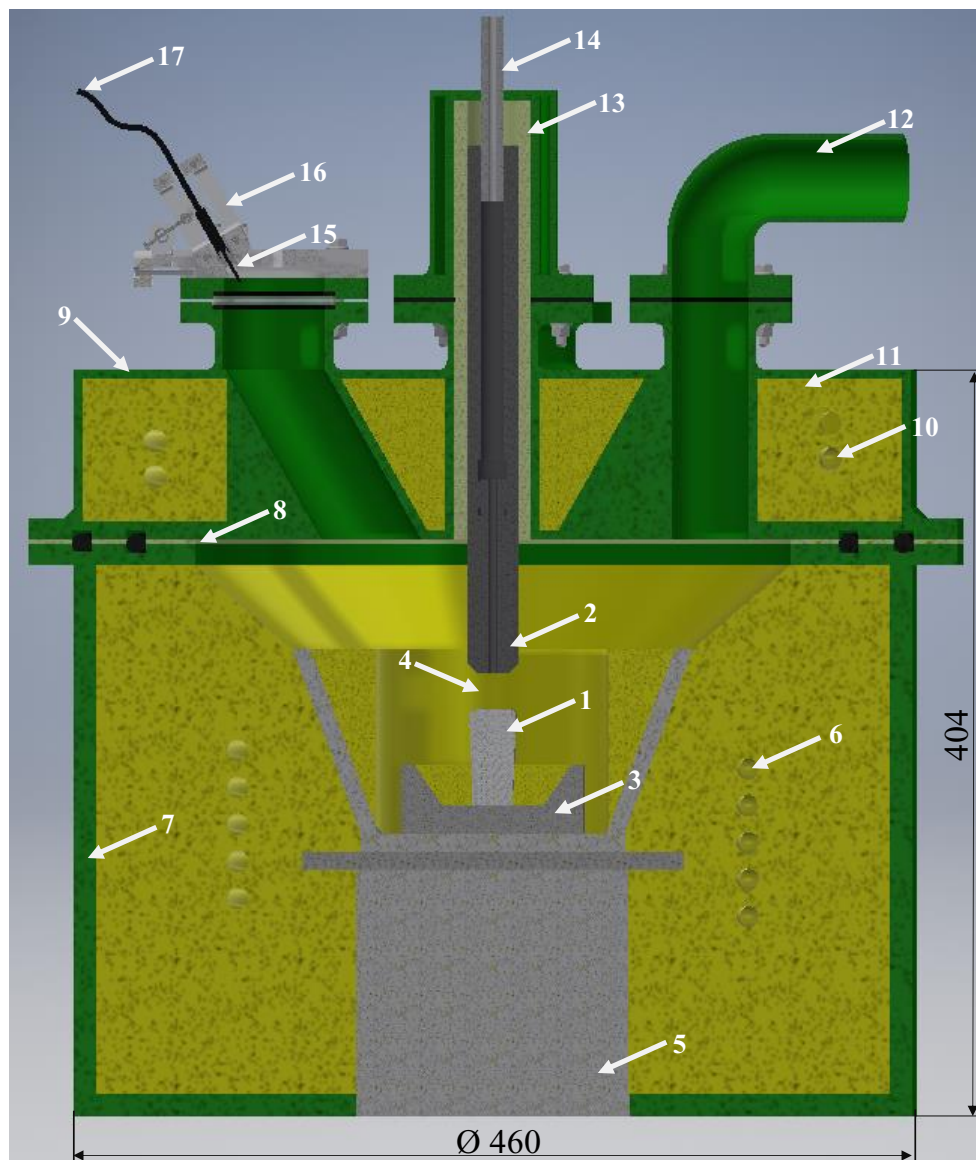


**Figure 4.1:** Cross Section of the Laboratory-EAF

- |                                  |                              |                   |
|----------------------------------|------------------------------|-------------------|
| 1...Steel Sample                 | 2...Graphite Electrode       | 3...Crucible      |
| 4...Arc                          | 5...Bottom Electrode (Anode) | 6...Cooling Pipes |
| 7...Vessel                       | 8...Electrical Insulation    | 9...Roof Part     |
| 10...Cooling Pipes (Roof Part)   | 11...Refractory              | 12...Exhaust      |
| 13...Insulation (Electrode)      | 14...Electrode (Cathode)     | 15...Fibre        |
| 16...Adjusting Mechanism (Fibre) | 17...Fibre To Spectroscope   |                   |

Fe	C	Si	Mn	P	S
99.47	0.0455	0.0182	0.354	0.0119	0.0170

**Table 4.1:** Constituents of the Crucible, [13]

### 4.1.2 Roof Part of the Furnace

Like the bottom part, this one is also manufactured from cylindrically shaped steel. In order to charge the furnace or to perform maintenance work, the roof is fully detachable with the help of a small crane.

An appropriate insulation is achieved, with the aid of refractory material and sufficient cooling is provided by copper pipes. On the top section of the roof, five flanges with sealings are attached. The one in the middle is necessary to insert the graphite electrode and its lifting mechanism for height adjustment. What is more, one of the outer four flanges is equipped with a glass window, with the purpose of getting a direct view on the arc and the molten steel. The other three ones have been installed to insert a thermocouple and therefore measure the temperature of the inside, to guide the exhaust gasses out of the furnace and to give the option of inserting materials, that are required for the process, i.e. oxides. In addition to this, the exhaust is equipped with a filter to absorb fine particles and a heating system, so that the gaseous water in the off-gas does not condense [8].

### 4.1.3 The Electrode and the Electrode Lifting Mechanism

The electrode of this small scale EAF, which is located in the centre of the roof, acts as the cathode and consists of two parts. The upper one is manufactured from graphite and the tip can either be made from tungsten or graphite as well. The main advantages of dividing the hollow electrode into two sections, that are connected to each other over a threaded joint, is to keep the tip (which gets consumed) easy to exchange or to use other materials. The electrode is hollow in the middle, in order to purge the furnace with gasses such as argon or hydrogen.

The height of the electrode (i.e. the distance between the tip and the steel sample) is adjusted with a lifting mechanism, that consists of a DC-motor and a spindle. The electrode is guided within a pipe made from PTFE, that also acts as an electrical insulator.

### 4.1.4 Spectrometer and Optical Fibre

The spectrometer used in the required experiments was the *AvaSpec ULS3648 High Resolution Fibre Optic Spectrometer* from AVANTES. Some important properties are shown



in Table 4.2 [14]. The optical fibre was from *Ocean Optics*, has a diameter of  $600\mu m$  and the optimal wavelength lies in the range of  $200-1100nm$  [21].

<b>Technical Data</b>	
Focal Length	$75mm$
Wavelength Range	$200-1000nm$
Detector	CCD array (3648 <i>pixels</i> )
Signal/Noise Ratio	350:1
AD-Converter	16-Bit, $1MHz$
Integration Time	$10\mu s-10mins$
Interface	USB 2.0

**Table 4.2:** Technical Data of the Used Spectrometer, taken from [14]

#### 4.1.5 Adjusting Mechanism for the Optical Fibre

As shown in Figure 4.1, a mechanism to adjust the angle and the position of the optical fibre and to provide a steady mounting is attached to the top of a flange. The main objective is to position the fibre properly, which means to get a direct sight onto the arc between the steel sample and the electrode.

The overall mechanism was designed with the help of a CAD-software and later 3D-printed with PLA. To give a better understanding, the cross section and the mounting position are illustrated in Figure 4.1 and the isometric view is depicted in Figure 4.2.

The horizontal position of the fibre is adjusted via screw 1, while its vertical angle can be adapted with the aid of screw 2. Figure 4.3 shows the mounting position on the furnace's roof and Figure 4.4 gives an overview of the fibre holder's parts.

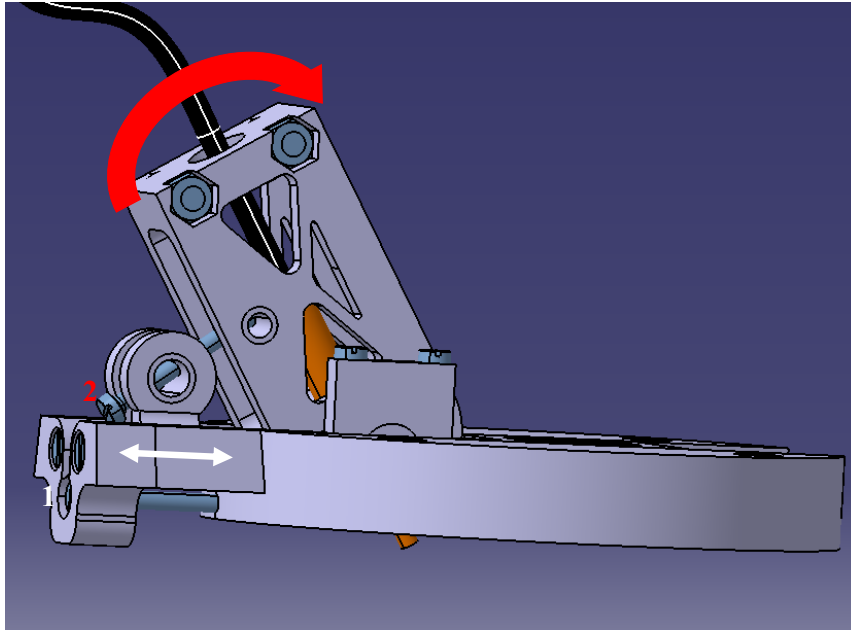


**Figure 4.2:** Isometric View of the Fibre Holder. *Screw 1* adjusts the horizontal position and *screw 2* the angle



**Figure 4.3:** Fibre Holder Mounted on a Flange on Top of the Furnace Roof

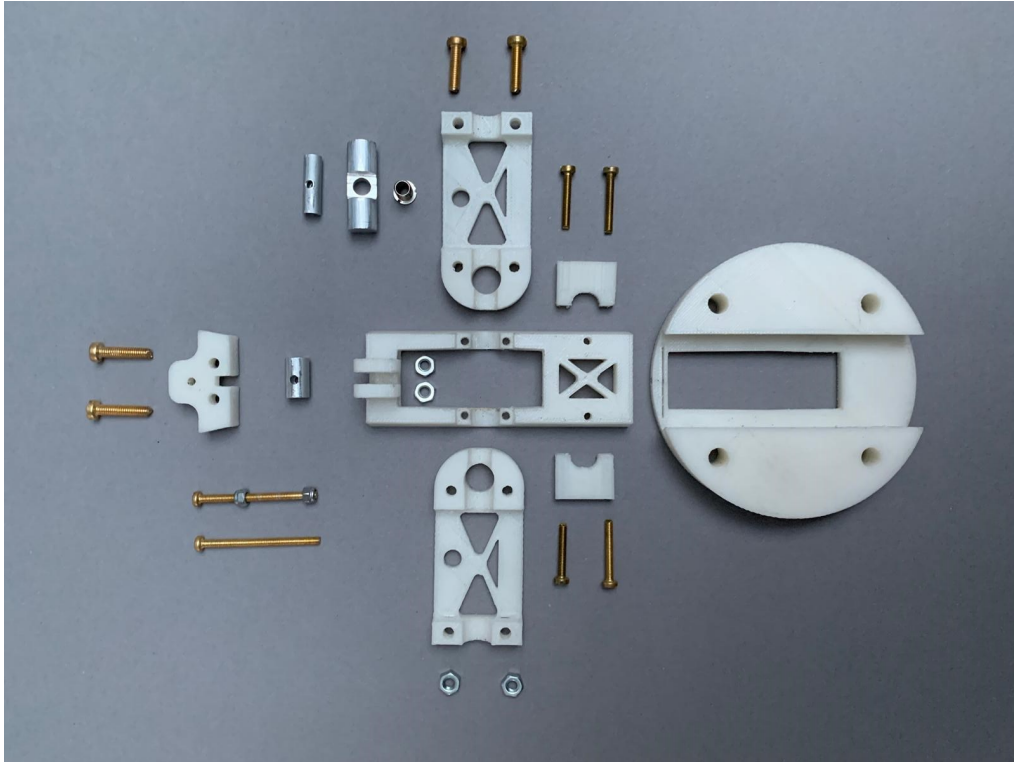


**Figure 4.4:** Overview of the Fibre Holder's Parts. The white ones are printed from PLA

# Chapter 5

## Data Processing

### 5.1 Savitzky-Golay Polynomial Smoothing

In the paper [22], that was published in 1964, Abraham Savitzky and Marcel J. E. Golay presented a method of smoothing noisy data by performing a local least-squares-fit [23]. In order to obtain a smoothed signal, Savitzky and Golay fitted a low order geometric polynomial to the noisy data observed by a spectrometer [24]. The main objective of their approach was to reduce the amount of noise in the observed signal while preserving both the height and shape of the spectral peaks [23].

Given a set of data with a finite length  $n$  (i.e. noisy spectrometer data), that can be presented as [25]:

$$\mathbf{y} = [y_1, \dots, y_n]^T \quad (5.1)$$

$$\mathbf{x} = [x_1, \dots, x_n]^T, \quad (5.2)$$

where the vector  $\mathbf{x}$  (containing equally-spaced values) defines the location of the values in  $\mathbf{y}$ . Thus, the corresponding elements  $x_i$  and  $y_i$  are forming so-called point pairs [25]:

$$\mathbf{p}_i = [x_i, y_i]. \quad (5.3)$$

In order to perform a local polynomial approximation, Savitzky-Golay-filters are designed to successively take out a subset of data (with the length or *support length*  $l_s$ ) from  $\mathbf{y}$  and optimally fit a polynomial of order  $d$  ( $d \leq l_s$ ) with the help of a least-squares-fit [26].

Considering the fact, that the support length  $l_s$  is an odd number, the half-length  $l_h$ , or *half-width* (as called in [23]) may be written as [11]:

$$l_h = \frac{l_s - 1}{2} \quad (5.4)$$

To give a better understanding, how such a filtering is achieved, an example is given with a support length  $l_s = 7$  and a fitting polynomial of order  $d = 3$ .

To begin, a vector  $\mathbf{y}$  containing a portion of noisy signal samples, whose length is equal to  $l_s$ , is set up. In general, this vector looks like that [11]:

$$\mathbf{y} = [y_{-l_h}, y_{-l_h+1}, \dots, y_0, \dots, y_{l_h-1}, y_{l_h}]^T \quad (5.5)$$

The corresponding vector  $\mathbf{x}_m$  containing the local x-values is given by [11]:

$$\mathbf{x}_m = [-l_h, \dots, 0, \dots, l_h]^T \quad (5.6)$$

In the case of the demonstration,  $\mathbf{y}$  and  $\mathbf{x}_m$  are given by:

$$\mathbf{y} = [y_{-3}, y_{-2}, y_{-1}, y_0, y_1, y_2, y_3]^T \quad (5.7)$$

$$\mathbf{x}_m = [-3, -2, -1, 0, 1, 2, 3]^T \quad (5.8)$$

Note that the subscripts of the entries in the vectors imply, that the data points are distributed symmetrically around their origin. Thus, the support length has to be an odd number. A visualization of the data points together with the fitting polynomials (constant, linear, quadratic and cubic) is depicted in Figure 5.1 [11].

Subsequently, the fitting polynomials are represented as geometric polynomials, i.e. a sum of monivariate monomials, each with a certain degree  $d$ . In general, they can be presented as [25]:

$$\hat{y}(x_m) = a_d x_m^d + \dots + a_3 x_m^3 + a_2 x_m^2 + a_1 x_m + a_0, \quad (5.9)$$

or in a more compact form [25]:

$$\hat{y}(x) = \sum_{i=0}^n a_i x^i. \quad (5.10)$$

In the case of the demonstration, the smoothing polynomials look like this [11]:

$$\text{Constant : } \hat{y} = a_0 \quad (5.11)$$

$$\text{Linear : } \hat{y} = a_1 x + a_0 \quad (5.12)$$

$$\text{Quadratic : } \hat{y} = a_2 x^2 + a_1 x + a_0 \quad (5.13)$$

$$\text{Cubic : } \hat{y} = a_3 x^3 + a_2 x^2 + a_1 x + a_0 \quad (5.14)$$

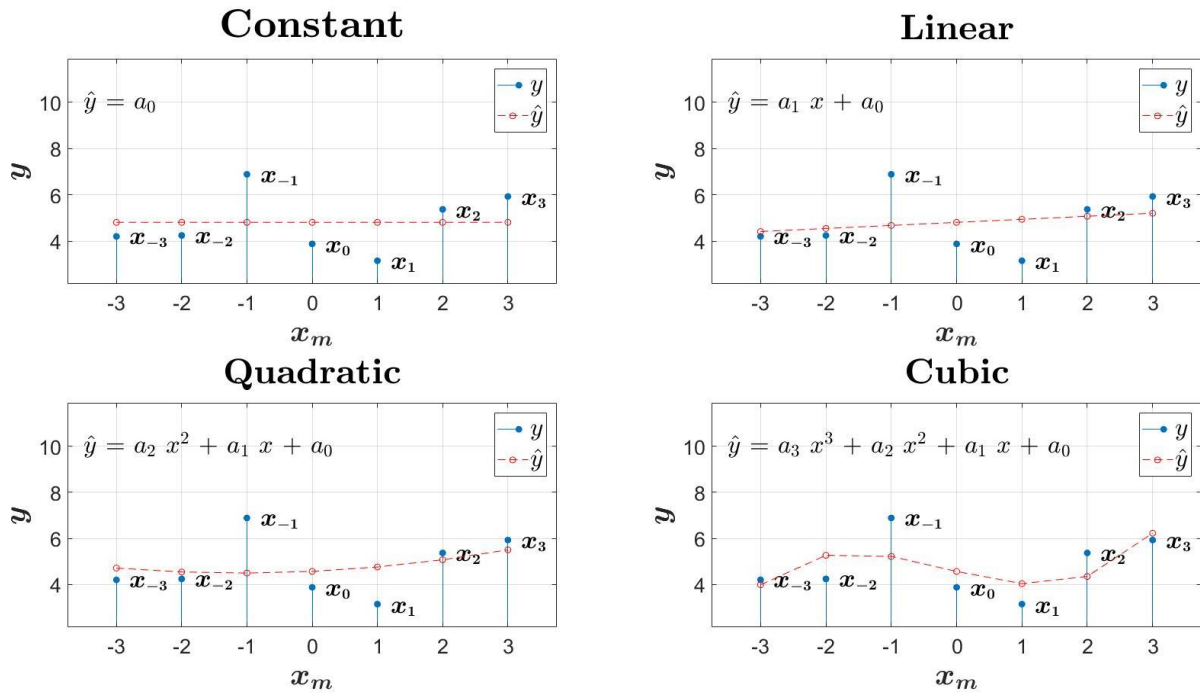


**Figure 5.1:** Data Points and the Corresponding Fitting Polynomials

It is important to point out, that the hat, as it is used in  $\hat{y}$ , denotes that these equations are utilized to perform an approximation to  $y$  (i.e. in the least-squares-sense). Hence, they are known as model- or design-equations. The vector containing the residual errors (or fitting errors) is given by [25] [11]:

$$\mathbf{r} = \mathbf{y} - \hat{\mathbf{y}} \tag{5.15}$$

$$= \begin{bmatrix} y_{-l_h} \\ y_{-l_h+1} \\ \vdots \\ y_0 \\ \vdots \\ y_{l_h-1} \\ y_{l_h} \end{bmatrix} - \begin{bmatrix} \hat{y}_{-l_h} \\ \hat{y}_{-l_h+1} \\ \vdots \\ \hat{y}_0 \\ \vdots \\ \hat{y}_{l_h-1} \\ \hat{y}_{l_h} \end{bmatrix} \tag{5.16}$$

Next, to get the fitting polynomials (equation 5.11 - 5.14) in a more compact form, the corresponding polynomial basis-vectors are represented as follows:

$$\mathbf{v}_0 = [(-l_h)^0, (-l_h + 1)^0, \dots, 0^0, \dots, (l_h - 1)^0, (l_h)^0]^T \quad (5.17)$$

$$\mathbf{v}_1 = [(-l_h)^1, (-l_h + 1)^1, \dots, 0^1, \dots, (l_h - 1)^1, (l_h)^1]^T \quad (5.18)$$

$$\mathbf{v}_2 = [(-l_h)^2, (-l_h + 1)^2, \dots, 0^2, \dots, (l_h - 1)^2, (l_h)^2]^T \quad (5.19)$$

$$\mathbf{v}_3 = [(-l_h)^3, (-l_h + 1)^3, \dots, 0^3, \dots, (l_h - 1)^3, (l_h)^3]^T \quad (5.20)$$

which yields to the following in the demonstrated example:

$$\mathbf{v}_0 = \begin{bmatrix} 1 \\ 1 \\ 1 \\ 1 \\ 1 \\ 1 \\ 1 \\ 1 \\ 1 \end{bmatrix}, \quad \mathbf{v}_1 = \begin{bmatrix} -3 \\ -2 \\ -1 \\ 0 \\ 1 \\ 2 \\ 3 \end{bmatrix}, \quad \mathbf{v}_2 = \begin{bmatrix} 9 \\ 4 \\ 1 \\ 0 \\ 1 \\ 4 \\ 9 \end{bmatrix}, \quad \mathbf{v}_3 = \begin{bmatrix} -27 \\ -8 \\ -1 \\ 0 \\ 1 \\ 8 \\ 27 \end{bmatrix} \quad (5.21)$$

Furthermore, this set of vectors can be represented in form of a matrix, which yields to the *Vandermonde – matrix* [25] [11]:

$$\mathbf{V}(x) = \begin{bmatrix} -27 & 9 & -3 & 1 \\ -8 & 4 & -2 & 1 \\ -1 & 1 & -1 & 1 \\ 0 & 0 & 0 & 1 \\ 1 & 1 & 1 & 1 \\ 8 & 4 & 2 & 1 \\ 27 & 9 & 3 & 1 \end{bmatrix} \quad (5.22)$$

$$= [\mathbf{v}_3, \mathbf{v}_2, \mathbf{v}_1, \mathbf{v}_0] \quad (5.23)$$

The matrix  $\mathbf{V}$  has the dimensions  $l_s \times (d + 1)$ , where  $l_s$  represents the support length and  $d$  the highest degree of the fitting polynomial.

One major advantage of the Vandermonde matrix is to provide a convenient evaluation of a polynomial with the following vector-matrix equation [25]:

$$\hat{\mathbf{y}} = \mathbf{V}\mathbf{a}, \quad (5.24)$$

where  $\mathbf{a}$  represents the coefficient vector

$$\mathbf{a} = [a_d, a_{d-1}, \dots, a_0]^T. \quad (5.25)$$

With the help of equation 5.24, the residual  $\mathbf{r}$ , that was presented in equation 5.15, can be formulated as [25]:

$$\mathbf{r} = \mathbf{y} - \hat{\mathbf{y}} \quad (5.26)$$

$$= \mathbf{y} - \mathbf{V}\mathbf{a}. \quad (5.27)$$

The initial desire was to fit a polynomial  $\hat{\mathbf{y}}$  to the set of given data  $\mathbf{y}$ , which might be accomplished in the least-squares-sense. With the assistance of this approach, the coefficients in  $\mathbf{a}$  are determined by minimizing the fitting error  $\mathbf{r}$ , which yields to the cost function [25] [11] :

$$\varepsilon(\mathbf{a}) = \sum_{i=1}^n r_i^2. \quad (5.28)$$

The cost function is basically the sum of the squared residuals and therefore a scalar function of the coefficient vector  $\mathbf{a}$  [25].

Expressing equation 5.28 with vectors leads to [25]:

$$\varepsilon(\mathbf{a}) = \|\mathbf{r}\|_2^2 \quad (5.29)$$

$$= \mathbf{r}^T \mathbf{r} \quad (5.30)$$

$$= (\mathbf{y} - \mathbf{V}\mathbf{a})^T (\mathbf{y} - \mathbf{V}\mathbf{a}). \quad (5.31)$$

Next, the transpose is applied and the equation gets expanded:

$$\varepsilon(\mathbf{a}) = (\mathbf{y}^T - \mathbf{a}^T \mathbf{V}^T) (\mathbf{y} - \mathbf{V}\mathbf{a}) \quad (5.32)$$

$$= \mathbf{y}^T \mathbf{y} - \mathbf{y}^T \mathbf{V}\mathbf{a} - \mathbf{a}^T \mathbf{V}^T \mathbf{y} + \mathbf{a}^T \mathbf{V}^T \mathbf{V}\mathbf{a}. \quad (5.33)$$

A further simplification of the two terms in the middle can be done, since  $\varepsilon(\mathbf{a})$  is a scalar function and therefore  $\mathbf{y}^T \mathbf{V}\mathbf{a}$  and  $\mathbf{a}^T \mathbf{V}^T \mathbf{y}$  are also scalars. Hence,  $\mathbf{y}^T \mathbf{V}\mathbf{a}$  can be transposed, which results in the following expression of the cost function [25]:

$$\varepsilon(\mathbf{a}) = \mathbf{y}^T \mathbf{y} - 2\mathbf{a}^T \mathbf{V}^T \mathbf{y} + \mathbf{a}^T \mathbf{V}^T \mathbf{V}\mathbf{a}. \quad (5.34)$$

The minimization is achieved by computing the first derivative of the cost function with



respect to  $\mathbf{a}$  and setting it equal to zero [25]:

$$\frac{\partial \varepsilon(\mathbf{a})}{\partial \mathbf{a}} = 0 \quad (5.35)$$

$$0 = -2\mathbf{V}^T \mathbf{y} + 2\mathbf{V}^T \mathbf{V} \mathbf{a}. \quad (5.36)$$

Dividing by two and getting the term  $\mathbf{V}^T \mathbf{y}$  to the other side, results in a set of linear equations [25]:

$$\mathbf{V}^T \mathbf{V} \mathbf{a} = \mathbf{V}^T \mathbf{y}, \quad (5.37)$$

which are also known as *normal – equations* [25].

Therefore, the optimal solution is given by [11]:

$$\mathbf{a} = (\mathbf{V}^T \mathbf{V})^{-1} \mathbf{V}^T \mathbf{y} \quad (5.38)$$

$$= \mathbf{G}^T \mathbf{y}. \quad (5.39)$$

Whereby the matrix  $\mathbf{G}$ , with the dimensions  $l_s \times (d + 1)$ , is denoted as [11]:

$$\mathbf{G} = \mathbf{V}(\mathbf{V}^T \mathbf{V})^{-1} \quad (5.40)$$

In the case of the shown example here,  $\mathbf{G}$  has the dimensions  $7 \times 4$ , since  $l_s = 7$  and  $d = 3$ . By inserting equation 5.39 into 5.24, the smoothed values can be obtained [11]:

$$\hat{\mathbf{y}} = \mathbf{V} \mathbf{a} \quad (5.41)$$

$$= \mathbf{V} \mathbf{G}^T \mathbf{y} \quad (5.42)$$

$$= \mathbf{V}(\mathbf{V}^T \mathbf{V})^{-1} \mathbf{V}^T \mathbf{y} \quad (5.43)$$

$$= \mathbf{B} \mathbf{y} \quad (5.44)$$

Whereby the matrix  $\mathbf{B}$  has the dimensions  $l_s \times l_s$  and is computed as follows [11]:

$$\mathbf{B} = \mathbf{V} \mathbf{G}^T \quad (5.45)$$

$$= \mathbf{G} \mathbf{V}^T \quad (5.46)$$

$$= \mathbf{V}(\mathbf{V}^T \mathbf{V})^{-1} \mathbf{V}^T \quad (5.47)$$

$$(5.48)$$

In the shown example,  $\mathbf{G}$  is given by:

$$\mathbf{G} = \mathbf{V}(\mathbf{V}^T \mathbf{V})^{-1} \tag{5.49}$$

$$= \begin{bmatrix} -27 & 9 & -3 & 1 \\ -8 & 4 & -2 & 1 \\ -1 & 1 & -1 & 1 \\ 0 & 0 & 0 & 1 \\ 1 & 1 & 1 & 1 \\ 8 & 4 & 2 & 1 \\ 27 & 9 & 3 & 1 \end{bmatrix} \left( \begin{bmatrix} -27 & -8 & -1 & 0 & 1 & 8 & 27 \\ 9 & 4 & 1 & 0 & 1 & 4 & 9 \\ -3 & -2 & -1 & 0 & 1 & 2 & 3 \\ 1 & 1 & 1 & 1 & 1 & 1 & 1 \end{bmatrix} \begin{bmatrix} -27 & 9 & -3 & 1 \\ -8 & 4 & -2 & 1 \\ -1 & 1 & -1 & 1 \\ 0 & 0 & 0 & 1 \\ 1 & 1 & 1 & 1 \\ 8 & 4 & 2 & 1 \\ 27 & 9 & 3 & 1 \end{bmatrix} \right)^{-1} \tag{5.50}$$

$$= \begin{bmatrix} -27 & 9 & -3 & 1 \\ -8 & 4 & -2 & 1 \\ -1 & 1 & -1 & 1 \\ 0 & 0 & 0 & 1 \\ 1 & 1 & 1 & 1 \\ 8 & 4 & 2 & 1 \\ 27 & 9 & 3 & 1 \end{bmatrix} \begin{bmatrix} 1588 & 0 & 196 & 0 \\ 0 & 196 & 0 & 28 \\ 196 & 0 & 28 & 0 \\ 0 & 28 & 0 & 7 \end{bmatrix}^{-1} \tag{5.51}$$

$$= \begin{bmatrix} -27 & 9 & -3 & 1 \\ -8 & 4 & -2 & 1 \\ -1 & 1 & -1 & 1 \\ 0 & 0 & 0 & 1 \\ 1 & 1 & 1 & 1 \\ 8 & 4 & 2 & 1 \\ 27 & 9 & 3 & 1 \end{bmatrix} \begin{bmatrix} \frac{1}{216} & 0 & -\frac{7}{216} & 0 \\ 0 & \frac{1}{84} & 0 & -\frac{1}{21} \\ -\frac{7}{216} & 0 & \frac{397}{1512} & 0 \\ 0 & -\frac{1}{21} & 0 & \frac{1}{3} \end{bmatrix} \tag{5.52}$$

$$= \frac{1}{1512} \begin{bmatrix} -27 & 9 & -3 & 1 \\ -8 & 4 & -2 & 1 \\ -1 & 1 & -1 & 1 \\ 0 & 0 & 0 & 1 \\ 1 & 1 & 1 & 1 \\ 8 & 4 & 2 & 1 \\ 27 & 9 & 3 & 1 \end{bmatrix} \begin{bmatrix} 7 & 0 & -49 & 0 \\ 0 & 18 & 0 & -72 \\ -49 & 0 & 397 & 0 \\ 0 & -72 & 0 & 504 \end{bmatrix} \tag{5.53}$$

$$= \frac{1}{1512} \begin{bmatrix} -42 & 90 & 132 & -144 \\ 42 & 0 & -402 & 216 \\ 42 & -54 & -348 & 432 \\ 0 & -72 & 0 & 504 \\ -42 & -54 & 348 & 432 \\ -42 & 0 & 402 & 216 \\ 42 & 90 & -132 & -144 \end{bmatrix} \tag{5.54}$$

The matrix  $\mathbf{B}$  is then given as [11]:

$$\mathbf{B} = \mathbf{V}\mathbf{G}^T \quad (5.55)$$

$$= \mathbf{G}\mathbf{V}^T \quad (5.56)$$

$$= \frac{1}{1512} \begin{bmatrix} -42 & 90 & 132 & -144 \\ 42 & 0 & -402 & 216 \\ 42 & -54 & -348 & 432 \\ 0 & -72 & 0 & 504 \\ -42 & -54 & 348 & 432 \\ -42 & 0 & 402 & 216 \\ 42 & 90 & -132 & -144 \end{bmatrix} \begin{bmatrix} -27 & -8 & -1 & 0 & 1 & 8 & 27 \\ 9 & 4 & 1 & 0 & 1 & 4 & 9 \\ -3 & -2 & -1 & 0 & 1 & 2 & 3 \\ 1 & 1 & 1 & 1 & 1 & 1 & 1 \end{bmatrix} \quad (5.57)$$

$$= \frac{1}{1512} \begin{bmatrix} 1404 & 288 & -144 & -144 & 36 & 144 & -72 \\ 288 & 684 & 576 & 216 & -144 & -252 & 144 \\ -144 & 576 & 684 & 432 & 72 & -144 & 36 \\ -144 & 216 & 432 & 504 & 432 & 216 & -144 \\ 36 & -144 & 72 & 432 & 684 & 576 & -144 \\ 144 & -252 & -144 & 216 & 576 & 684 & 288 \\ -72 & 144 & 36 & -144 & -144 & 288 & 1404 \end{bmatrix} \quad (5.58)$$

Due to the fact that the columns in the matrix  $\mathbf{B}$  are the same as its rows,  $\mathbf{B}$  is symmetric. Consequently,  $\mathbf{B}$  can be expressed either row- or column-wise [11]:

$$\mathbf{B} = \left[ \mathbf{b}_{-l_h}, \mathbf{b}_{-l_h+1}, \dots, \mathbf{b}_0, \dots, \mathbf{b}_{l_h-1}, \mathbf{b}_{l_h} \right] = \begin{bmatrix} \mathbf{b}_{-l_h}^T \\ \mathbf{b}_{-l_h+1}^T \\ \vdots \\ \mathbf{b}_0^T \\ \vdots \\ \mathbf{b}_{l_h-1}^T \\ \mathbf{b}_{l_h}^T \end{bmatrix} = \mathbf{B}^T \quad (5.59)$$

$$\mathbf{B} = \left[ \mathbf{b}_{-3}, \mathbf{b}_{-2}, \mathbf{b}_{-1}, \mathbf{b}_0, \mathbf{b}_1, \mathbf{b}_2, \mathbf{b}_3 \right] = \begin{bmatrix} \mathbf{b}_{-3}^T \\ \mathbf{b}_{-2}^T \\ \mathbf{b}_{-1}^T \\ \mathbf{b}_0^T \\ \mathbf{b}_1^T \\ \mathbf{b}_2^T \\ \mathbf{b}_3^T \end{bmatrix} = \mathbf{B}^T \quad (5.60)$$

Both, the rows and the columns of  $\mathbf{B}$  represent the so-called Savitzky-Golay-smoothing filters. More precisely, since  $\mathbf{b}_0$  (the centre row or centre column of  $\mathbf{B}$ ) is used to smooth a large set of data in the steady state, it is also referred to as the *Steady-State-Savitzky Golay* filter. In contrast to that, the other rows (or columns) of  $\mathbf{B}$  are named *Transient-Savitzky Golay* filters, because they are utilized to perform the smoothing during the input-on and input-off period, respectively [11]. Figure 5.2 depicts the difference between smoothing with (using transient-, input-on- and input-off- filters) and without (solely using the transient filters) endpoint-correction.

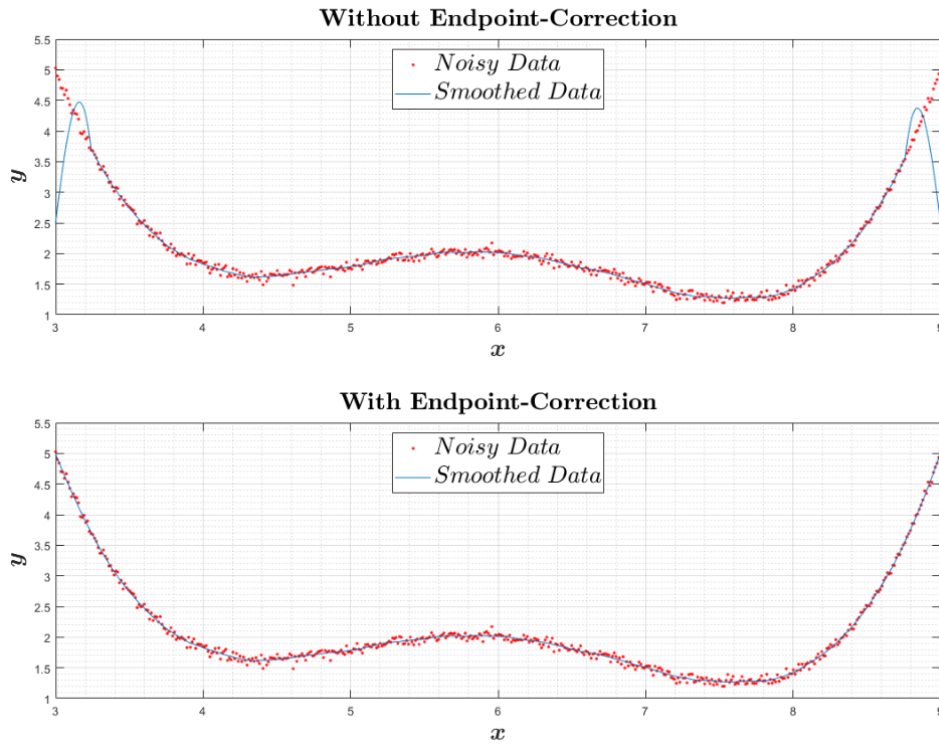


**Figure 5.2:** Difference Between Smoothing Polynomial ( $l_s = 41$ ,  $d = 2$ ) With and Without Endpoint-Correction

The smoothed data points are finally obtained by performing convolution of the noisy data set with the centre row (or column) of  $\mathbf{B}$  (in the steady-state case) [11][25].

---

**Algorithm 1:** Perform Savitzky-Golay Polynomial Smoothing
 

---

**Input:**

- Noisy data (observations):  $\mathbf{y}$
- Order of smoothing polynomial: *order*
- Supportlength:  $l_s$

**Output:**

- Vector  $\mathbf{y}_{smoothed}$ , containing smoothed data

**Algorithm:**

1. Compute the half-length:  $l_h = \frac{l_s-1}{2}$
  2. Define a column-vector containing local x-coordinates:  $\mathbf{x} = [-l_h, \dots, 0, \dots, l_h]$
  3. Set up the Vandermonde-matrix  $\mathbf{V}_b$
  4. Compute  $\mathbf{B}$  (matrix that represents the Savitzky-Golay smoothing-filters):  
 $\mathbf{B} = \mathbf{V}_b \mathbf{V}_b^+$
  5. Extract the centre row of  $\mathbf{B}$  (i.e. the *Steady – State* Savitzky-Golay filters):  
 $\mathbf{b}_c = \mathbf{B}(l_h + 1, :)$
  6. Compute the vector containing smoothed data  $\mathbf{y}_{Smoothed}$  by performing convolution:  $\mathbf{y}_{Smoothed} = conv(\mathbf{y}, \mathbf{b}_c)$
- 

### 5.1.1 Some Properties of SG-Smoothing Filters

One advantage of the SG-filters is, that the entries of matrix  $\mathbf{B}$  only depend on the support-length  $l_s$  and the order  $d$  of the fitting polynomial, and thus are independent of the observed data. In other words, the smoothing filters  $\mathbf{b}$  only have to be computed once for every combination of  $l_s$  and  $d$ , and the smoothed data  $\hat{\mathbf{y}}$  is then obtained via convolution. Another interesting property is, that SG-filters with a polynomial of order  $d = 0$  is equivalent to a moving average-filter, provided that  $l_s$  is equal in both cases. A moving average-filter may be given as [23]:

$$\hat{\mathbf{y}} = \frac{1}{l_s} \sum_{j=-l_h}^{l_h} y_j \quad (5.61)$$

One major difference between the two FIR filters mentioned above is their capability of reducing the amount of noise in the signal, which can be measured with the help of the *noise reduction ratio*, or NRR [11]:

$$NRR = \sum_n h_n^2 \quad (5.62)$$

$$= \sum_{i=-l_h}^{l_h} b_0^2(i) \quad (5.63)$$

$$= \mathbf{b}_0^T \mathbf{b}_0, \quad (5.64)$$

whereas  $h_n$  is the  $n$ -th impulse response of a filter. In other words, equation 5.63 shows, that the NRR is obtained by squaring and summing the filter coefficients, which leads to [11]:

$$NRR_{SG} = \sum_{i=-l_h}^{l_h} b_0^2(i) \quad (5.65)$$

$$= \mathbf{b}_0^T \mathbf{b}_0 \quad (5.66)$$

in the case of a SG-filter and a moving average filter in their steady-state [11]:

$$NRR_{MA} = \frac{1}{l_s} \quad (5.67)$$

In general, a noise reduction ratio smaller than one implies, that the filter achieved an attenuation of the noise in the input signal. Hence, the NRR is a convenient method of evaluating a noise reduction filter [11].

## 5.2 Background Correction and Baseline Estimation

In atomic spectroscopy, it is essential to perform a background correction on the observed signal, in order to solely remove the parts of the signal, which are not from the analyzed sample. These undesired parts of the obtained data might be from the plasma, the flame, or glowing parts of the graphite furnace [27].

### 5.2.1 Background Removal by Minimizing a Non-Quadratic Cost Function

As stated in the previous section, the data from a spectrometer can be represented by a set of data with a given length  $n$ :

$$\mathbf{y} = [y_1, \dots, y_n]^T \quad (5.68)$$

Furthermore, the vector  $\mathbf{y}$  consists of the following parts [28]:

$$\mathbf{y} = \mathbf{b} + \mathbf{e}, \quad (5.69)$$

where  $\mathbf{b}$  represents the background and gets modeled with a polynomial of order  $d$ . The vector  $\mathbf{e}$  covers the residual, which moreover contains the peaks (positive or negative), any model uncertainties and physical noise. Note that  $\mathbf{b}$  can be expressed as a vector-matrix equation [28]:

$$\mathbf{b} = \mathbf{V}\mathbf{a}, \quad (5.70)$$

where  $\mathbf{V}$  is the Vandermonde matrix and  $\mathbf{a}$  is the corresponding coefficient vector.

The main objective of this approach is to obtain  $\mathbf{a}$ , which leads to minimizing the following cost-function [28]:

$$\varepsilon(\mathbf{a}) = \sum_{i=1}^n \varphi(y_i - b_i). \quad (5.71)$$

However, a quadratic cost function, as it is used in a least-squares fit, would not lead to a satisfactory result, in general. This is explained due to the fact, that a quadratic cost function  $\varphi(x)$  would square each residual  $r_i = (y_i - b_i)$  and therefore higher values (i.e. data from peaks) get a much greater cost. Consequently, the flaw of this approach are data points, that have a sufficiently high distance from the baseline, tend to shift the polynomial (that models the baseline) towards these values [28].

With the aim of bypassing this issue, the following approach utilizes cost functions, that are solely quadratic in the close proximity to zero and therefore avoid any insufficiently high costs for larger values. The shown method for estimating the background considers

the following functions  $\varphi(x)$  [28]:

1. Symmetric Truncated Quadratic Function:

$$\varphi_{STQ}(x) = \begin{cases} x^2, & \text{if } |x| < s \\ s^2, & \text{otherwise} \end{cases} \quad \forall x \in \mathbb{R} \quad (5.72)$$

$$\varphi'_{STQ}(x) = \begin{cases} 2x, & \text{if } |x| < s \\ 0, & \text{otherwise} \end{cases} \quad \forall x \in \mathbb{R} \quad (5.73)$$

2. Asymmetric Truncated Quadratic Function:

$$\varphi_{ATQ}(x) = \begin{cases} x^2, & \text{if } x < s \\ s^2, & \text{otherwise} \end{cases} \quad \forall x \in \mathbb{R} \quad (5.74)$$

$$\varphi'_{ATQ}(x) = \begin{cases} 2x, & \text{if } x < s \\ 0, & \text{otherwise} \end{cases} \quad \forall x \in \mathbb{R} \quad (5.75)$$

3. Symmetric Huber Function:

$$\varphi_{SH}(x) = \begin{cases} x^2, & \text{if } |x| < s \\ 2s|x| - s^2, & \text{otherwise} \end{cases} \quad \forall x \in \mathbb{R} \quad (5.76)$$

$$\varphi'_{SH}(x) = \begin{cases} -2s, & \text{if } x \leq -s \\ 2x, & \text{if } |x| < s \\ 2s, & \text{if } x \geq s \end{cases} \quad \forall x \in \mathbb{R} \quad (5.77)$$

4. Asymmetric Huber Function:

$$\varphi_{ASH}(x) = \begin{cases} x^2, & \text{if } x < s \\ 2sx - s^2, & \text{otherwise} \end{cases} \quad \forall x \in \mathbb{R} \quad (5.78)$$

$$\varphi'_{ASH}(x) = \begin{cases} 2x, & \text{if } x < s \\ 2s, & \text{otherwise} \end{cases} \quad \forall x \in \mathbb{R} \quad (5.79)$$

For the sake of a better understanding, the functions are illustrated in Figure 5.3.

The main difference between a quadratic function  $\varphi(x) = x^2$  (as used in an ordinary least squares fit) and the proposed ones is, that the (a)symmetric Huber and (a)symmetric truncated quadratic functions only give a quadratic cost to values, that are beneath a certain



threshold  $s$ . Beyond  $s$ , the cost of the Huber function is increasing in a linear manner, while that of the truncated quadratic ones remain, as its name implies, constant.

Symmetric functions  $\varphi(x)$ , that are depicted in Figure 5.3 *left*, may be used for data that contains both positive and negative peak values. However, in optical spectroscopy, where only positive peaks occur, asymmetric cost functions (Figure 5.3 *right*) are taken into consideration [28].

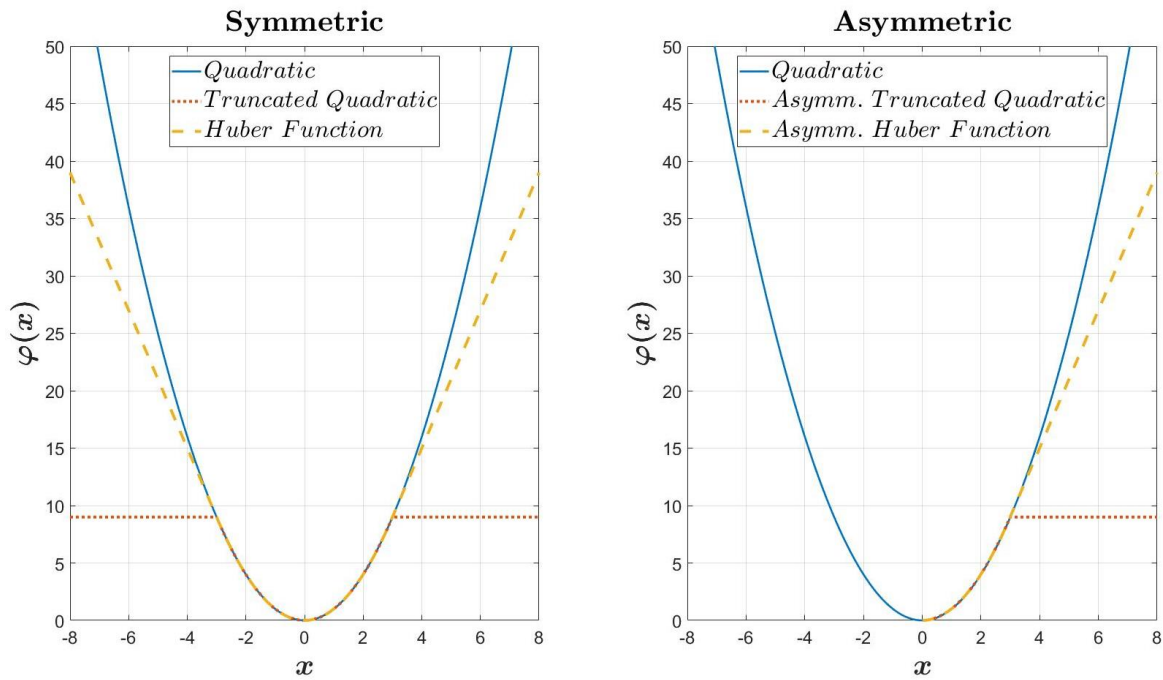


**Figure 5.3:** Comparison of Symmetric and Asymmetric Non-Quadratic Cost-Functions to the Quadratic Cost-Function. ( $s = 3$ )

In contrast to the classical least squares method, the cost function shown in this approach cannot be minimized by deriving equation 5.71 with respect to  $\mathbf{a}$  and set it equal to zero to obtain the optimal solution for  $\mathbf{a}$ . Therefore, the idea is to take the *half-quadratic (HQ) minimization* into consideration, which is basically an iterative way of optimizing a non-quadratic cost function  $\varphi(x)$  [28].

The prerequisite for applying the algorithm of the HQ-minimization as given in [29] is that  $\alpha$  lies in the following range:

$$\forall \alpha \in [0; \alpha_{max}[ \quad (5.80)$$

and for which the following function is strictly convex [28]:

$$g_{\alpha}(x) = \frac{x^2}{2} - \alpha\varphi(x). \quad (5.81)$$

In the case of the truncated quadratic and the Huber function,  $\alpha_{max}$  is given as [28]:

$$\alpha_{max} = \frac{1}{2}. \quad (5.82)$$

Next, the algorithm proposed by [30] requires the introduction of an auxiliary variable [28]

$$\mathbf{d} = [d_1, \dots, d_n]^T, \quad (5.83)$$

that yields to the augmented criterion, which provides the same minimum as  $\varepsilon(\mathbf{a})$  in equation 5.71 does [28]:

$$\mathcal{K}(\mathbf{a}, \mathbf{d}) = \frac{1}{\alpha} \sum_{k=1}^n \left( \frac{1}{2} (y_k - (\mathbf{V}\mathbf{a})_k - d_k)^2 + \zeta(d_k) \right), \quad (5.84)$$

in which  $\zeta(d_k)$  is given as [28]:

$$\zeta(d) = \sup_x \left( \varphi(x) - \frac{(x-d)^2}{2} \right) \quad (5.85)$$

It is important to emphasize that the function  $\mathcal{K}(\mathbf{a}, \mathbf{d})$  is convex in  $\mathbf{d}$  and a quadratic function of  $\mathbf{a}$ , which therefore explains the term *half quadratic criterion* [28].

The iterative algorithm shown above is aborted, if the following condition is met [28]:

$$\mathcal{K}^i - \mathcal{K}^{i-1} < c, \quad (5.86)$$

where  $c$  represents a threshold value (i.e.  $10^{-5}$ ). In this case, the convergence is reached. Minimizing the criterion  $\mathcal{K}(\mathbf{a}, \mathbf{d})$  given in equation 5.84 with respect to the coefficient vector  $\mathbf{a}$  while keeping  $\mathbf{d}$  fixed leads to [28]:

$$\hat{\mathbf{a}} = (\mathbf{V}^T \mathbf{V})^{-1} \mathbf{V}^T (\mathbf{y} + \mathbf{d}), \quad (5.87)$$

while the same procedure with fixed  $\mathbf{a}$  and minimizing with respect to  $\mathbf{d}$  gives [28]:

$$\hat{d}_k = b_k - y_k + \alpha \varphi'(y_k - b_k) \quad (5.88)$$

The code presented in the appendix was adapted from [28]. Figure 5.4 and 5.5 show, how this algorithm is applied to synthetic and real data.

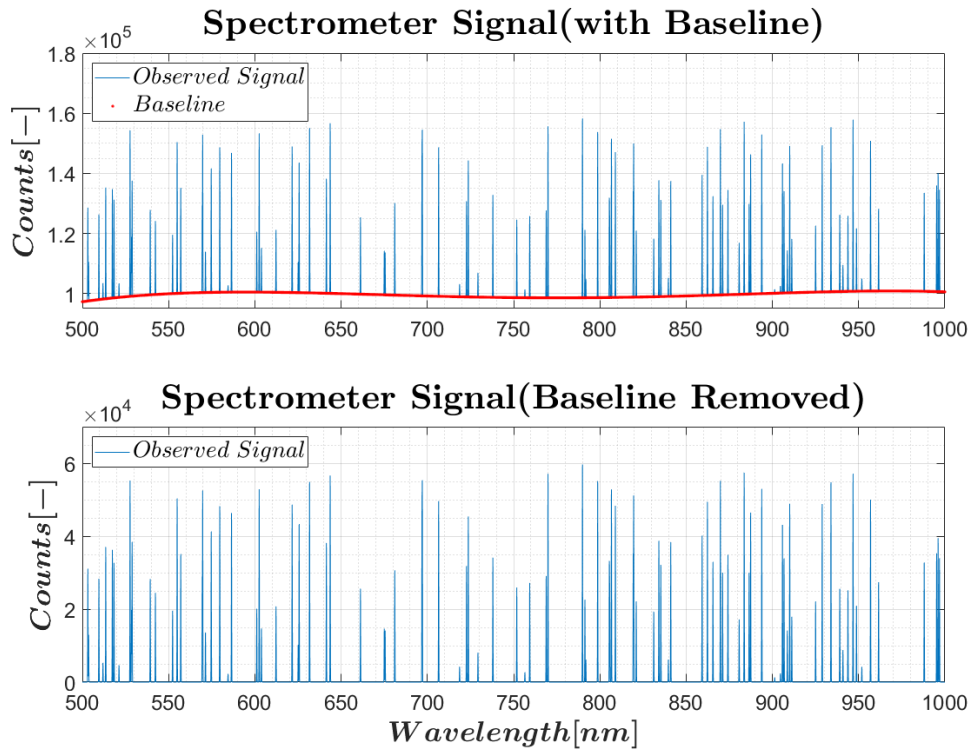


**Figure 5.4:** Baseline Removal, Demonstrated on Synthetic Spectrometer Data. Baseline modelled as a polynomial of order  $d = 4$

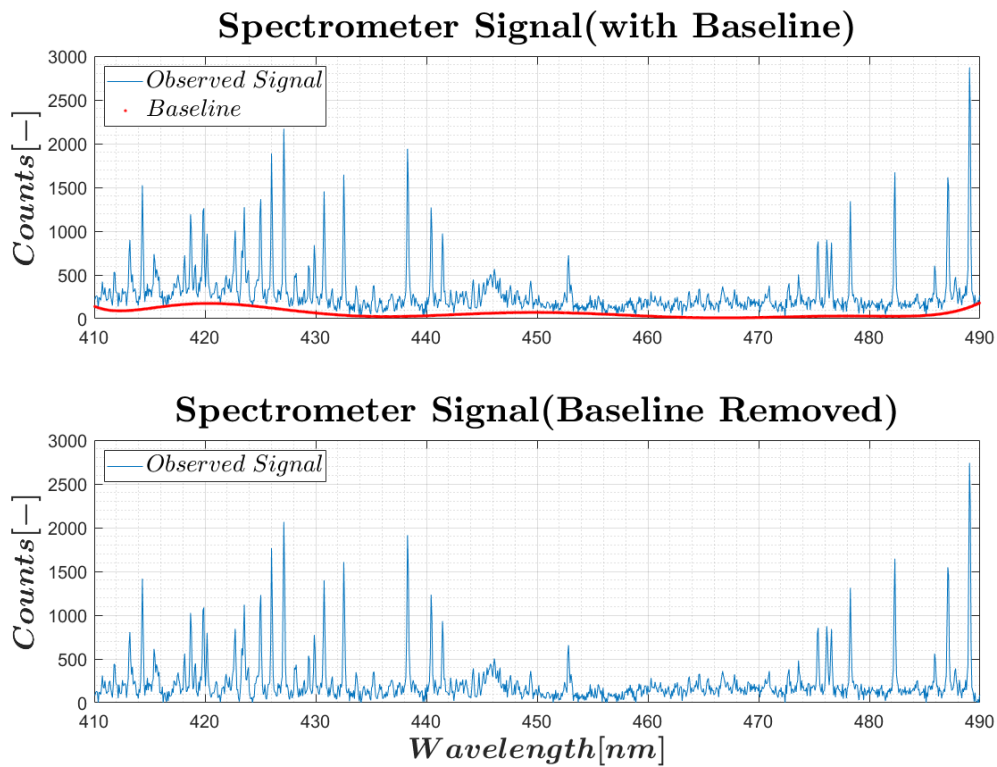


**Figure 5.5:** Baseline Removal, Demonstrated on Real Spectrometer Data

---

**Algorithm 2:** Background Removal by Minimizing a Non-Quadratic Cost-Function
 

---

**Input:**

- Vector of locations  $\mathbf{x}$
- Vector of observations  $\mathbf{y}$
- Order of the polynomial modelling the baseline
- Threshold value  $s$
- Type of the cost function

**Output:**

- Model of the baseline  $\mathbf{y}_{BL}$

**Algorithm:**

1. Perform a coordinate transformation, to get a better conditioned Vandermonde-matrix:  $\mathbf{z} = \frac{\mathbf{x} - \bar{x}}{\sigma_x}$
  2. Set up the Vandermonde-matrix  $\mathbf{V}$  and perform QR-decomposition:  $[\mathbf{Q}, \mathbf{R}] = qr(\mathbf{V}, 0)$
  3. Perform an initial estimation of the baseline:
    - (a) Initialize the coefficient vector  $\mathbf{a}$ :  $\mathbf{a} = \mathbf{R}^+ \mathbf{Q}^T \mathbf{y}$
    - (b) Model for the baseline:  $\mathbf{y}_{BL} = \mathbf{V} \mathbf{a}$
  4. Perform an iteration, that ends, if:
    - The maximum number of iterations is reached
    - The termination criterion is fulfilled
    - (a) Compute the residual, i.e. the difference between the current model of the baseline and that of the previous iteration:  $\mathbf{r} = \mathbf{y}_{BL} - \mathbf{y}_{BL,prev}$ .
    - (b) Define the termination criterion: Terminate if  $\sum_{i=1}^n r_i^2 < 10^{-5}$
    - (c) Compute the difference between observations and the model  $\boldsymbol{\varepsilon} = \mathbf{y} - \mathbf{y}_{BL}$
    - (d) Compute  $\mathbf{d}$  as follows:  $\mathbf{d} = -\boldsymbol{\varepsilon} + \alpha \boldsymbol{\varphi}'(\mathbf{x})$
    - (e) Get the coefficient vector of the model baseline:  $\mathbf{a} = \mathbf{R}^+ \mathbf{Q}^T (\mathbf{y} + \mathbf{d})$
    - (f) Get the model baseline  $\mathbf{y}_{BL}$ :  $\mathbf{y}_{BL} = \mathbf{V} \mathbf{a}$
  5. Put out the modelled baseline  $\mathbf{y}_{BL}$
-

## 5.2.2 Adaptive Iteratively Reweighted Penalized Least-Squares Background Correction

The penalized least-squares method was initially intended for smoothing data and published by Whittaker in the 1920's.

According to [31], the idea behind the *Penalized Least-Squares Method* dates back to 1899, where it was mentioned in Bohlmann's work [32].

Later, in the 1920's, this idea was further refined by Whittaker and Herderson, for smoothing operations, giving this method its name *Whittaker-Herderson-Smoothing* [31].

Basically, this algorithm consists of the introduction and minimization of a criterion which includes the deviation between the fitted and original data as well as the roughness of the fitted signal [33], [34].

Considering an observation  $\mathbf{y}$  with a finite length  $n$

$$\mathbf{y} = [y_1, \dots, y_n]^T, \quad (5.89)$$

and the corresponding  $x$ -vector containing equally spaced elements  $x_i$

$$\mathbf{x} = [x_1, \dots, x_n]^T, \quad (5.90)$$

the sum of the square errors (cost function) is given by [34]:

$$\varepsilon(\mathbf{a}) = \sum_{i=1}^n (y_i - \hat{y}_i)^2 \quad (5.91)$$

In addition to this, summing and squaring the differences of the fitted data results in the roughness [31] [34]:

$$R = \sum_{i=2}^n (\hat{y}_i - \hat{y}_{i-1})^2 \quad (5.92)$$

$$= \sum_{i=1}^{n-m} (\Delta^m \hat{y}_i)^2, \quad (5.93)$$

where the expression  $\Delta^m \hat{y}_i$  denotes the  $m$ -th difference between the values of the modelled data points  $\hat{y}_i$  in the following manner[31] [34]:

$$m = 1: \quad \Delta^1 \hat{y}_i = \Delta \hat{y}_i = \hat{y}_i - \hat{y}_{i-1} \quad (5.94)$$

$$m = 2: \quad \Delta^2 \hat{y}_i = \Delta(\Delta \hat{y}_i) = \hat{y}_{i+1} - 2\hat{y}_i + \hat{y}_{i-1} \quad (5.95)$$

In general, the term  $\Delta^m \hat{\mathbf{y}}$  can also be expressed with the help of matrices and vectors [31] [34]:

$$\Delta^m \hat{\mathbf{y}} = \mathbf{D}_m \hat{\mathbf{y}}, \quad (5.96)$$

whereas  $\mathbf{D}_m$  represents the  $m$ -th difference matrix with the dimensions  $(n - m) \times n$ . As an example,  $D_1$  (dimensions  $(n - 1) \times n$ ) is illustrated below [31] [34]:

$$\mathbf{D}_1 = \begin{bmatrix} -1 & 1 & 0 & \dots & 0 & 0 & 0 \\ 0 & -1 & 1 & \dots & 0 & 0 & 0 \\ \vdots & \vdots & \vdots & \ddots & \vdots & \vdots & \vdots \\ 0 & 0 & 0 & \dots & -1 & 1 & 0 \\ 0 & 0 & 0 & \dots & 0 & -1 & 1 \end{bmatrix} \quad (5.97)$$

Finally, the criterion that has to be minimized and contains the sum of square errors and the roughness, can be written as [31] [34]:

$$Q = \varepsilon + \lambda R, \quad (5.98)$$

where  $\lambda \in \mathbb{R}$  is introduced to penalize the roughness, and therefore justifying the term *Penalized Least-Squares Algorithm*. Note that larger values of  $\lambda$  lead to smoother values of the modeled data in  $\hat{\mathbf{y}}$ . Therefore,  $\lambda$  is also named as *smoothing parameter* [33] [34]. Expressing equation 5.98 using vectors and matrices, yields [31] [34]:

$$Q = (\mathbf{y} - \hat{\mathbf{y}})^T (\mathbf{y} - \hat{\mathbf{y}}) + \lambda [(\mathbf{D}_m \hat{\mathbf{y}})^T (\mathbf{D}_m \hat{\mathbf{y}})] \quad (5.99)$$

$$= (\mathbf{y}^T - \hat{\mathbf{y}}^T) (\mathbf{y} - \hat{\mathbf{y}}) + \lambda [(\hat{\mathbf{y}} \mathbf{D}_m^T) (\mathbf{D}_m \hat{\mathbf{y}})] \quad (5.100)$$

$$= \mathbf{y}^T \mathbf{y} - \mathbf{y}^T \hat{\mathbf{y}} - \hat{\mathbf{y}}^T \mathbf{y} + \hat{\mathbf{y}}^T \hat{\mathbf{y}} + \lambda \hat{\mathbf{y}}^T \mathbf{D}_m^T \mathbf{D}_m \hat{\mathbf{y}} \quad (5.101)$$

$$= \mathbf{y}^T \mathbf{y} - 2\mathbf{y}^T \hat{\mathbf{y}} + \hat{\mathbf{y}}^T \hat{\mathbf{y}} + \lambda \hat{\mathbf{y}}^T \mathbf{D}_m^T \mathbf{D}_m \hat{\mathbf{y}} \quad (5.102)$$

The minimization of the criterion  $Q$  is achieved by calculating the derivative with respect to  $\hat{\mathbf{y}}$  and setting the obtained expression equal to zero [31] [34]:

$$\frac{\partial Q}{\partial \hat{\mathbf{y}}} = 0, \quad (5.103)$$

which gives:

$$0 = -2\mathbf{y}^T + 2\hat{\mathbf{y}}^T + 2\lambda \hat{\mathbf{y}}^T \mathbf{D}_m^T \mathbf{D}_m \quad (5.104)$$

$$\mathbf{y}^T = \hat{\mathbf{y}}^T (\mathbf{I} + \lambda \mathbf{D}_m^T \mathbf{D}_m) \quad (5.105)$$

Provided that the term  $(\mathbf{I} + \lambda \mathbf{D}_m^T \mathbf{D}_m)$  is invertible, leads to the following expression [31] [34]:

$$\hat{\mathbf{y}}^T = \mathbf{y}^T (\mathbf{I} + \lambda \mathbf{D}_m^T \mathbf{D}_m)^{-1} \quad (5.106)$$

Equation 5.106 demonstrates how to smooth data in  $\mathbf{y}$  with the help of the penalized least-squares algorithm.

However, in order to obtain the baseline, using the penalized least-squares method, a weighting matrix  $\mathbf{W}$  is introduced to the cost function in the following manner [34]:

$$\varepsilon(\mathbf{a}) = \sum_{i=1}^n w_i (y_i - \hat{y}_i)^2 \quad (5.107)$$

$$= (\mathbf{y} - \hat{\mathbf{y}})^T \mathbf{W} (\mathbf{y} - \hat{\mathbf{y}}), \quad (5.108)$$

where  $\mathbf{W}$  has the form of a diagonal matrix with  $w_i$  as the entries on its main diagonal and the dimension  $n \times n$  [34]:

$$\mathbf{W} = \begin{bmatrix} w_1 & \dots & 0 \\ \vdots & \ddots & \vdots \\ 0 & \dots & w_n \end{bmatrix} \quad (5.109)$$

Inserting  $\mathbf{W}$  into equation 5.106 leads to [34]:

$$\hat{\mathbf{y}} = (\mathbf{W} + \lambda \mathbf{D}_m^T \mathbf{D}_m)^{-1} \mathbf{W} \mathbf{y} \quad (5.110)$$

Implementing the adaptive and iteratively reweighting method

In each step of the iteration with the length  $t$ , the criterion  $Q$  has to be solved for every data point of  $\mathbf{y}$  [34]:

$$Q_t = \sum_{i=1}^n w_{i,t} (y_i - \hat{y}_{i,t})^2 + \lambda \sum_{j=2}^n (\hat{y}_{j,t} - \hat{y}_{j-1,t})^2 \quad (5.111)$$

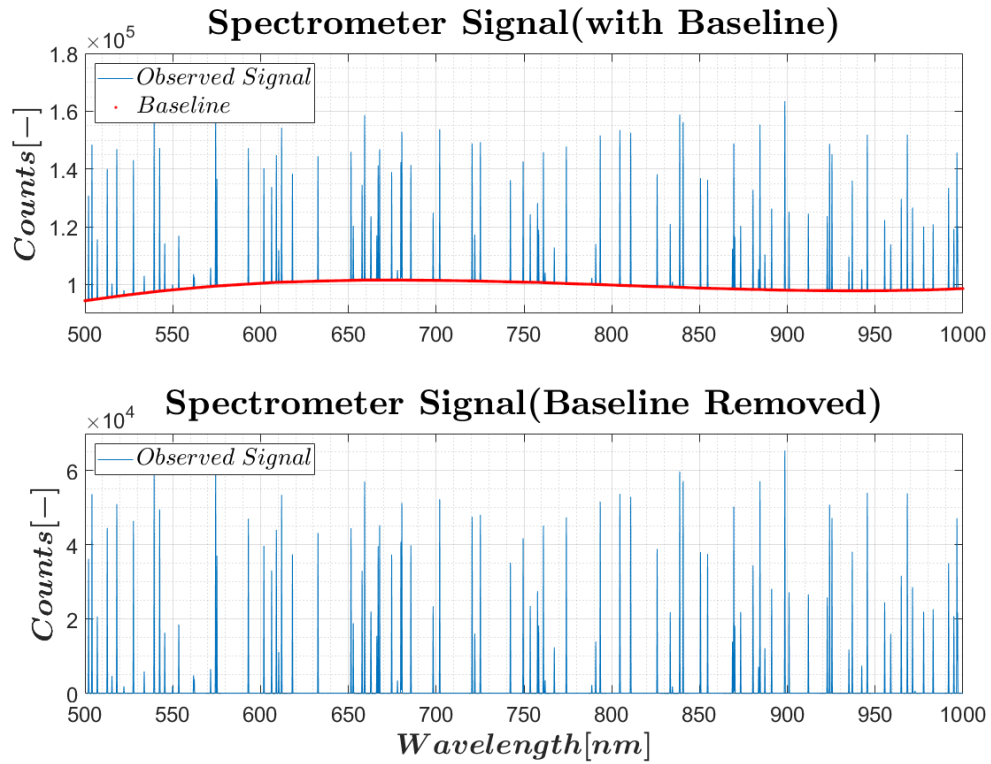
Furthermore, the entries  $w_i$  in the matrix  $\mathbf{W}$  are computed in an adaptive manner. This means, that  $w_i$  is obtained in every iteration as shown [34]:

$$w_{i,t} = \begin{cases} 0, & \text{if } y_i \geq \hat{y}_{i,t-1} \\ e^{-\frac{t(y_i - \hat{y}_{i,t-1})}{|d_{i,t}|}}, & \text{if } y_i < \hat{y}_{i,t-1} \end{cases} \quad (5.112)$$

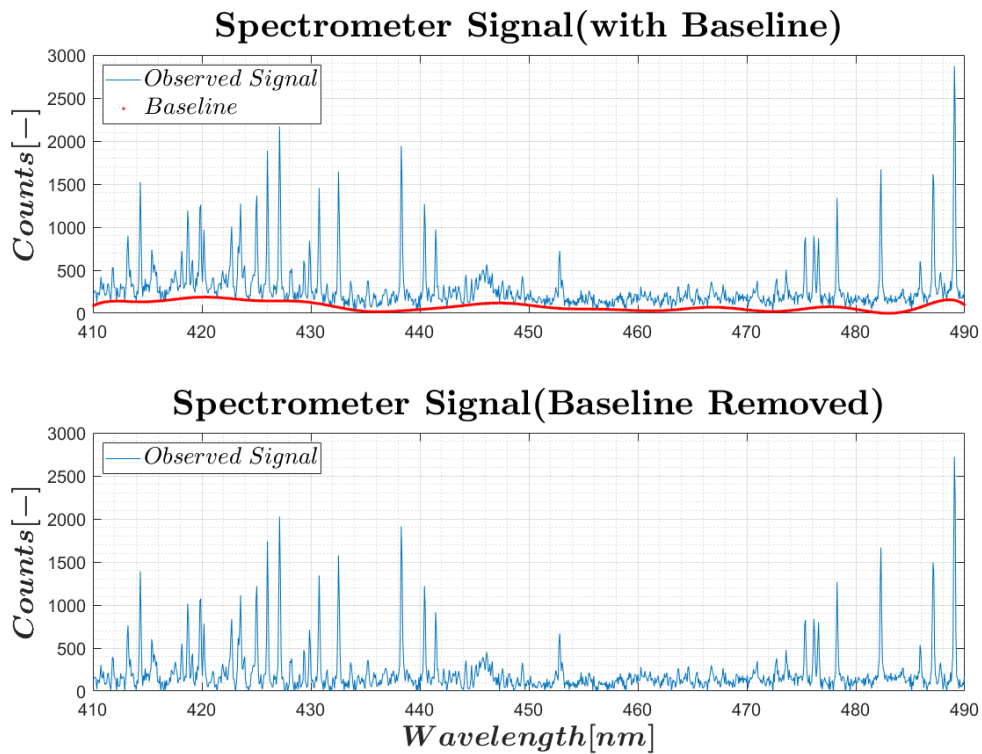
Whereby the subscript  $i$  denotes the  $i$ -th element of the corresponding vector and  $t$  the  $t$ -th iteration step [34].

Figure 5.6 and 5.7 depict, how this algorithm removes the baseline in synthetic and real spectrometer data.

The code to this section, provided in the appendix, is adapted from [34].



**Figure 5.6:** Baseline Removal, Demonstrated on Synthetic Spectrometer Data. Baseline modelled as a polynomial of order  $d = 3$



**Figure 5.7:** Baseline Removal, Demonstrated on Real Spectrometer Data



---

**Algorithm 3:** Adaptive Iteratively Reweighted Penalized Least-Squares Background Correction

---

**Input:**

- Vector of locations  $\mathbf{x}$
- Vector containing the observations  $\mathbf{y}$
- Value  $m$  (used for the  $m$ -th difference matrix  $\mathbf{D}_m$ )
- Maximum number of iterations  $maxNumberIter$
- Smoothing parameter  $\lambda$

**Output:**

- Model of the baseline  $\mathbf{y}_{BL}$

**Algorithm:**

1. Compute the length of the vector  $\mathbf{y}$
  2. Set up the difference-matrix  $\mathbf{D}_m$
  3. Perform an iteration (iteration variable  $t$ ), that ends, if
    - $t$  reaches the maximum number of iterations
    - the termination criterion is reached
    - (a) Set up the matrix  $\mathbf{W}$ , that has the weighted entries  $w_i$  on its main diagonal
    - (b) Compute the modelled baseline  $\mathbf{y}_{BL}$  as:  $\mathbf{y}_{BL} = (\mathbf{W} + \lambda \mathbf{D}_m^T \mathbf{D}_m)^{-1} \mathbf{W} \mathbf{y}$
    - (c) Compute  $\mathbf{d}$  (the difference between the observation and the model):  

$$\mathbf{d} = \mathbf{y} - \mathbf{y}_{BL}$$
    - (d) Define the termination criterion
      - Compute the absolute value of the sum of negative entries in  $\mathbf{d}$ :  

$$abs(sum(\mathbf{d}(\mathbf{d} < 0)))$$
      - Compute the sum of absolute values in  $\mathbf{y}$ :  $sum(abs(\mathbf{y}))$
      - Terminate the iteration, if the following criterion is fulfilled:  

$$abs(sum(\mathbf{d}(\mathbf{d} < 0))) < 0.001 \cdot sum(abs(\mathbf{y}))$$
    - (e) Set the values of the weighting vector  $\mathbf{w}$ 
      - if  $d_{i,t} < 0$ :  $w_{i,t} = e^{\frac{t \cdot (abs(\mathbf{d}(\mathbf{d} < 0)))}{abs(sum(\mathbf{d}(\mathbf{d} < 0)))}}$
      - if  $d_{i,t} \geq 0$ :  $w_{i,t} = 0$
  4. Put out the modelled baseline  $\mathbf{y}_{BL}$
-

### 5.3 Generating Synthetic Spectrometer Data

The aim of generating synthetic spectrometer data is to evaluate, whether the proposed methods in this chapter perform as desired and to quantify their accuracy. Therefore, these generated sets of data will be utilized for test purposes, before the methods are then applied to the real observed data sets.

According to [28] and [34], synthetic spectrometer data  $\mathbf{y}_s$  can be written as:

$$\mathbf{y}_s = \mathbf{b} + \mathbf{p} + \mathbf{n}, \quad (5.113)$$

where  $\mathbf{b}$  represents the background (i.e. a low order polynomial),  $\mathbf{p}$  the analytical signal and  $\mathbf{n}$  the noise. For the sake of simplicity,  $\mathbf{n}$  will be assumed to be white Gaussian noise with variance  $\sigma_n^2$ .

---

#### Algorithm 4: Generate Synthetic Spectrometer Data

---

1. Define  $\mathbf{x}$ , a column vector that contains  $n$  x-values ranging from  $x_{min}$  to  $x_{max}$
  2. Generate the baseline:
    - (a) Specify a maximum and minimum value for the baseline:  $y_{BL_{min}}$ ,  $y_{BL_{max}}$
    - (b) Generate  $n$  random data points within  $y_{BL_{min}}$  and  $y_{BL_{max}}$
    - (c) Approximate these data points with a polynomial of order  $d$
  3. Add noise to the baseline
    - (a) Perturb the data with Gaussian noise  $N(\mu, \sigma)$
  4. Create Gaussian-shaped peaks with  $\mu = 0$  and  $\sigma_p$ 
    - (a)  $\mathbf{y}_p = \frac{1}{\sqrt{2\pi\sigma_p^2}} e^{-\frac{(x-\mu)^2}{2\sigma_p^2}}$
    - (b) Normalize the values in  $\mathbf{y}_p$  by dividing them by  $\max(\mathbf{y}_p)$
    - (c) Specify a maximum and minimum value for the height of the peaks:  $peak_{min}$ ,  $peak_{max}$
    - (d) Specify the number of desired peaks  $nrPeaks$
    - (e) Generate random numbers within  $peak_{min}$  and  $peak_{max}$
    - (f) Multiply these random numbers with the normalized peak values
  5. Add the peaks at random locations
-

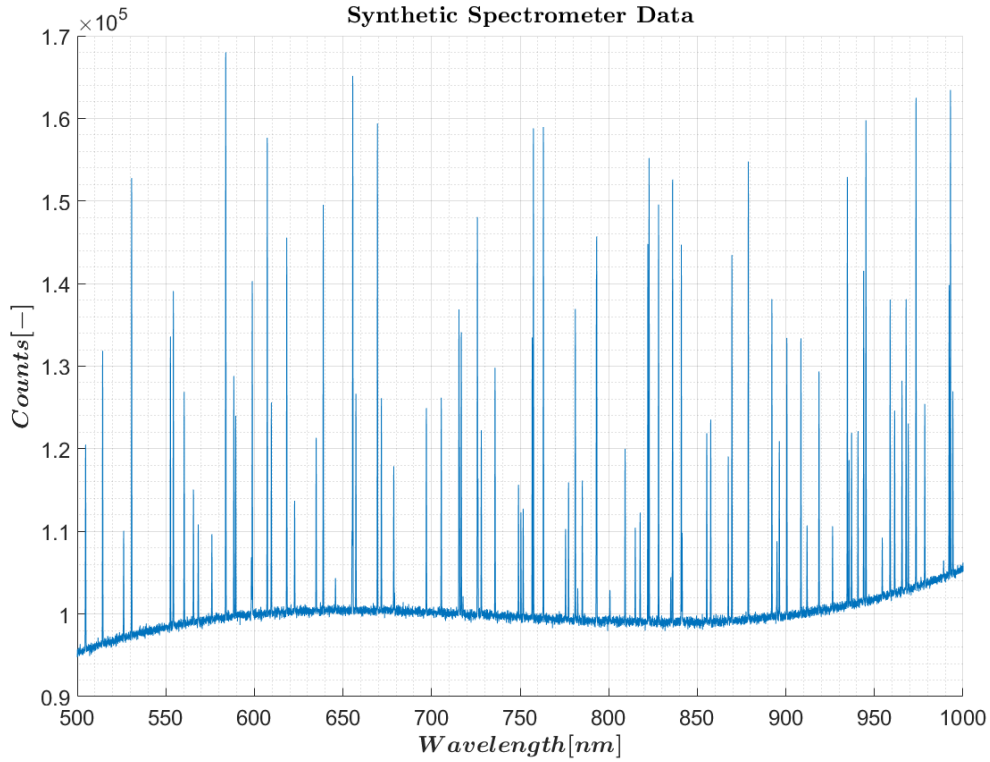


**Figure 5.8:** Synthetic Spectrometer Data, Baseline: Polynomial of Order  $d = 3$  and Noise  $\mu = 0$ ,  $\sigma = 300$

## 5.4 Peak Detection

After the observed signal was smoothed and the baseline was removed, the next step is to determine the peaks (i.e. local maxima) in the signal, in order to assign them to the corresponding chemical elements afterwards.

According to [35] a peak denotes a local maximum and, in contrast to that, a valley a local minimum.

The function  $f$  has a global maximum at  $x_0 \in D$  ( $D \subseteq \mathbb{R}$ ), if [36]:

$$f(x) \leq f(x_0) \quad \forall x \in D. \quad (5.114)$$

Consequently, a local maximum is given, if the following condition is satisfied [36]:

$$f(x) \leq f(x_0) \quad \forall x \in I \cap D, \quad (5.115)$$

whereby  $I$  represents a smaller interval, having  $x_0$  as its centre.

In contrast to that, a global minimum is represented as [36]:

$$f(x) \geq f(x_0) \quad \forall x \in D, \quad (5.116)$$

and, lastly, a local minimum as:

$$f(x) \geq f(x_0) \quad \forall x \in I \cap D. \quad (5.117)$$

The following algorithm for peak detection, that is presented in this work, is adapted from [37]. To foster understanding, a simple example with numbers is given.

The set of data with the length  $n$ , containing the observations can be written as:

$$\mathbf{y} = [y_1, \dots, y_n]^T. \quad (5.118)$$

$$\mathbf{y} = [0, 2, 5, 3, 1, 2, 4, 1]^T \quad (5.119)$$

Recapitulating the definition of a local maximum from above, the first step is to perform subtraction between the consecutive elements in  $\mathbf{y}$ , in order to determine the dominant values. This can be achieved with the built-in MATLAB function `diff`, that yields the following result for an input vector  $\mathbf{y}$  [38]:

$$\mathbf{y}_{diff} = [y_2 - y_1, y_3 - y_2, \dots, y_n - y_{n-1}]^T \quad (5.120)$$

$$\mathbf{y}_{diff} = [2, 3, -2, -2, 1, 2, -3]^T \quad (5.121)$$

The absolute values in  $\mathbf{y}_{diff}$  are not needed and only their sign is required for further steps. One possible way to extract the sign of each value in  $\mathbf{y}_{diff}$  is by using the `signum` function (see Figure 5.9), that is defined as [39]:

$$\text{sgn}(x) := \begin{cases} -1, & \text{if } x < 0 \\ 0, & \text{if } x = 0 \\ 1, & \text{if } x > 0 \end{cases} \quad (5.122)$$

The result of this step is an array that solely consists of  $-1, 0, 1$  as its entries. In the demonstrated example, the array  $\mathbf{y}_{diff,sign}$  looks like this:

$$\mathbf{y}_{diff,sign} = [1, 1, -1, -1, 1, 1, -1]^T \quad (5.123)$$

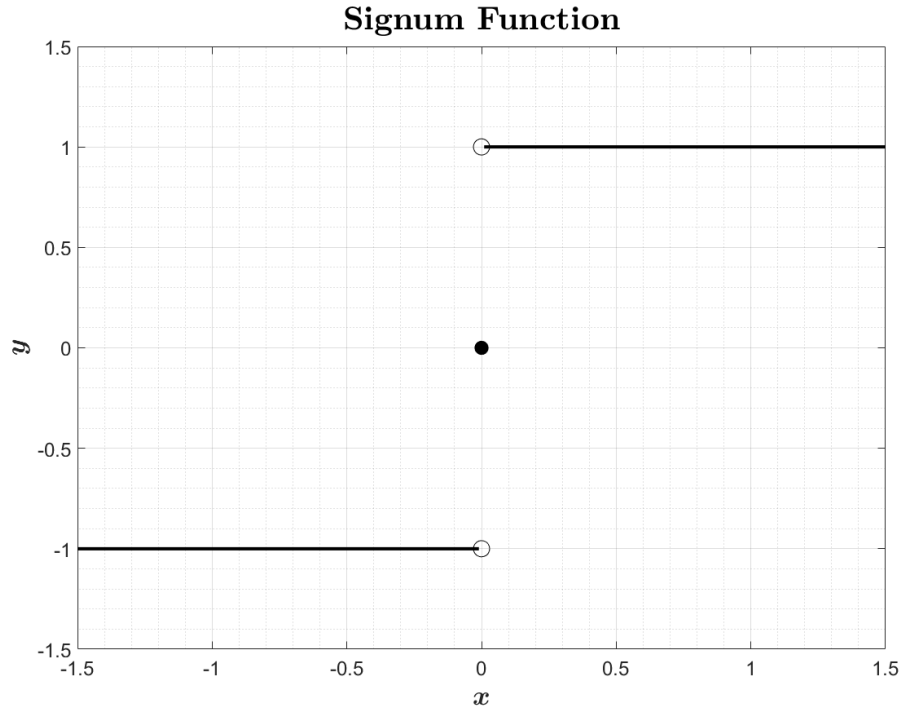


Figure 5.9: Signum Function

Taking a closer look at  $\mathbf{y}_{diff,sign}$  and comparing it with the initial array of observations  $\mathbf{y}$ , it becomes clear, that local maxima are represented as  $[1, -1]^T$ -pairs in  $\mathbf{y}_{diff,sign}$ . In order to determine these pairs (or more precisely, their location) in an array such as  $\mathbf{y}_{diff,sign}$ , [37] uses convolution.

Usually, in literature, the convolution operation is represented as [11]:

$$\mathbf{g} = \mathbf{h} * \mathbf{x}, \quad (5.124)$$

where the vectors  $\mathbf{g}$ ,  $\mathbf{h}$  and  $\mathbf{x}$  are given as [11]:

$$\mathbf{h} = [h_0, \dots, h_l]^T \quad (5.125)$$

$$\mathbf{x} = [x_0, \dots, x_f]^T \quad (5.126)$$

$$\mathbf{g} = [g_0, \dots, g_k]^T \quad (5.127)$$

Note that  $k$  is computed from  $l$  and  $f$  of  $\mathbf{h}$  and  $\mathbf{x}$  as follows [11]:

$$k = l + f \quad (5.128)$$

Each entry  $g_m$  in  $\mathbf{g}$  is obtained by summing up all products  $h_i x_j$ , which fulfill the following condition [11]:

$$i + j = m \quad (5.129)$$

Therefore, the  $m$ -th entry  $g_m$  in  $\mathbf{g}$  is calculated as [11]:

$$g_m = \sum_{\substack{i,j \\ i+j=m}} h_i x_j \quad (5.130)$$

Here, it proves convenient to use a convolution table to get the values in  $\mathbf{g}$ , see Figure 5.10.

		→ $j$				
		$x_0$	$x_1$	$x_2$	$x_3$	$x_4$
$h_0$	$h_0 x_0$	$h_0 x_1$	$h_0 x_2$	$h_0 x_3$	$h_0 x_4$	
$h_1$	$h_1 x_0$	$h_1 x_1$	$h_1 x_2$	$h_1 x_3$	$h_1 x_4$	
$h_2$	$h_2 x_0$	$h_2 x_1$	$h_2 x_2$	$h_2 x_3$	$h_2 x_4$	
$h_3$	$h_3 x_0$	$h_3 x_1$	$h_3 x_2$	$h_3 x_3$	$h_3 x_4$	
↓ $i$						

**Figure 5.10:** Convolution table in the case of  $l = 3$  and  $f = 4$ , [11]

With the help of the table in Figure 5.10 and equation 5.130, each entry  $g_m$  of  $\mathbf{g}$  can now be computed [11]:

$$g_0 = h_0 x_0 \quad (5.131)$$

$$g_1 = h_0 x_1 + h_1 x_0 \quad (5.132)$$

$$g_2 = h_0 x_2 + h_1 x_1 + h_2 x_0 \quad (5.133)$$

$$g_3 = h_0 x_3 + h_1 x_2 + h_2 x_1 + h_3 x_0 \quad (5.134)$$

$$g_4 = h_0 x_4 + h_1 x_3 + h_2 x_2 + h_3 x_1 \quad (5.135)$$

$$g_5 = h_1 x_4 + h_2 x_3 + h_3 x_2 \quad (5.136)$$

$$g_6 = h_2 x_4 + h_3 x_3 \quad (5.137)$$

$$g_7 = h_3 x_4 \quad (5.138)$$

$$(5.139)$$

Using the convolution table and the equations for computing the entries in  $\mathbf{y}_{peaks}$ , the

$[1, -1]^T$ -pairs in  $\mathbf{y}_{diff,sign}$  can be located. In order to perform the convolution-operation [11][37]:

$$\mathbf{y}_{peaks} = \mathbf{y}_{diff,sign} * [-1, 1]^T, \quad (5.140)$$

the first step is to flip the entries in the  $[1, -1]^T$ -vector, which gives  $[-1, 1]^T$ . Next, the resulting entries in  $\mathbf{y}_{peaks}$  are obtained as proposed in equations 5.131- 5.138:

$$\mathbf{y}_{peaks} = [-1, 0, 2, 0, -2, 0, 2, -1]^T \quad (5.141)$$

Finally, the entries in  $\mathbf{y}_{peaks}$ , that are equal to 2, indicate the location of a local maxima in the vector of observations  $\mathbf{y}$  and can be detected with the MATLAB function `find` [37] [40].

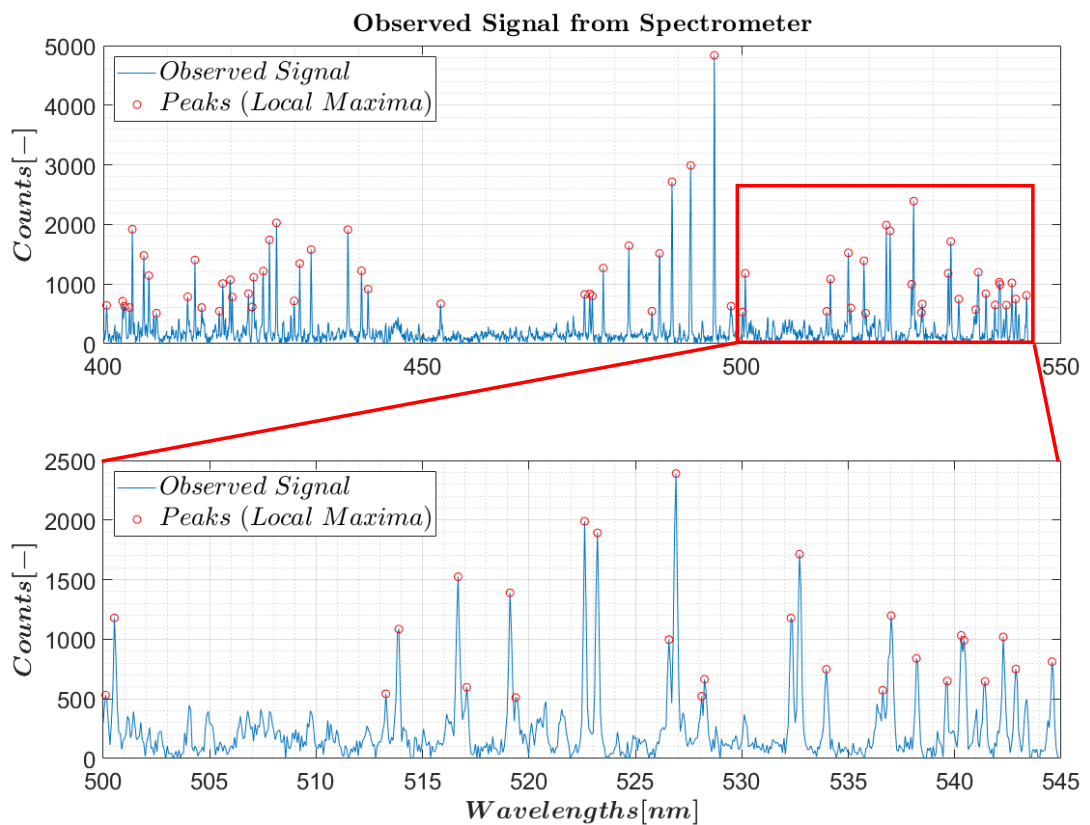


**Figure 5.11:** Detecting the Peaks in a Set of Data from a Spectrometer.  $Window\ size = 10$ ,  $Threshold = 500$ , hence peaks with  $Counts$  lower than 500 are ignored

---

**Algorithm 5: Peak Detection**

---

**Input:**

- Vector of locations  $\mathbf{x}$
- Vector of observations  $\mathbf{y}$
- Window size, in which the peak shall be detected
- Threshold (peaks that are smaller than this value will be ignored)

**Output:**

- Locations of the local maxima  $\mathbf{x}_{peak}$  in the input signal
- Value of the local maxima  $\mathbf{y}_{peak}$  in the input signal

**Algorithm:**

1. Compute the differences between the adjacent values in  $\mathbf{y}$ :  $\mathbf{y}_{diff} = diff(\mathbf{y})$
  2. Extract the sign of each value in  $\mathbf{y}_{diff}$ :  $\mathbf{y}_{diff,sign} = sign(\mathbf{y}_{diff})$
  3. Perform convolution, to detect all  $[1, -1]^T$ -pairs  $\mathbf{y}_{diff,sign}$ :  
$$\mathbf{y}_{peaks} = conv(\mathbf{y}_{diff,sign}, [-1, 1]^T)$$
  4. In a `for`-loop, detect the maxima in each window:
    - (a) Detect all possible maxima within the window
    - (b) Check, whether each detected maxima is bigger than the threshold
    - (c) Compare each possible maxima with the other ones, to obtain the greatest one within the window
  5. Put out the results of the function:
    - (a)  $\mathbf{y}_{peak}$
    - (b)  $\mathbf{x}_{peak}$
-



# Chapter 6

## Results and Conclusion

### 6.1 Results

In the first step of processing the observations by the spectroscope, the data is loaded into the MATLAB-workspace. For each steel sample, approximately 100 spectra were obtained. During this thesis, nine samples were examined, amounting to roughly 900 spectra in total. The chemical composition of each of these samples is given in Table 6.1. The steel samples used in this work were taken from a real EAF and the contents of each chemical element were determined with the help of a spark spectrometer.

Sample	Chemical Element									
	C	Si	Mn	P	S	Al	Cr	Cu	Mo	Ni
1	0.202	0.33	0.85	0.010	0.006	0.064	0.04	0.056	0.01	0.23
2	0.102	0.00	0.37	0.007	0.006	0.301	0.09	0.055	0.01	0.05
3	0.144	0.00	0.51	0.018	0.006	0.392	0.12	0.071	0.02	0.06
4	0.176	0.28	1.49	0.010	0.005	0.045	0.06	0.052	0.01	0.03
5	0.184	0.69	1.95	0.022	0.004	0.087	0.12	0.056	0.01	0.05
6	0.169	0.00	0.32	0.009	0.007	0.223	0.07	0.049	0.01	0.05
7	0.166	0.00	0.37	0.024	0.009	0.272	0.15	0.046	0.02	0.06
8	0.194	0.45	1.48	0.022	0.007	0.074	0.12	0.058	0.01	0.05
9	0.191	0.33	0.47	0.025	0.007	0.063	0.99	0.07	0.22	1.03

**Table 6.1:** The Samples and Their Chemical Composition. The contents are given in wt-%.

Next, if required, the noise, that is contained in the data, gets reduced using the smoothing technique by Savitzky and Golay, described in chapter 5. It is important to perform this procedure prior to the baseline removal, to get a better fit of the baseline.

After the baseline has been removed, the peaks can be detected, which is accomplished as described in the previous chapter. Obtaining the location of each peak permits to de-

termine its wavelength, which in return can be put into the database [41] to assign the chemical elements (i.e. *Fe I, Mn I, Cr I,...*) to each corresponding local maxima.

In the last stage, so-called *calibration curves* are established, that permit to evaluate, whether the peak ratios (i.e.  $\frac{I_{Cr}}{I_{Fe}}$ ,  $I$  denotes the intensity, or the value of the peak) correlate with the actual content of each chemical element in the sample. What is more, the calibration curve has to be linear, since (as stated in the chapter *Atomic Spectroscopy*) the intensity of the emitted photons is proportional to the elements' concentration in the inspected sample. In addition to this, after the calibration curve has been established for a specific element (with samples of known chemical composition), it permits to obtain the content of this element from a sample of unknown chemical composition.

Figure 6.1 shows an example of how such a calibration curve may look like in a general case. Each red circle denotes the ratio of two local maxima in one spectrum. With the help of a histogram, it has been firstly evaluated and in the following consequence confirmed, that these red circles follow a normal distribution.

In order to check and quantify the linear dependency between the peak ratios and the actual contents of a given element in the sample, the so-called *correlation-coefficient* was computed as follows [42]:

$$\rho(\mathbf{x}, \mathbf{y}) = \frac{1}{n-1} \sum_{i=1}^n \left( \frac{x_i - \mu_x}{\sigma_x} \right) \left( \frac{y_i - \mu_y}{\sigma_y} \right) \quad (6.1)$$

With:

$\mathbf{x}, \mathbf{y} \dots$  Random variables

$\mu_x \dots$  Mean of  $\mathbf{x}$

$\mu_y \dots$  Mean of  $\mathbf{y}$

$\sigma_x \dots$  Standard deviation of  $\mathbf{x}$

$\sigma_y \dots$  Standard deviation of  $\mathbf{y}$

Another representation of the correlation coefficient with the help of the covariance of the variables  $\mathbf{x}$  and  $\mathbf{y}$  is given as [42]:

$$\rho(\mathbf{x}, \mathbf{y}) = \frac{cov(\mathbf{x}, \mathbf{y})}{\sigma_x \sigma_y} \quad (6.2)$$

The overall computation of  $\rho(\mathbf{x}, \mathbf{y})$  can be accomplished with the help of the MATLAB-function `corrcoef`, that returns the following matrix [42]:

$$\mathbf{R} = \begin{bmatrix} \rho(\mathbf{x}, \mathbf{x}) & \rho(\mathbf{x}, \mathbf{y}) \\ \rho(\mathbf{y}, \mathbf{x}) & \rho(\mathbf{y}, \mathbf{y}) \end{bmatrix} \quad (6.3)$$

Note that the main diagonal of  $\mathbf{R}$  has the value 1 on its entries, since  $\rho(\mathbf{x}, \mathbf{x}) = 1$  and

$$\rho(\mathbf{y}, \mathbf{y}) = 1.$$

Next, the dependence between the two random variables  $\mathbf{x}$  and  $\mathbf{y}$  (in this work: peak ratios and contents of the chemical element) is described with a model based on linear regression [43]:

$$y = \beta_1 x + \beta_0 + \varepsilon \quad (6.4)$$

With,

$\beta_0$  ... Intercept on y-axis

$\beta_1$  ... Slope (also termed *regression coefficient*)

$\varepsilon$  ... Error term

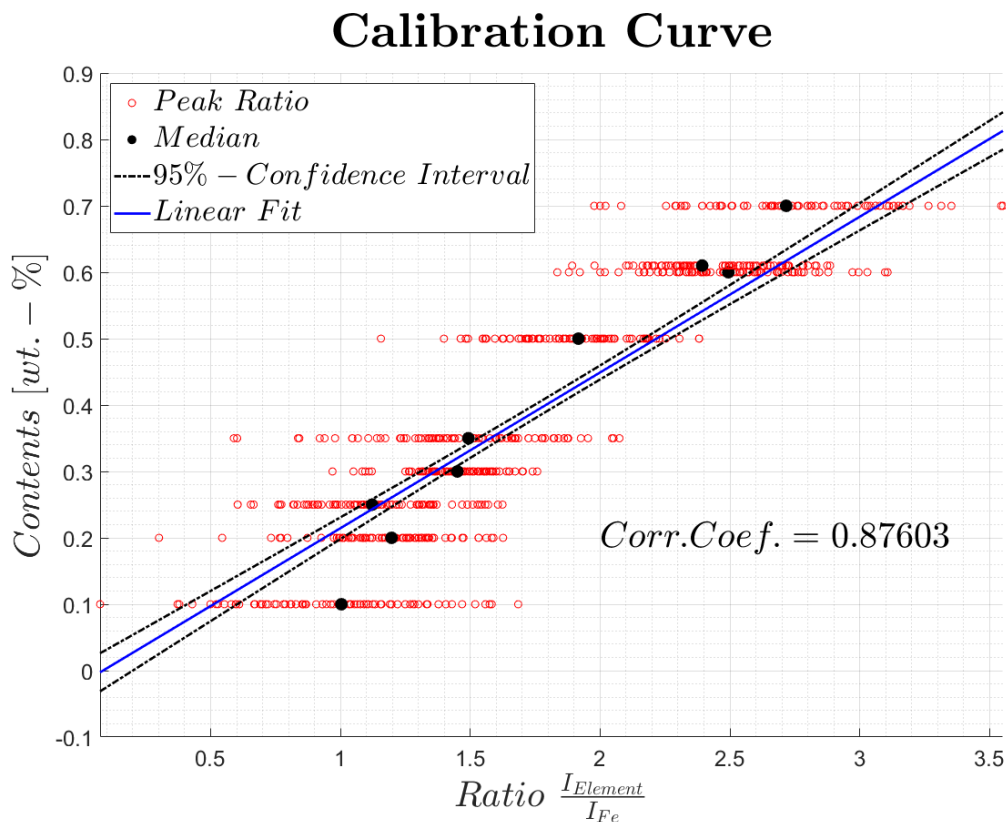


**Figure 6.1:** Example of a Calibration Curve. Each horizontal plot of red circles represents one steel sample with a specific content of a certain chemical element

A more useful and lucid representation of the data in Figure 6.1 can be given with the aid of *box-whisker diagrams* (or *boxplots*) [44]. Figure 6.2 illustrates, how such a boxplot looks like. The *interquartile range* is defined as [44] [45]:

$$iqr = Q_3 - Q_1 \quad (6.5)$$

With,

$Q_3$  ... 75-th percentile

$Q_1$  ... 25-th percentile

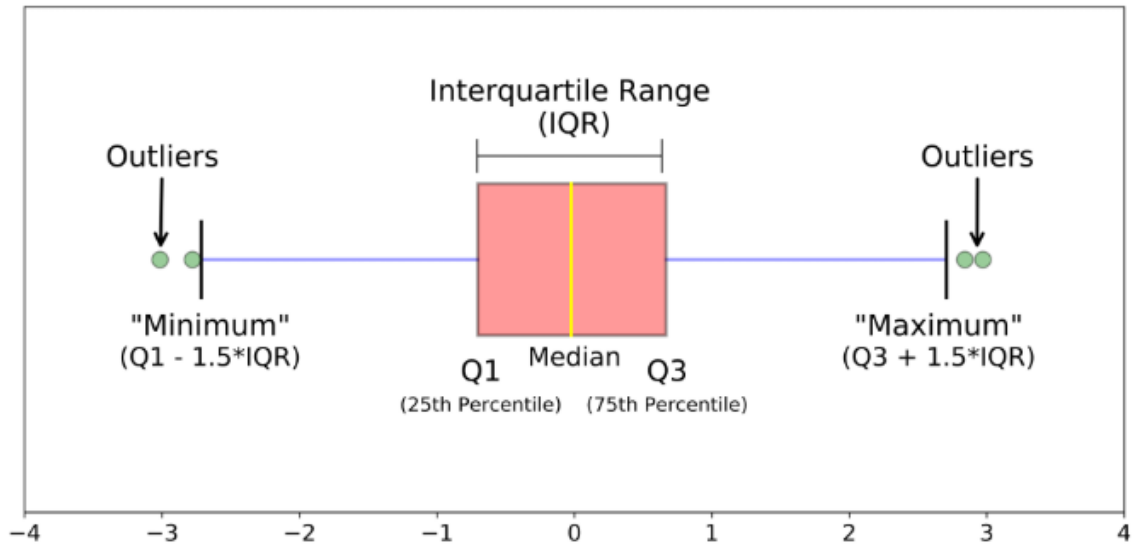


**Figure 6.2:** Overview of the Typical Parts of a Boxplot, adapted from [12]

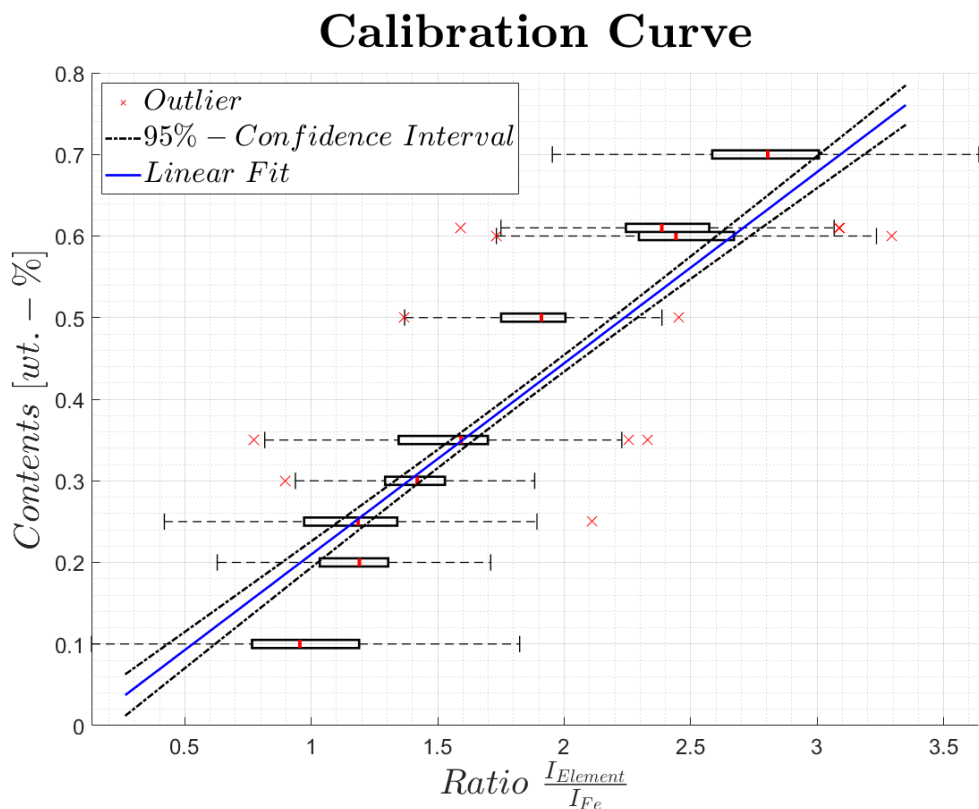


**Figure 6.3:** Example of a Calibration Curve. Data represented with the help of boxplots

An overview of the overall procedure from the raw spectrometer data to a calibration curve is given with the help of Figure 6.4 and 6.5.

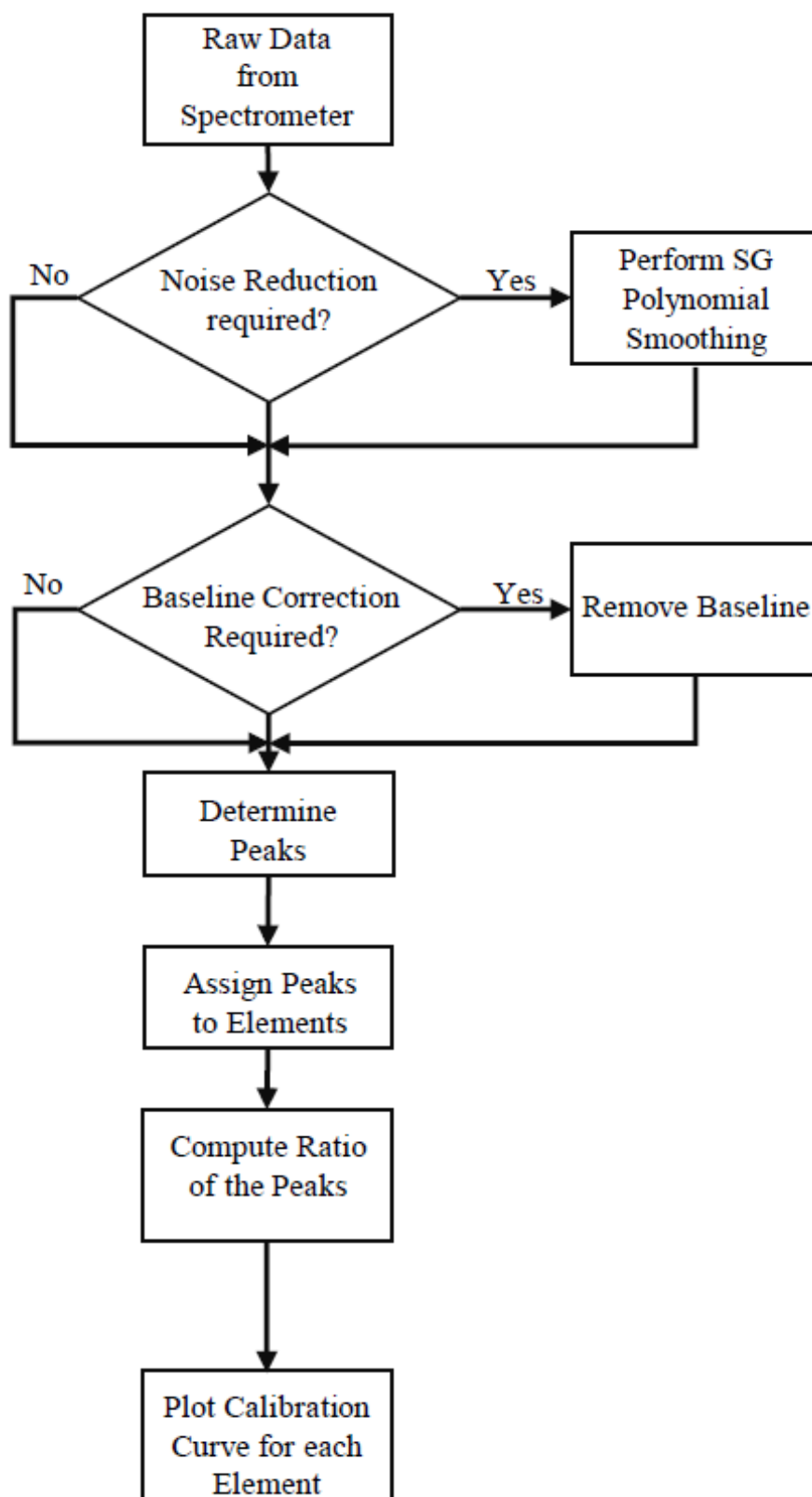


**Figure 6.4:** Flowchart, Illustrating Each Step from Raw Spectrometer Data to the Calibration Curves

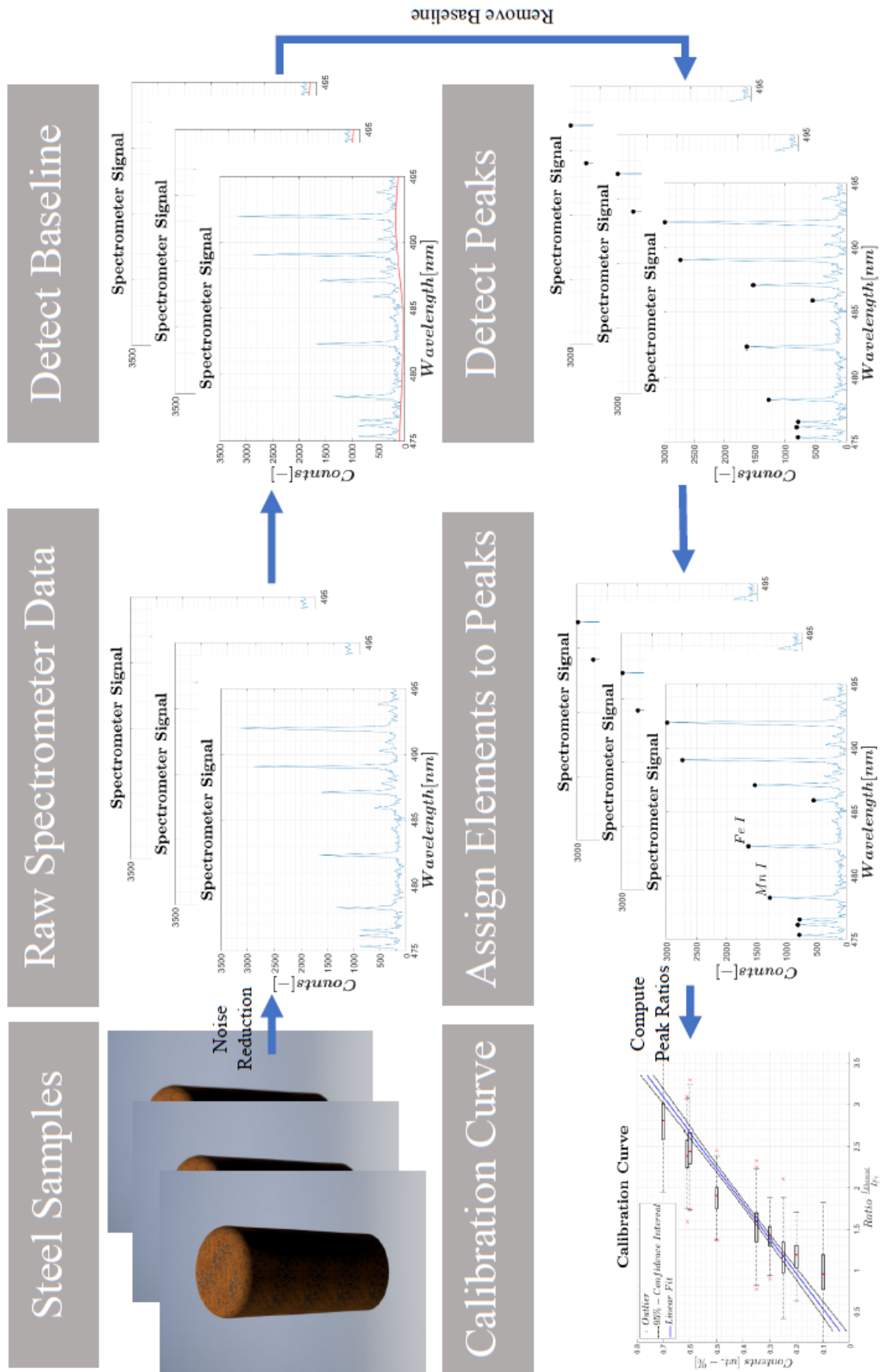


**Figure 6.5:** Schematic Overview of the Overall Process from Raw Spectrometer Data to a Calibration Curve

In the following, Figures 6.6 to 6.15 depict the correlation curves for each of the chemical elements, depicted in Table 6.1.

### Calibration Curve (Chromium)

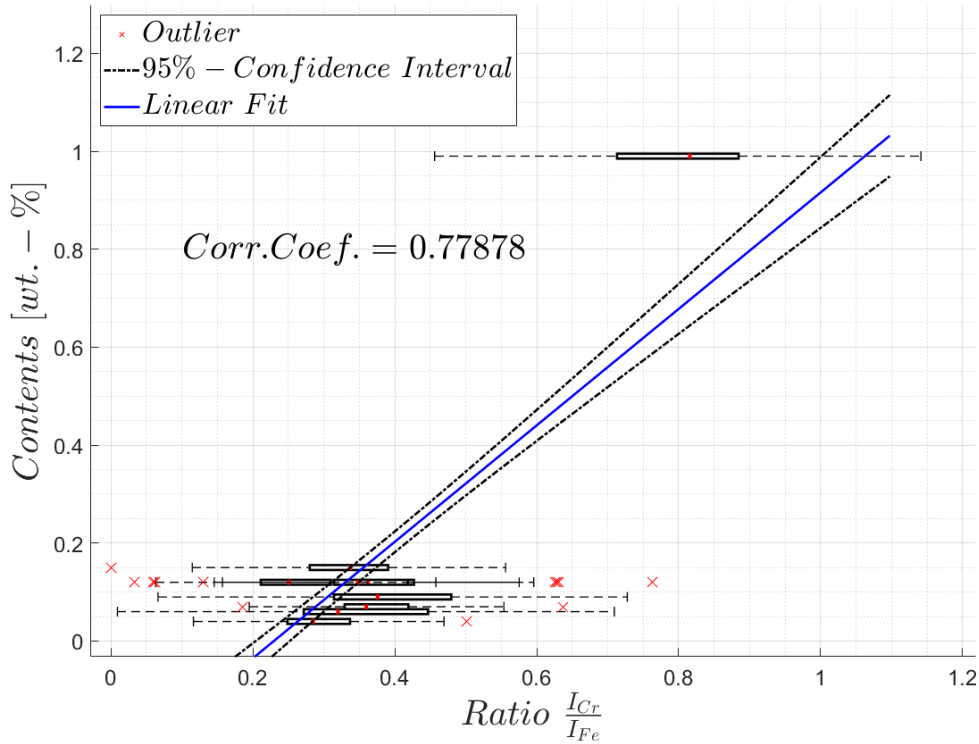


Figure 6.6: Calibration Curve (Chromium)

### Calibration Curve (Molybdenum)

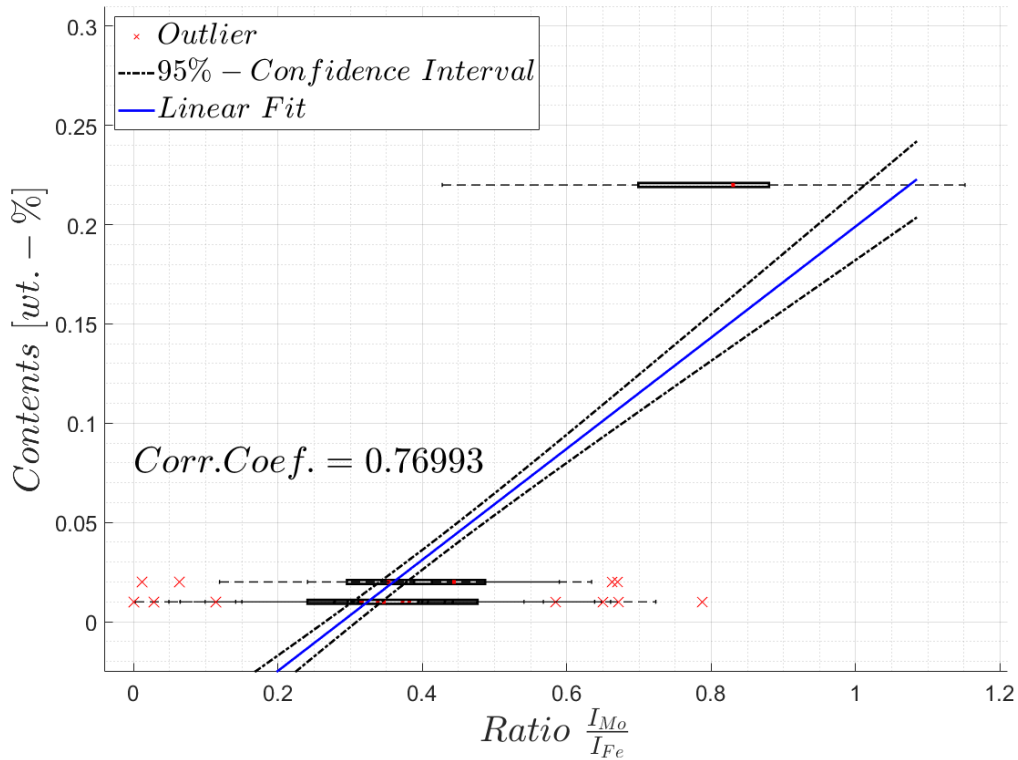


Figure 6.7: Calibration Curve (Chromium)

### Calibration Curve (Nickel)

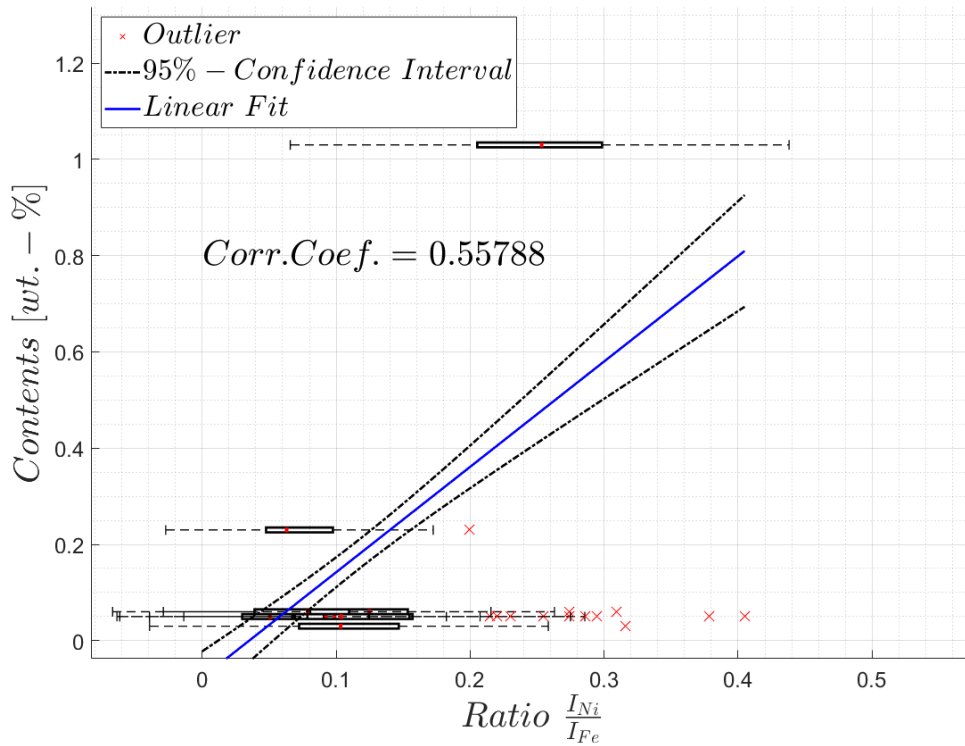


Figure 6.8: Calibration Curve (Nickel)

### Calibration Curve (Copper)

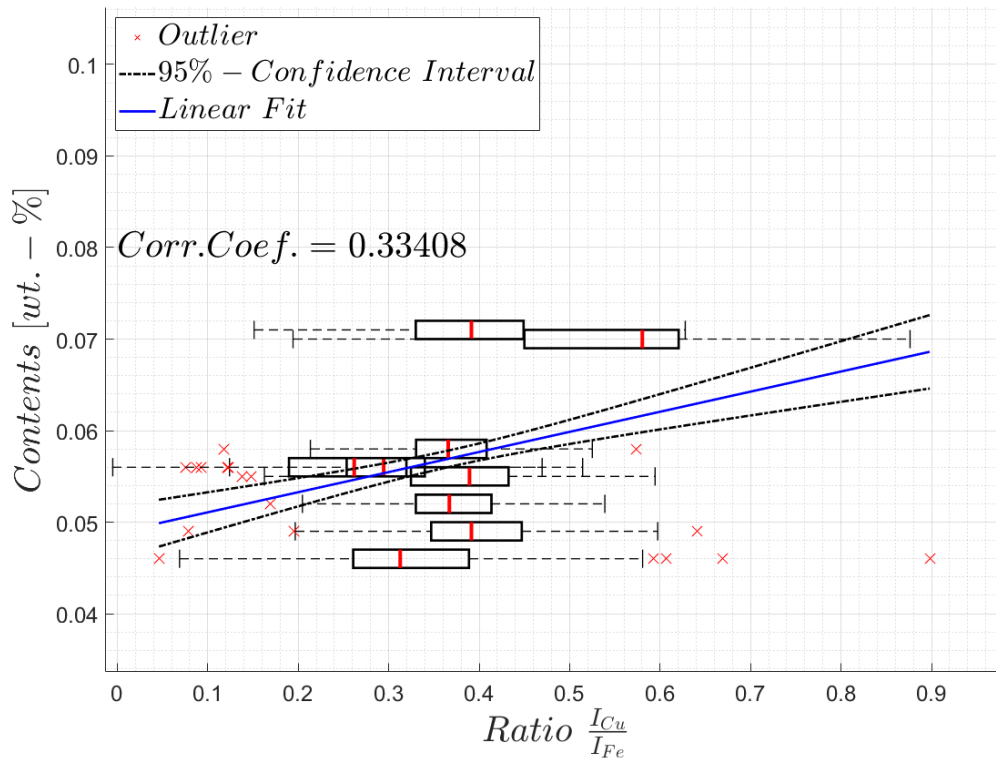


Figure 6.9: Calibration Curve (Copper)



### Calibration Curve (Manganese)

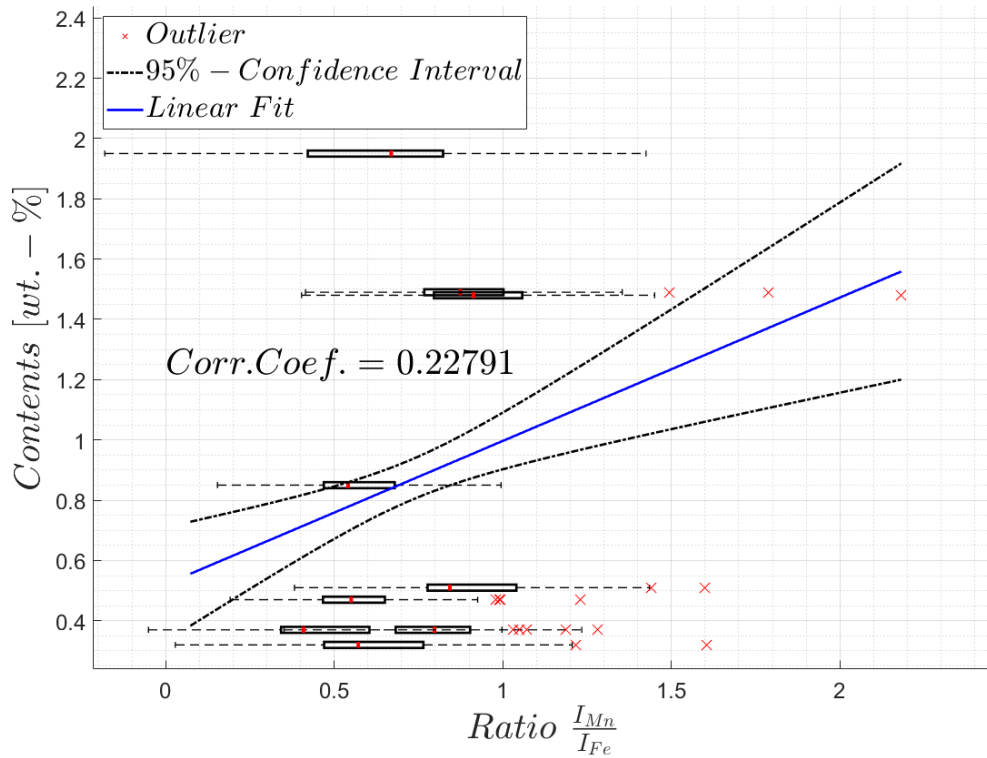


Figure 6.10: Calibration Curve (Manganese)

### Calibration Curve (Carbon)

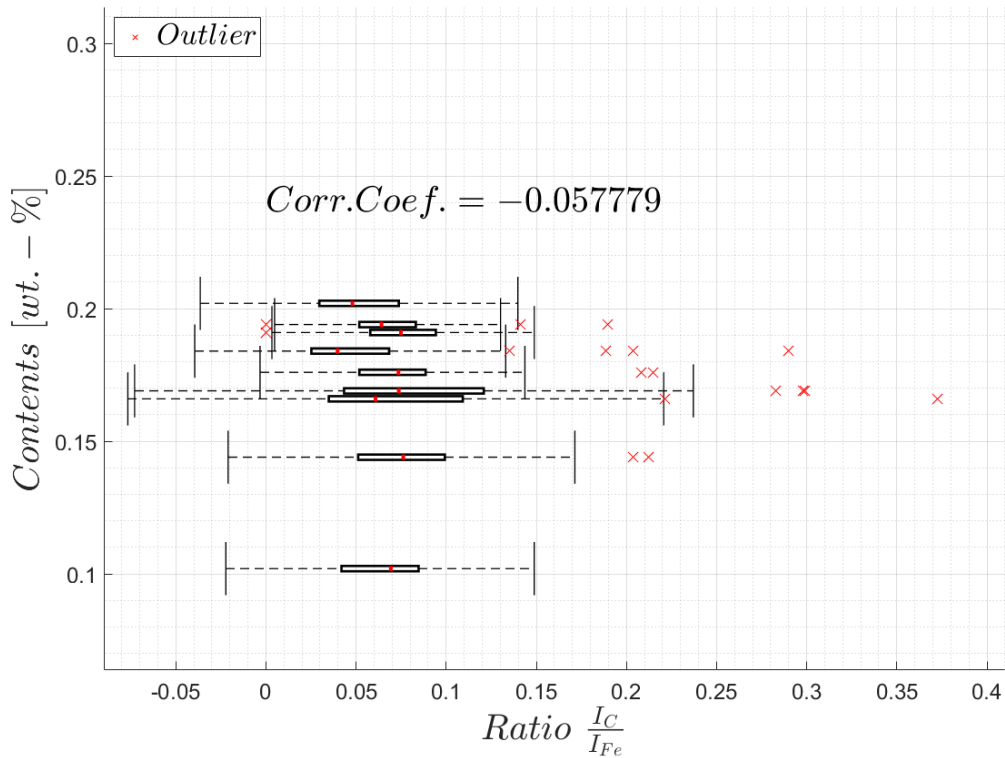


Figure 6.11: Calibration Curve (Carbon)

### Calibration Curve (Silicon)

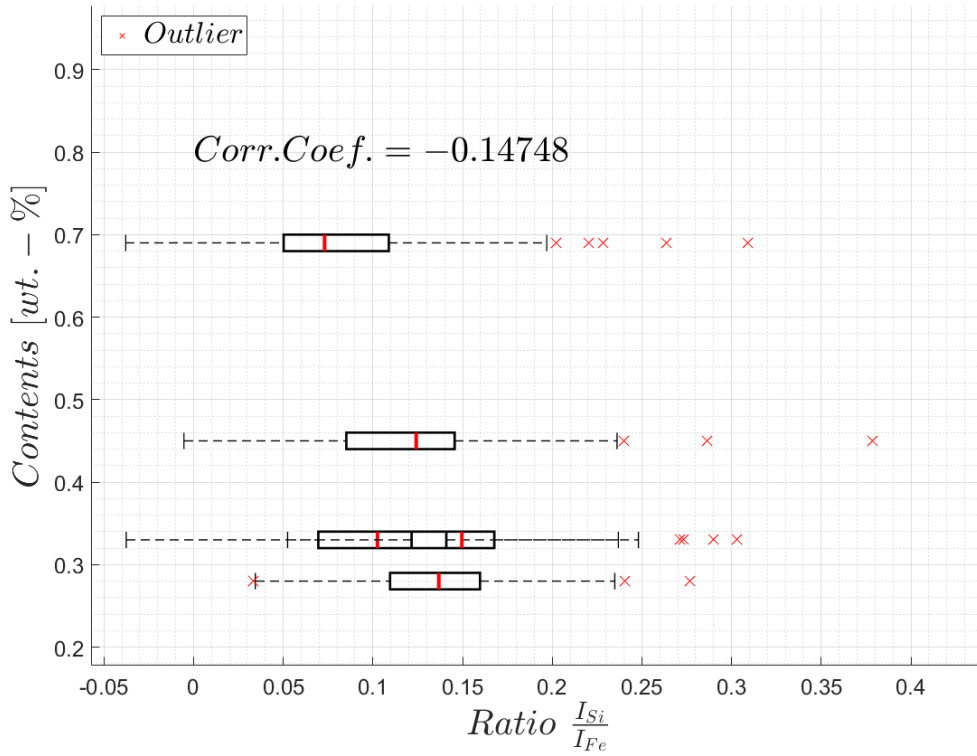


Figure 6.12: Calibration Curve (Silicon)

### Calibration Curve (Aluminum)

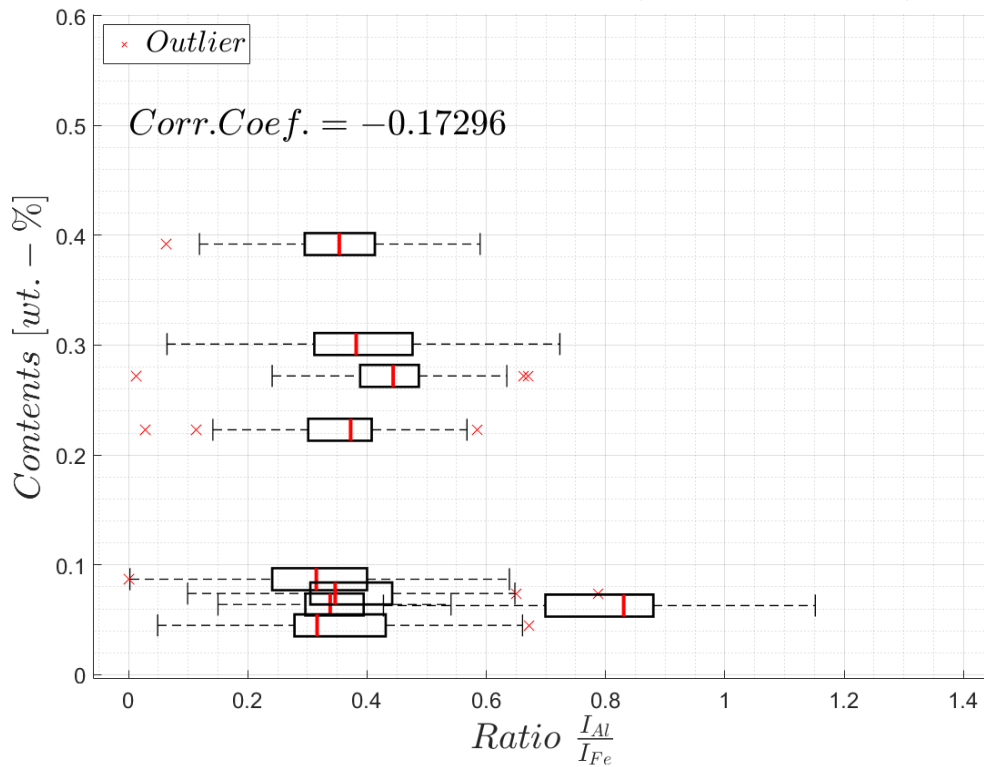


Figure 6.13: Calibration Curve (Aluminum)

### Calibration Curve (Phosphorous)

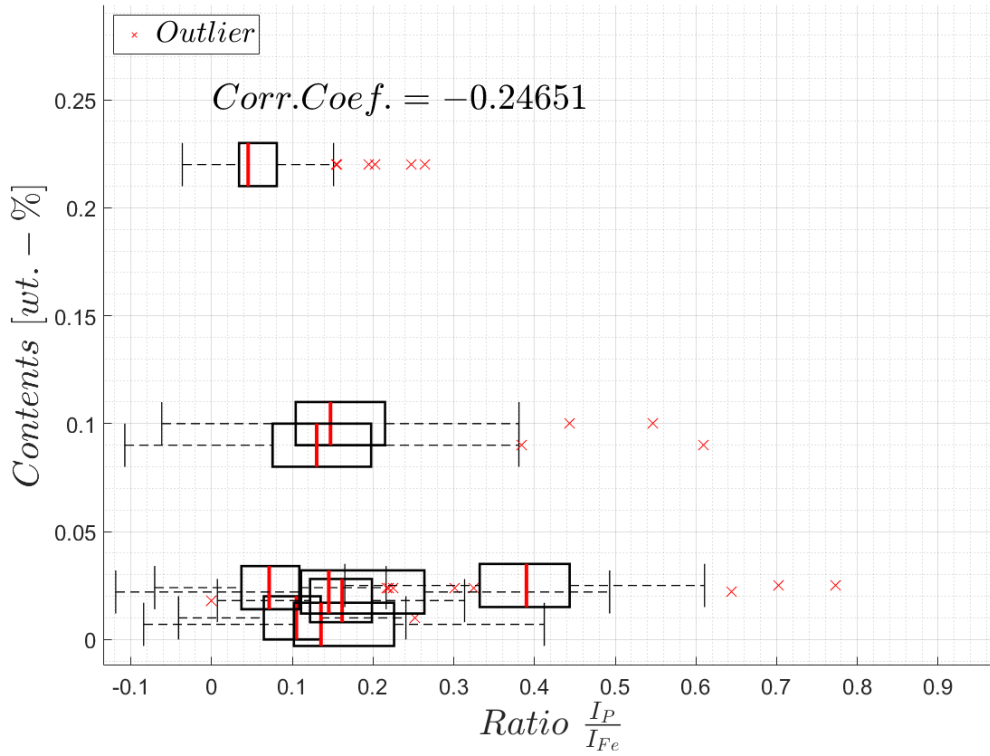


Figure 6.14: Calibration Curve (Phosphorous)

### Calibration Curve (Sulfur)

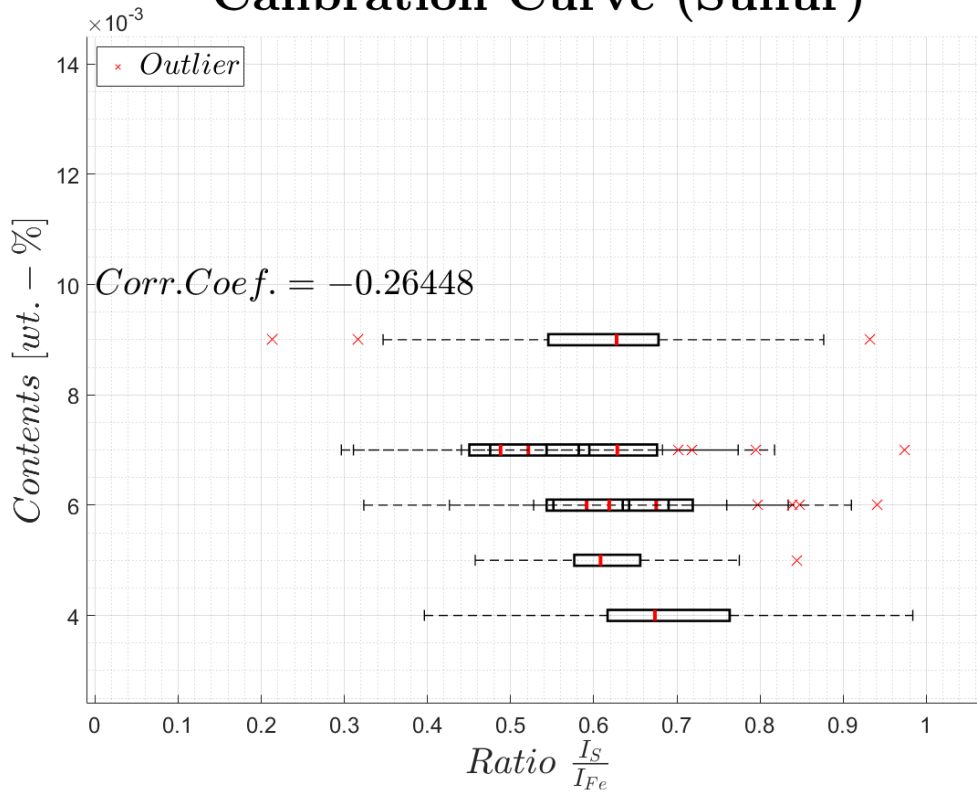


Figure 6.15: Calibration Curve (Sulfur)

## 6.2 Conclusion

The results of this thesis show, that the investigated method does not yield the desired results and is therefore not suitable for determining the composition of the liquid steel inside an EAF.

Even though, the calibration curves of chromium, molybdenum and nickel may seem promising at the first glance, due to the relatively high overall correlation coefficients of approximately 0.56 – 0.78, a lot of care has to be taken, when interpreting these results.

In the case of chromium, for instance, at lower contents (0.04-0.15 wt.-%), there is very little dependency observable between the peak ratios and the actual *Cr*-contents in the samples.

The same applies to the calibration curves of molybdenum and nickel.

In the case of manganese, the overall correlation coefficient is even lower, especially in the region below 1 wt.%, similar to the findings by [46].

Note, that all the remaining elements, modelling the data with the help of linear regression has been omitted, since it would not deliver reasonable results, due to their low correlation coefficients.

Another flaw of this discussed method to determine the chemical composition of the liquid steel is the fact, that the content of carbon in the molten sample is impossible to determine, due to the fact, that the electrode mainly consists of graphite (see chapter 2) and therefore falsifies the results. This may explain, why there is almost no correlation between the data in the calibration curve for carbon.

One conclusion, that can be drawn from the presented findings is, that due to the uncontrolled nature of the arc (or, instability of the arc) between the graphite electrode and the molten steel, the arc is not a suitable excitation source for atomic emission spectroscopy. Hence, that is why, in laboratory applications, the plasma is established with the help of an *inductively coupled plasma burner*, delivering a stable plasma. Whereby the term *stable* refers to the temperature here. The effect of the temperature (that may be caused by an unstable arc, as it is the case in an EAF) on spectroscopy is discussed in chapter 3.

Furthermore, the laboratory EAF, that was available to conduct the experiments, does not completely resemble a furnace, that is utilized in steelmaking industry. For instance, the laboratory furnace was equipped with a DC-power supply and in consequence of its small size, there was no chance to generate a bath of molten steel (the steel sample could only be liquified at its top). For this reason, there was no possibility to examine the effect of the slag on the measurements. Therefore, this leads to the assumption, that the small scale furnace may not be sufficiently suitable to be conclusive with respect to its industrial used version.

# Appendix A

## Code

### A.1 Savitzky-Golay Polynomial Smoothing

```
1 function [ySmoothed] = sgFilt(y,order, ls)
2 % Description: This function performs a Savitzky-Golay ...
   polynomial smoothing
3 % Inputs: y...a vector containing noisy data (observations)
4 %         order...defines the order of the fitting polynomila
5 %         ls...supportlength
6
7 % Output: ySmoothed...smoothed data
8
9
10
11 % Author: Florian Floh
12 % (c) 2019, Florian Floh
13 % email: florian.floh@stud.unileoben.ac.at
14
15 % Check, whether the input y is a column vector, if not, turn it ...
   into a
16 % column vector
17 if (iscolumn(y) ~=1)
18     y = y';
19 end
20
21 % The order of the polynomial must be less than the support-length
22 % Check, whether this is true here. If not, display an error message
23 if (order >= ls)
24     error(['The order of the polynomial has to be smaller than the',...
25         ' support-length!']);
26 end
27
```

```

28 % Another important aspect, that has to be checked, is, whether the
29 % support-length is an odd number
30 if(mod(ls,2) == 0 )
31 error('Support-Length must be an odd number!');
32 end
33
34
35 % Compute the half-length lh
36 lh = (ls-1)/2;
37 % Define a column-vector that contains the local x-coordinates
38 x = linspace(-lh,lh, ls)';
39
40 % Set up the Vandermonde-matrix
41 Vb = ones(length(x), order+1);
42 Vb(:,order) = x;
43
44 for k=order-1:-1:1
45 Vb(:,k) = x.*Vb(:,k+1);
46 end
47
48 % Compute B (i.e. the matrix, that represents the so-called
49 % Savitzky-Golay smoothing filters
50 B = Vb*pinv(Vb);
51
52 % Extract the centre row of B (or the centre column would also work,
53 % since B is symmetric)
54 bC = B(lh+1, :);
55 %bC = B(:,lh+1);
56
57 % The smoothed data is then obtained by performing a convolution ...
58 % of the
59 % noisy data with the centre row of B
60 ySmoothed = conv(y,bC, 'same');
61
62 % In order to perform an end point correction, both the upper ...
63 % half and
64 % lower half of the matrix B have to be extracted
65 BuppH = B(1:lh, :);
66
67 BlowH = B((end-lh+1):end, :);
68
69 % Perform the endpoint-correction
70 ySmoothed(1:lh) = BuppH * y(1:ls);
71 ySmoothed((end-lh+1):end) = BlowH * y((end - ls+1):end);
72 end

```

## A.2 Background Removal by Minimizing a Non-Quadratic Cost Function

```
1 function [yBL] = backgroundCorrectionNonQuadr(x,y,order,s,costfct)
2 % Description: The aim of this function is to provide an ...
3 % algorithm, that
4 % models the baseline of the input signal, which can later be ...
5 % subtracted in
6 % the corresponding script file
7
8 % Inputs: x... a column vector, containing the locations of the
9 % observations
10 % y... a column vector, containing the observations
11 % order... the order of the baseline model
12 % s... the threshold value for the cost functions
13 % fct... a char, that represents the desired cost function
14
15 % Output: yBL...a column vector, that contains the values of the ...
16 % modelled
17 % baseline
18
19 % Author: Florian Floh
20 % (c) 2019, Florian Floh
21 % email: florian.floh@stud.unileoben.ac.at
22
23 % Check, whether the input y is a column vector, if not, turn it ...
24 % into a
25 % column vector
26 if (iscolumn(y) ~= 1)
27     y = y';
28 end
29 % Do the same with the x-vector
30 if(iscolumn(x) ~= 1)
31     x = x';
32 end
33
34 % Set the maximum number of iterations
35 maxNumberIter = 100000;
36 % limit value alpha
37 alphaMax = 0.5;
38
39 % Perform a coordinate transformation, to get a better conditioned
```

```

38 % Vandermonde-matrix:
39 x = (x-mean(x))/std(x);
40
41 % Use Horner's form to get the Vandermonde-matrix:
42 % Preallocation, the Vandermonde-Matrix has the dimensions n x (d+1)
43 V = ones(length(x), order+1);
44 % Set the d-th column equal to x (the (d+1)-th column is already ...
    set equal
45 % to 1 in the previous step)
46 V(:,order) = x;
47
48 % Set the remaining columns of V, beginning at the (d-1)-th ...
    column and
49 % ending at the 1-st column
50 for k=(order-1):-1:1
51 V(:,k) = x.* V(:,k+1);
52 end
53
54 % Perform the QR-decomposition
55 %[Q,R] = qr(V,0);
56 %Rinv = pinv(V);
57 Vinv = pinv(V);
58 %Initialize the coefficient vector a:
59 %a = Rinv * Q' * y;
60 a = Vinv *y;
61 % Perform an initial estimation of the baseline
62 yModel = V*a;
63
64 % Compute the terms, that do not change during the iterative ...
    process before
65 % the for-loop, in order to increase the efficiency of the function
66 % Set the value of alpha (it is convenient to set it close to ...
    alphaMax, in
67 % order to reach the convergence quicker)
68 alpha = 0.99*alphaMax;
69 yModelprev = zeros(length(y),1);
70
71 % Perform the iteration. End it if:
72 % -- the maximum number of iterations is reached OR
73 % -- the termination-criterion is fulfilled
74 for i= 1:maxNumberIter
75 % Define the termination-criterion (if it is reached or
76 % i=maxNumberIter, the iteration is stopped)
77 if (sum((yModel-yModelprev).^2) < 1e-9)
78 break;
79 end
80 % Compute 'epsilon', which is the difference between the observation

```



```

81 % and the model
82 yModelprev = yModel;
83 epsil = y-yModel;
84
85
86 switch costfct
87 % to avoid another for-loop here, create a logic array, that
88 % consists of zeros and ones, depending on the fulfilled
89 % condition
90 case 'SymmTruncQuadr'
91 % Condition 1: phi'(x) = 2x (if |x| < s)
92 cond1 = (abs(epsil)<s);
93 % Condition 2: phi'(x) = 0 (otherwise)
94 cond2 = (abs(epsil)≥s);
95 % compute d (d=-epsilon+alpha*phi'(epsilon)):
96 d = (-epsil+alpha*2*epsil) .* cond1 + (-epsil) .*cond2;
97 case 'ASymmTruncQuadr'
98 % Condition 1: phi'(x) = x^2 (if x < s)
99 cond1 = (epsil <s);
100 % Condition 2: phi'(x) = s^2 (otherwise)
101 cond2 = (epsil ≥s);
102 % compute d (d=-epsilon+alpha*phi'(epsilon)):
103 d = (-epsil+alpha*2*epsil) .* cond1 + (-epsil).*cond2;
104 case 'SymmHuber'
105 % Condition 1: phi'(x) = -2s (if x < -s)
106 cond1 = (epsil ≤ -s);
107 % Condition 2: phi'(x) = 2x (if |x| < s)
108 cond2 = (abs(epsil) < s);
109 % Condition 3: phi'(x) = 2s (if x ≥ s)
110 cond3 = (epsil≥s);
111 % compute d (d=-epsilon+alpha*phi'(epsilon)):
112 d = (-epsil+alpha*(-2*s)).*cond1 + (-epsil+alpha*2*epsil).*cond2 ...
      + (-epsil+alpha*2*s).*cond3;
113 case 'ASymmHuber'
114 % Condition 1: phi'(x) = 2x (if x < s)
115 cond1 = (epsil<s);
116 % Condition 2: phi'(x) = 2s (otherwise)
117 cond2 = (epsil ≥s);
118 % compute d (d=-epsilon+alpha*phi'(epsilon))
119 d = (-epsil+alpha*2*epsil) .*cond1 +((-epsil+alpha*2*s) .* cond2);
120
121 end
122 % Calculate the coefficientvector
123 %a = Rinv*Q'*(y+d);
124 a = Vinv*(y+d);
125 % Get the baseline
126 yModel = V*a;

```

```
127
128 end
129
130 yBL = yModel;
131
132 end
```

### A.3 Adaptive Iteratively Reweighted Penalized Least-Squares Background Correction

```
1 function yBaseline = ...
    adapIterReWeightPenLeastSq(y,m,maxNumberIter,lambda)
2 % Description: The aim of this function is to provide an ...
    algorithm, that
3 % models the baseline of the input signal, which can later be ...
    subtracted in
4 % the corresponding script file
5
6 % Inputs: y... a column vector, containing the observations
7 %         m...used for the m-th difference-matrix Dm
8 %         maxNumberIter...maximum number of iterations
9 %         lambda...smoothing parameter
10
11 % Output: yBL...a column vector, that contains the values of the ...
    modelled
12 %         baseline
13
14
15 % Author: Florian Floh
16 % (c) 2019, Florian Floh
17 % email: florian.floh@stud.unileoben.ac.at
18
19
20 % Check if y is a column vector (and if not, make it a column ...
    vector)
21 if (iscolumn(y) ≠ 1)
22 y = y';
23 end
24
25 % Deal with NaNs (remove all NaN-entries from the vector y)
26 y = y(~isnan(y));
27 % Compute the number of rows in y
28 n = length(y);
```

```

29
30 % Check how many input arguments have been assigned to the ...
    function, and
31 % give them a predefined value if required
32 if nargin < 4, lambda = 10e10;end;
33 if nargin < 3, maxNumberIter = 20;end;
34 if nargin < 2, m = 3; end;
35
36 % Compute the terms, that do not change during the iterative ...
    process before
37 % the for-loop, in order to increase the efficiency of the function
38
39 % the m-th difference matrix:
40 Dm = diff(speye(n), m);
41
42 % lambda*Dm'*Dm:
43 lamDmTDm = lambda * Dm' * Dm;
44
45 % the column vector containing the weighting values wi (which ...
    will be set to 1 in
46 % the next step)
47 w = ones(n,1);
48
49 % Perform the iteration, until the termination criterion is ...
    reached (or the
50 % maximum number of iteration is reached)
51 for t = 1:maxNumberIter
52 % Use the vector w to build up the diagonal matrix W
53 W = spdiags(w,0,n,n);
54
55 % Given a symmetric positive semi definite matrix A, factorize ...
    it into
56 % an upper triangular matrix R, so that A = R'R. Use the Matlab ...
    function
57 % 'chol', that performs a Cholesky-Factorization. See
58 % Matlab-Documentation
59 R =sparse(chol(W + lamDmTDm));
60
61 % Given a linear equation (R'Rx = b), x is obtained in the following
62 % manner: x = R\'(R'\b)
63 % However, here the function 'mldivide' is used, which is ...
    equivalent to
64 % the backslash
65 yBL = mldivide(R,mldivide(R',W*y));
66
67 % Compute the vector d (difference between the elements in the
68 % observation vector and the modelled baseline vector)

```

```

69 d = y -yBL;
70
71 % get the negative entries of d:
72 dneg = d(d<0);
73 % compute the sum of all entries in dneg
74 sumdneg = sum(dneg);
75 % compute the absolute value of the sum in dneg. this will be needed
76 % for the termination criterion: abs(d) < 0.01*abs(y)
77 absSumdneg = abs(sumdneg);
78 % get the absolute values of the entries in y
79 yabs = abs(y);
80 % get the sum of the absolute values in yabs
81 yabsSum = sum(yabs);
82
83 % the termination criterion (the function is terminated, if this
84 % criterion is reached)
85 if absSumdneg < 0.001 * yabsSum
86 break;
87 end
88
89 % set the values of the weighting vector w (this is done via ...
      indexing,
90 % instead of using a for-loop, since it is much faster)
91 % every entry wi of w is calculated in the following manner
92 % if (y(i,1) < yBL(i,1))
93 w(d<0,1) = exp((t*(abs(dneg)))/absSumdneg);
94
95 % if (y(i,1) ≥ yBL(i,1))
96 w(d≥0,1) = 0;
97
98 end
99
100 yBaseline = yBL;

```

## A.4 Synthetic Spectrometer Data

```

1 %% Generate Synthetic Spectrometer Data
2 % Description: The aim of this script is to generate synthetic ...
      spectrometer
3 % data that permits to evaluate the methods (peak detection, noise
4 % reduction and fitting a baseline) described in this thesis
5
6 % As stated in the chapter "Generating Synthetic Spectrometer ...
      Data", data

```

```
7 % from a spectrometer data can be represented in the following way:
8 %  $ys = b + p + n$ 
9 %
10 % b...vector, whose entries describe the baseline
11 % p...vector, whose entries describe the analytical signal
12 % n...vector containing noise
13
14 % Author: Florian Floh
15 % (c) 2019, Florian Floh
16 % email: florian.floh@stud.unileoben.ac.at
17
18 %% Prepare the Workspace
19
20 clc;
21 clear;
22
23 %% Set up the x-Vector
24
25 % Define the range of the x-vector
26 xMin = 500;
27 xMax = 1000;
28 nrPts = 10000;
29 % Generate a column-vector, whose entries are equally spaced
30 x = linspace(xMin, xMax, nrPts)';
31
32 %% Generate the Baseline
33
34 % Define the minimum and maximum value of the baseline
35 yBLMin = 0;
36 yBLMax = 200000;
37 % Specify the order of the baseline
38 order = 3;
39 yBaseLine = (yBLMax-yBLMin).*rand(nrPts,1) + yBLMin;
40
41 % Fit a polynomial to the data-points, in order to obtain the ...
    model of the
42 % baseline
43 [aBaseLineModel, S, mu] = polyfit(x,yBaseLine,order);
44 yBaseLineModel = polyval(aBaseLineModel,x,S,mu);
45
46 %% Add Noise
47
48 % Generate the noise, that is later added to the baseline
49 gain = 300;
50 noise = gain * randn(size(yBaseLineModel));
51
52 %% Create Peaks
```

```

53
54 % Specify the width of the peaks, the standard deviation and the ...
    mean
55 peakWidth = 10;
56 standdev = 0.5;
57 meanv = 0;
58
59 % Create a local x-vector solely for the peaks
60 xG = linspace(-peakWidth,peakWidth,51)';
61 g = (1/(standdev*sqrt(2*pi)))*exp(-((1/2)*(xG-meanv)/standdev).^2);
62 % Normalize the values of the peaks, so that their maximum ...
    height is equal
63 % to 1, so that their height can later be adjusted by ...
    multiplying them with
64 % a desired height
65 g = g'/max(g);
66
67 %% Add the peaks
68
69 % Specify the number of desired peaks
70 numberOfPeaks = 100;
71 % Set the maximum and minimum height of the peaks
72 maxPeakHeight = 60000;
73 minPeakHeight = 100;
74
75 % Create random locations, where the peaks should be added
76 a = length(x)-(length(xG)+1)/2;
77 b = (length(xG)+1)/2;
78 xm = randi([b,a],numberOfPeaks,1);
79
80 % Set up a vector containing the height for each corresponding peak
81 peakHeights = (maxPeakHeight - ...
    minPeakHeight).*rand(numberOfPeaks,1)+...
82 minPeakHeight;
83
84 % Add the peaks to the baseline
85 % Here, special care is needed, since the peaks shall not be ...
    added at the
86 % very beginning or ending of the baseline, otherwise they might get
87 % truncated
88 % Therefore, their width has to be taken into account, to add ...
    them at
89 % proper locations
90 for i=1:numberOfPeaks
91 yBaseLineModel(xm(i)-(length(xG)-1)/2:xm(i)+...
92 (length(xG)-1)/2,1) = yBaseLineModel(xm(i)-...
93 (length(xG)-1)/2:xm(i)+(length(xG)-1)/2,1)+peakHeights(i)*g';

```

```
94 end
95
96 % Add the noise to the baseline
97 y = yBaseLineModel+noise;
98
99 %% Plot the result
100 plot(x,y);
101 title('\textbf{Synthetic Spectrometer Data}', 'interpreter', ...
102 'latex', 'FontSize', 25);
103 xlabel('\boldmath$Wavelength[nm]$', 'interpreter', 'latex', ...
104         'FontSize', 20);
104 ylabel('\boldmath$Counts[-]$', 'interpreter', 'latex', ...
105         'FontSize', 20);
105 grid on;
106 grid minor;
107 set(gca, 'FontSize', 18);
```

## A.5 Peak Detection

```
1 function [xPeak, yPeak]=detectPeak(x,y, windowSize, threshold)
2 % Description: The purpose of this function is to detect the ...
3 % peaks (i.e.
4 % local maxima in a signal and give back their locations and values
5 %Input: y...vector containing the observations
6 %       x...location of the corresponding y-vector
7 %       windowSize...specifies the windowSize, in which the peak ...
8 %       shall
9 %       be detected
10 %       threshold...gives a minimum value, where all peak values ...
11 %       that
12 %       are smaller than the predefined 'threshold' value shall be
13 %       ignored
14 %
15 %Output: xPeak...x-values of the local maxima
16 %        yPeak...the peak values
17 %
18 % Author: Florian Floh
19 % (c) 2019, Florian Floh
20 % email: florian.floh@stud.unileoben.ac.at
21
22 % If there is no input for the threshold-value, set it do 0 by ...
23 % default
```

```
22 if nargin ==3
23 threshold =0;
24 end
25
26 % Check if y is a column vector (and if not, make it a column ...
    vector)
27 if (iscolumn(y) ≠ 1)
28 y = y';
29 end
30
31 % Deal with NaNs (remove all NaN-entries from the vector y)
32 y = y(~isnan(y));
33
34 % Since a peak is characterized through a higher value than its
35 % neighbouring values, the differences between the adjacent ...
    values in
36 % the y-vector are computed. This is done via the MATLAB-function
37 % "diff", that does it in the following way:
38 % Given a vector y=[y(1), y(2), ....., y(m)] with the length m
39 % diff(y) gives: y=[y(2)-y(1), y(3)-y(2), ....., y(m)-y(m-1)] with the
40 % length (m-1)
41 ydiff = diff(y);
42
43 % Extract the sign of the values in the ydiff-vector. This can ...
    be done
44 % with the "sign" function, that returns:
45 %         | 1 if x > 0
46 %sign(x) = | 0 if x = 0
47 %         |-1 if x < 0
48
49 ydiffSign = sign(ydiff);
50
51 % The ydiffSign-vector contains -1,0 and 1. A peak is now ...
    characterized,
52 % if the pattern [1,-1]' appears. This can be found for ...
    instance, via
53 % convolution. If the pattern matches, the output will be equal ...
    to 2.
54 ypeaks = conv(ydiffSign, [-1,1]);
55
56 xPeak = [];
57 yPeak = [];
58 % Check the vector ypeaks, in order to find the maximum in each ...
    window
59 for i=1:length(ypeaks) - windowsize +1
60 % Create a temporary array, that has the size of each window
61 temparray = ypeaks(i:i+windowsize-1);
```



```
62
63 % Detect all possible maximas within the window
64 possmax = find(temparray ==2);
65
66 defmax = 0;
67 indmax = 0;
68
69 % check for the absolute maximum among all possible maximas in the
70 % window
71 for j=1:length(possmax)
72 if(y(possmax(j)+i-1) > defmax && y(possmax(j)+i-1) > threshold)
73 % get the y-value of the maximum
74 defmax = y(possmax(j)+i-1);
75 % get the indices of the maximum
76 indmax = possmax(j)+i-1;
77 end
78 end
79
80 xPeak = [xPeak indmax];
81 end
82
83 xPeak = unique(xPeak);
84 xPeak = xPeak(xPeak≠0);
85
86 yPeak = y(xPeak);
87 xPeak = x(xPeak);
88 end
```

# Bibliography

- [1] Yuri N. Toulouevski and Ilyaz Y. Zinurov. *Innovation in Electric Arc Furnaces-Scientific Basis for Selection*. Springer, Canada and Russia, 2010. ISBN:978-3-642-03800-6.
- [2] Herbert Pfeifer Marcus Kirschen, Victor Risonarta. *Energy efficiency and the influence of gas burners to the energy related carbon dioxide emissions of electric arc furnaces in steel industry*. Energy 34, 2009. DOI: 10.1016/j.energy.2009.04.015.
- [3] Harrer O. *Maschinen und Anlagen der Metallurgie*. Lecture Script, Montanuniversität Leoben, 2012.
- [4] Hendrik Schnack. *Schnelle Stromregelung von Drehstrom-Lichtbogenöfen mit Halbleiter-Stufenschaltern*. PhD thesis, Helmut-Schmidt-Universität, 2016.
- [5] Klaus Krüger and Ben Bowman. *Arc Furnace Physics*. Stahleisen, Germany, 2009. ISBN:978-3514007680.
- [6] Richard J. Fruehan et al. *The Making, Shaping and Treating of Steel: 11th Edition-Steelmaking and Refining Volume*. The AISE Steel Foundation, USA, 1998. ISBN:0-930767-02-0.
- [7] Klaus Krueger and Markus Abel. *Design of the High-Current System for AC-Furnaces*. Seminar, Electrical Engineering of Arc Furnaces, 2017.
- [8] Jan F. Plaul. *Schmelzreduktion von hämatitischen Feinerzen im Wasserstoff-Argon-Plasma*. PhD thesis, Montanuniversität, 2005.
- [9] J. Michael Hollas. *Basic Atomic and Molecular Spectroscopy*. The Royal Society of Chemistry, Reading, 2002. ISBN:978-0-85404-667-6.
- [10] Daniel C. Harris and Charles A. Lucy. *Quantitative Chemical Analysis*. W. H. Freeman and Company, USA, 2016. ISBN:978-1-4641-3538-5.
- [11] Sophocles J. Orfanidis. *Introduction to Signal Processing*. Prentice Hall International, Englewood Cliffs, 1996. ISBN:0-13-240334-X.

- [12] Understanding boxplots. <https://towardsdatascience.com/understanding-boxplots-5e2df7bcbd51>. Accessed: 28-09-2019.
- [13] Karim Badr. *Smelting of Iron Oxides Using Hydrogen Based Plasmas*. PhD thesis, Montanuniversität, 2007.
- [14] AvaSpec-ULS3648 StarLine High-resolution Fiber-optic Spectrometer. [https://www.avantes.com/images/stories/brochurescat2012/33-35\\_-\\_avaspec-uls3648.pdf](https://www.avantes.com/images/stories/brochurescat2012/33-35_-_avaspec-uls3648.pdf). Accessed: 28-09-2019.
- [15] World Steel Association. Steel Statistical Yearbook 2017. <https://www.worldsteel.org/steel-by-topic/statistics/steel-statistical-yearbook.html>. Accessed: 25.06.2019.
- [16] Yuri N. Toulouevski and Ilyaz Y. Zinurov. *Fuel Arc Furnace (FAF) for Effective Scrap Melting- From EAF to FAF*. Springer, Canada and Russia, 2017. ISBN: 978-981-10-5884-4.
- [17] Klaus Krüger and Andrey Galochkin. *Verfahren zur Ermittlung eines Betriebs- und/oder Werkstoffparameters in einem Elektrolichtbogenofen und Elektrolichtbogenofen*. 13.05.2015. EP 2 686 665 B1.
- [18] Wolfgang Suttrop. *Technische Plasmen*. Lecture Script, Universität Bayreuth, 2003.
- [19] Paul A. Tipler and Gene Mosca. *Physik fuer Wissenschaftler und Ingenieure*. Springer Spektrum, Germany, 2012. ISBN: 978-3-8274-1945-3.
- [20] E. Bäck. *Schmelzreduktion von Eisenoxiden mit Argon-Wasserstoff-Plasma*. PhD thesis, Montanuniversität, 1998.
- [21] Fibers and Probes. [https://oceanoptics.com/wp-content/uploads/Ocean\\_Optics\\_Fibers\\_Probes.pdf](https://oceanoptics.com/wp-content/uploads/Ocean_Optics_Fibers_Probes.pdf). Accessed: 28-09-2019.
- [22] Marcel J. E. Golay Abraham Savitzky. *Smoothing and Differentiation of Data by Simplified Least Squares Procedures*. Anal. Chem., vol. 36, 1964. DOI:10.1021/ac60214a047.
- [23] Ronald W. Schafer. *What Is a Savitzky-Golay Filter?* IEEE Signal Processing Magazine, pages 111-117, 2011. DOI: 10.1109/MSP.2011.941097.
- [24] Matthew Harker Paul O'Leary. *Discrete Polynomial Moments and Savitzky-Golay Smoothing*. World Academy of Science, Engineering and Technology 48, 2010. DOI:10.5281/zenodo.1078873.

- [25] Paul O’Leary. *Data Science for Engineers II*. Lecture Script, Montanuniversität Leoben, 2018.
- [26] Jing Bai Jianwen Luo, Kui Ying. *Savitzky-Golay smoothing and differentiation filter for even number data*. *Signal Processing* 85, 2005. DOI:10.1016/j.sigpro.2005.02.002.
- [27] L.H.J. Lajunen and P. Peramaki. *Spectrochemical Analysis by Atomic Absorption and Emission*. The Royal Society of Chemistry, Finland, 2004. ISBN: 0-85 404-624-0.
- [28] et al. Vincent Mazet. *Background removal from spectra by designing and minimizing a non-quadratic cost function*. *Chemometrics and Intelligent Laboratory Systems* 76, 2004. DOI:10.1016/j.chemolab.2004.10.003.
- [29] Jerome Idier. *Convex Half-Quadratic Criteria and Interacting Auxiliary Variables for Image Restoration*. *IEEE Transactions on Image Processing*, Vol. 10, No. 7, 2001. DOI:10.1109/83.931094.
- [30] Donald Geman and Chengda Yang. *Nonlinear Image Recovery with Half-Quadratic Regularization*. *IEEE Transactions on Image Processing*, Vol. 14, No. 7, 1995. DOI:10.1109/83.392335.
- [31] Raphael Moulart and Rene Rotinat. *On the Use of a Penalized Least Squares Method to Process Kinematic Full-Field Measurements*. *Measurement Science and Technology*, Vol. 25, No. 7, 2014. DOI:10.1088/0957-0233/25/7/075001.
- [32] G. Bohlmann. *Ein Ausgleichungsproblem*. Nachrichten von der Gesellschaft der Wissenschaften zu Göttingen, Mathematisch-Physikalische Klasse, 1899.
- [33] D. Garcia. *Robust Smoothing of Gridded Data in One and Higher Dimensions with Missing Values*. *Computational Statistics and Data Analysis*, Vol. 56, No. 6, 2010.
- [34] Yi-Zeng Liang Zhi-Min Zhang, Shan Chen. *Baseline correction using adaptive iteratively reweighted penalized least squares*. *The Analyst* 135(5), 2010. DOI:10.1039/b922045c.
- [35] Roger Schneider. *Survey of Peaks/Valley identification in Time Series*. 2011.
- [36] Kurt Meyberg and Peter Vachenauer. *Hoehere Mathematik I*. Springer, Germany, 2003. ISBN: 3-540-41850-4.
- [37] Find local maxima by convolution. <http://matlabtricks.com/post-47/find-local-maximas-of-an-1d-signal-by-convolution>. Accessed: 22-09-2019.

- [38] Differences and approximate derivatives. <https://de.mathworks.com/help/matlab/ref/diff.html>. Accessed: 22-09-2019.
- [39] Christian Blatter. *Ingenieur Analysis 1*. Springer, Swiss, 1996. ISBN: 3-540-60438-3.
- [40] Find indices and values of nonzero elements. [https://de.mathworks.com/help/matlab/ref/find.html?s\\_tid=srchtitle](https://de.mathworks.com/help/matlab/ref/find.html?s_tid=srchtitle). Accessed: 23-09-2019.
- [41] NIST Atomic Spectra Database Lines Form. [https://physics.nist.gov/PhysRefData/ASD/lines\\_form.html](https://physics.nist.gov/PhysRefData/ASD/lines_form.html). Accessed: 17-09-2019.
- [42] Correlation coefficients. <https://de.mathworks.com/help/matlab/ref/corrcoef.html>. Accessed: 28-09-2019.
- [43] Simple linear regression. [https://de.mathworks.com/help/matlab/data\\_analysis/linear-regression.html](https://de.mathworks.com/help/matlab/data_analysis/linear-regression.html). Accessed: 28-09-2019.
- [44] Graham Upton and Ian Cook. *Understanding Statistics*. Oxford University Press, UK, 1996. ISBN: 0-19-914391-9.
- [45] Interquartile range. [https://de.mathworks.com/help/stats/prob.normaldistribution.iqr.html?searchHighlight=interquartile%20range&s\\_tid=doc\\_srchttitle](https://de.mathworks.com/help/stats/prob.normaldistribution.iqr.html?searchHighlight=interquartile%20range&s_tid=doc_srchttitle). Accessed: 28-09-2019.
- [46] et al. J. Gruber. *In Situ Analysis of Metal Melts in Metallurgic Vacuum Devices by Laser-Induced Breakdown Spectroscopy*. Applied Spectroscopy, Volume 58, Number 4, 2004. DOI:10.1366/000370204773580310.